UNIVERSITY OF CALIFORNIA
RIVERSIDE

Rationally Designed Scaffold Increase Enzyme and Cascade Kinetics via Local Environmental

A Dissertation submitted in partial satisfaction
of the requirements for the degree of

Doctor of Philosophy

in

Biochemistry and Molecular Biology

by

Xiao Hong

December 2021

Dissertation Committee:
Dr. Ian Wheeldon, Chairperson
Dr. Russ Hille
Dr. Chia-en Chang

The Dissertation of Xiao Hong is approved:

_____

_____

_____

Committee Chairperson

University of California, Riverside

ACKNOWLEDGEMENTS

No matter what industry lore or movie fiction says, no one can walk the path of research completely alone. Along the way, there is always a need for guidance, assistance, and even silent companionship.

Therefore, I would like to express my highest appreciation to my mentor, Dr. Ian Wheeldon. I would like to thank him for his continuous support, encouraging discussions and his confidence in me. Postdocs Xuye Lang was my inspiration for my PhD career, especially in helping me through the most dismal "unproductive" period. Mengwan Li and Shuang Wei, in our group, as important members of the recreational team, have helped me to enrich my spare time and to find a balance between research and life. Of course, I also appreciate their passion for research and their amazing abilities.

I would also like to thank Dr. Russ Hille and Dr. Chian-en Chang for their continued support, research advice, and friendship, and Dr. Chian-en Chang and her graduate student, Tim Cholko, for their tremendous help with my publication. I hope the article will be published soon. Other members I have had the pleasure of working with include Dr. Tamara C. Otto and her graduate student Cetara A. Baker, Dr. Scott Banta and his graduate student Walaa Abdallah. I would like to express my sincere gratitude.

I would also like to thank the publishers of Biotechnology and Bioengineering for allowing me to reprint Chapter 2. The content of Chapters 3 and 4 is derived in part from material in Current Opinion in Biotechnology (2021) and ACS catalysis (2022 under review).

Finally, I would like to thank my parents and Shan for their love, dedication and support during these five years away from them. I miss them very much.

My motivation for embarking on this adventure is simple: to pursue my studies and live a life free of vanity. The world is unpredictable, and I'm sure I'll have to deal with more difficult situations in the future. However, I already own the strength and patience to confront any difficulties or challenges that may arise. What I only hope is that years may wrinkle my skin, but will never wrinkle my soul. Finally, if I can contribute to making other people's lives better, my life will have been worthwhile.

ABSTRACT OF THE DISSERTATION

Rationally Designed Scaffold Increase Enzyme and Cascade Kinetics via Local Environmental

by

Xiao Hong

Doctor of Philosophy, Graduate Program in Biochemistry and Molecular Biology
University of California, Riverside, December 2021
Dr. Ian Wheeldon, Chairperson

Enzymes are highly effective catalysts that enable biological reactions and control complex metabolic and cell processes. Over the past few decades, active site engineering has dramatically improved enzyme kinetics; however, in many cases catalytic efficiency (k_{cat}/K_M) can be limiting to the desired application. There have also been considerable efforts put towards increasing enzyme stability through immobilization on solid supports. Recently, nanoscale molecular engineering tools have opened the possibility of replicating the enhancement of immobilization while also controlling an enzyme's local chemical and physical microenvironment. These new molecular tools have opened a new approach to enzyme engineering that has the potential to both control enzyme kinetics as well as provide the benefits of increased stability often observed with immobilization. Here, we propose the design and application of rationally designed biomolecular scaffolds to control

an enzyme's microenvironment and consequently enhance reaction kinetics. The first example of this approach is the engineering of phosphotriesterase (PTE), a potential therapeutic countermeasure for organophosphate toxicity, with DNA scaffolds. The challenge is that highly toxic nerve agents, such as VX or Sarin, are potentially deadly at very low concentration, thus requiring a biocatalytic scavenger with high catalytic rates at low concentrations. We show that small DNA scaffolds designed to bind organophosphates in a sequence-dependent manner can decrease the Michaels parameter (K_M) and increase the second order rate constant of PTE by nearly 11-fold, thus providing high catalytic rates at low organophosphate concentrations. We also show that the position of the scaffold is critical to the enhancement; conjugation of the scaffold close to the active site provides the largest enhancement provided that the active site is not blocked by the appended scaffold. The second example of our approach is to control a microenvironment of a two-step enzyme cascade. We modeled the cascade reaction between hexokinase-2 (HK2) and glucose-6-phosphate dehydrogenase (G6PD) and linked them by superfold green fluorescent protein (sfGFP) with different charges (+36, 0, -30). We observed that (+36)sfGFP enhanced cascade kinetics, (-30)sfGFP did the opposite, and (0)sfGFP had no effect on the cascade. We also showed that the modification of sfGFP significantly altered the kinetics of the assembled enzymes, including k_{cat}, K_M, and K_i. We simulated and fitted the experiments with the model, and the results showed that the enhanced kinetics of this cascade was due to change in the kinetics of the assembled enzymes, influenced by the microenvironment change of the scaffold.

TABLET OF CONTENTS

LIST OF FIGURES

LIST OF SUPPORTING FIGURES

LIST OF TABLES

LIST OF SUPPORTING TABLES

LIST OF SUPPORTING LISTS

Chapter 1. Introduction

1.1 Background

Enzymes are highly efficient biocatalysts that determine the rate of biological reactions and control complex metabolic pathways and other cellular processes [1]. Due to their incredible catalytic efficiency, enzymes are now an important industrial tool for targeted chemical transformations [2]. Modern enzymology, in particular, is at the core of food and beverage processing operations, with applications in animal feed manufacture, processing, quality improvement, detergents, medicines, and textiles [3]. However, natural enzymes often have low catalytic efficiency under the conditions of a desired application and can be prone to denaturation [4]. The disadvantages of natural enzymes are becoming glaringly evident, mainly as industrial demand grows. Researchers have modified and implemented enzyme engineering of small and big molecules to overcome the constraints of thermal instability in enzymes through continuous innovation in protein products. Enzyme engineering strategies typically include directed evolution, directed mutagenesis, truncation, end-binding, and directed modification [5]. To a considerable extent, a proper implementation resolves the thermal instability of enzymes. For example, a sturdy PEG [6] or a DNA scaffold can be wrapped around a target enzyme to generate an enzyme-engineered complex. Enzymes modified in this way have shown a 4-fold increase in residual activity after 48 h incubation at 37 ℃ in plasma compared to the unmodified natural enzyme [7].

The catalytic activity of natural enzymes has also garnered more study in recent years. Subsequently, active site engineering, which includes rational design, guided evolution, and computer-aided design, has substantially enhanced natural enzyme catalytic efficiency. However, in many cases, the enzyme's catalytic efficiency (k_{cat}/K_M) is limited and cannot reach the current industrial demand [8,9] . Based on this, the challenge regarding enzymes has shifted to improve the catalytic efficiency of enzymes. As a result, a novel method is required to break through this barrier and develop enzymes with high activity under the desired conditions. Chapter 2 describes a novel approach enzyme engineering founded on the notion that changing the microenvironment around an enzyme might boost its catalytic activity in its current context. This enzyme engineering strategy has the potential to further increase enzyme kinetics once the limitations of enzyme active site engineering are reached. The studies presented here used the breakdown of organophosphates by phosphotriesterase (PTE) as a test case for the approach. We achieved increases in the effective concentration of organophosphates in the vicinity of PTE via rationally designed DNA scaffolds cross-linking to PTE. We demonstrated that DNA conjugation did not change PTE's turnover rate (k_{cat}) but effectively enhanced the Michaels constant (K_M) and the second order rate constant (k_{cat}/K_M). As a result, PTE's degradation rate to the target organophosphate was ultimately enhanced.

We used the same DNA scaffold and crosslinker to modify various PTE mutants. The results revealed a high degree of variability in the K_M of PTE mutants changed following modification. A similar thing happened in our previous investigation [10]; only the proximate sites to the active site affected the protein's kinetics after DNA conjugation.

Based on this observation, we hypothesized in Chapter 3 that the modification location significantly influenced protein dynamics. To better understand the system, we simulated the substrate concentration surrounding DNA and controlled the DNA position with noncanonical amino acid technology. We ultimately built a model to characterize the connection between simulation and experiment. The findings suggest that our model can accurately describe the influence of DNA alteration on PTE kinetics at various places. Meanwhile, when DNA does not obstruct the PTE active site, the closer the DNA is to the PTE active site, the more prominent the K_M change is.

In Chapter 4, we broaden our research model from single enzyme to multi-enzyme cascades because complex living activities in organisms are frequently accomplished through the collaboration of numerous enzymes. The substrate channel effect is one method for enhancing cascade. This effect has been observed in nature, increasing the apparent k_{cat} of the cascade; however, the mechanism behind this increase is not completely understood (or more specifically, the contributions of channeling to increased reaction rate are difficult to delineate from other effects). Both natural and engineered scaffolds can produce substrate channels, which improve intermediate transport; however, these scaffolds can also change the microenvironment to which the assembled enzyme is exposed. The microenvironment influences assembled enzyme activity, complicating kinetic studies [11]. Chapter 4 utilized Hexokinase II (HK2) and glucose-6-phosphate dehydrogenase (G6PD) as a model. A series of differently charged sfGFPs were included to form substrate channels by electrostatic guidance. The results indicated that the charged sfGFP increased the cascade's k_{cat}, the essential factor in the substrate channel development. This improvement,

however, was not primarily owing to an increase in intermediate diffusion. The sfGFP alteration also significantly affected the kinetics of the constructed enzyme. Moreover, the assembled enzyme kinetics change is adequate to model and describe cascade enhancement.

1.1.1 Organophosphate degradation by phosphotriesterase

Organophosphates are a group of C-P-linked organic compounds containing phosphate groups [12]. The mechanism of organophosphates is the inhibition of acetylcholinesterase (AChE). The process is shown in Figure 1.1. The inhibition occurs on the activated serine of the AChE active site, which is nucleophilically attacked by the electrophilic phosphorus atom. In cholinesterase, there are several groups of serine and threonine residues that contain alcohol groups. In combination with the adjacent carboxyl groups of histidine and glutamate or aspartate, these residues respond to the hydrolysis of the neurotransmitter acetylcholine. The adequacy of this alcohol activation process allows for an extremely high turnover rate. However, serine residues are particularly susceptible to inactivation by phosphorylation of organophosphates. Meanwhile, phosphate-serine bonds are highly stable, so the whole phosphorylation process can be considered irreversible [12,13]. Because of their ability to effectively inhibit the normal function of the nervous system, OP compounds have been widely used as pesticides in agriculture and as weapons of mass destruction in warfare [14]. Despite their toxicity and severe environmental pollution, OP compounds still play an essential role in daily life and cannot be replaced soon [15].

So far, a new approach has been developed. It aims at the selective degradation of organophosphates by designing PTE, which are metal-dependent hydrolases. The hydrophobic active site has three discontinuous binding pockets to accommodate the ester groups of the organophosphate [16]. Although PTE is still not commercially available, which means it needs to be expressed and purified, its protein sequence, three-dimensional structure, and catalytic mechanism are well understood [17,18]. The purpose of PTE is to hydrolyze organophosphates before they are inhibited, as shown in Figure 1.1. Recent enzyme engineering studies have provided great efforts to reach efficiencies of about 2×10^6 $M^{-1}s^{-1}$, which is the minimum requirement for enzymatic treatment of organophosphate poisoning [19]. Enzymatic treatment shows strong potential compared to conventional drug strategies with toxicity, but its activity is insufficient to replace existing therapeutic approaches.

Additional strategies, such as protein modifications, can be used independently or in combination. Specifically, target organophosphates (VX agents and paraoxon, but not interacting with DDVP) can be attracted to rationally designed DNA fragments and DNA scaffolds. This attraction increases the concentration of local reactants. In addition, one manifestation is a faster movement of the target substrate to the active site (increased conductivity constant). Specifically, with this rationally designed form of DNA conjugation, the catalytic rate of hydrolysis of VX by PTE is increased approximately 3-fold, and that of paraoxon is increased 10-fold. In contrast, the catalytic rate of hydrolysis of DDVP did not change significantly before and after DNA conjugation.

1.1.2 Position effect of enzyme modification

Although the engineering of enzyme stability through conjugation is well understood, the design rules for conjugation strategies to improve the kinetics of enzyme reactions have yet to be clearly defined [20–23]. For instance, a protein has many structurally critical amino acids, and mutations can lead to changes in the protein structure. Our previous study [7] found that these mutants were modified by the same method and DNA scaffold but exhibited different kinetics. In another study [10], shown in figure 1.2, the model enzyme horseradish peroxidase (HRP) has only two lysine residues on its surface (near the active site (proximal) and far from the active site (distal)). The 20 bp DNA scaffold was designed to bind to the HRP substrates (tetramethylbenzidine (TMB) and 4-aminophenol (4-AP)). The increase in local substrate concentration in the HRP(DNA) nanostructure formed by this DNA scaffold conjugated with the proximal lysine phase resulted in a 2.9-fold and 2.4-fold decrease in the apparent Michaelis constants of TMB and 4-AP. In contrast, the Michaelis constants of HRP(DNA) remained almost unchanged when the DNA scaffold modified the distal lysine.

A more fundamental understanding of the relationship between conjugation chemistry, structure, and enzyme kinetics is needed to better understand the molecular mechanisms underlying these effects and advanced conjugation approaches focused on enhanced kinetics. Here, we address this lack of knowledge through a combination of computational, experimental, and modeling approaches. The results begin to develop design rules for achieving increases in effective substrate concentrations in enzyme-DNA

conjugation systems and, in doing so, relate kinetic enhancements to enzyme-DNA characteristics [7,10,24]. We take as an example the PTE-DNA conjugate system (PTE-DNA), which catalyzes the hydrolysis of organophosphates, including the chemical warfare agents VX and sarin, and the insecticide parathion, whose use is restricted in the United States and other countries.

Experimental techniques alone often lack the resolution to interpret and predict the enhanced effects obtained from conjugation accurately, so we set out to combine computational modeling and simulation with studying the PTE-DNA system in more detail and quantifying impacts that are difficult to assess experimentally. Specifically, we used molecular dynamics (MD) and Brownian dynamics (BD) simulations to investigate the concentration gradient of organophosphate around the DNA scaffold used to modify the PTE in an attempt to quantify the potential increase in effective concentration from the conjugation of the substrate-binding scaffold to the enzyme of interest. We support the computational study by experimentally testing the positional effects of individual DNA scaffolds on enzyme kinetics and subsequently combining simulated and experimental data to develop mechanistic models of the impact of DNA scaffolds and conjugation location on catalysis. Our results suggest that our DNA scaffold modification of PTE reduces K_M by increasing the effective substrate concentration around the DNA and expanding the effective concentration region to include the enzyme's active site, that is by raising the substrate capture radius of the conjugated complex.

1.1.3 Enhance cascade catalysis by microenvironment effect at individual enzyme

Enzymes are often considered biological catalysts encompassing almost every life process, performing the simplest to very complex organic reactions. It starts with only a single enzyme, leading to an explosion of new possibilities for biosynthesis. Later, stepwise tandem cascade reactions performed by multiple enzymes have recently attracted attention because of their significance for novel chemical synthesis with reasonable substrate flux control and improved overall efficiency. An important key to improve the overall output of multistep reactions is to control the flux of several molecules, such as intermediates, between reaction sites [25].

So far, compartmentalization, metabolons, and scaffolds have attracted the attention of the bioengineering community to control the flux of intermediates in the cascade. In recent decades, electrostatic channels in nature have received considerable attention. One example is the bifunctional enzyme dihydrofolate reductase-synuclein synthase (DHFR-TS), in which negatively charged dihydrofolate intermediates diffuse with a positively charged structure between the two active sites [26]. Another example is in the tricarboxylic acid (TCA) cycle. The positively charged surface between malate dehydrogenase (MDH) and citrate synthase (CS) guides oxaloacetate (the negatively charged intermediate) across the active site via electrostatic interaction [27].

Although solid experimental evidence cannot be ignored to support a multi-enzyme cascade in nature, the role of the channel and its exact mechanism remain unclear and remain a persistent topic of debate [28–30]. One view is that electrostatic channels control the transport of charged intermediates between cascade sites through electrostatic action

without the need for a large environmental balance. However, Hess et al. [25] reported a simple stochastic simulation that followed the channel idea, showing that kinetic enhancement does not always occur; in particular, the channelization reaction can be even slower than the original non-channelized cascade at long (i.e., steady-state) times and high substrate concentrations. An alternative view is shown in Figure 1.3 that potentially high local metabolite concentrations are formed by electrostatic interactions and enhance the overall output of the cascade through kinetic enhancement of individual steps.

In this project, to investigate the mechanism of cascade catalysis, we synthesized an enzyme complex consisting of hexokinase II (HK2) and glucose-6-phosphate dehydrogenase (G6PD) covalently linked by sfGFP. The induced electrostatic interaction of the negatively charged intermediate glucose-6-phosphate (G6P) was controlled by three different charged sfGFP (+36, 0, -30). Cascade's turnover rate increase and decrease after sfGFP modification were well in line with the expectations of the substrate channel in a crude assessment. However, the change of the initial rate in the transition time analysis weakened the expectation of the substrate channel. Meanwhile, the kinetic constants of HK2 and G6PD before and after the modification were simulated as parameters. The simulated results were in good agreement with the experimental results of the cascade catalytic process of HK2-G6PD before and after sfGFP modification. The kinetic performance of the cascade before and after sfGFP modification is well reflected in the kinetic performance when the intermediate is produced in excess (substrate channel failure). The results are in good agreement with the idea that electrostatic interactions form the

potentially high local metabolite concentrations and that the kinetic enhancement of individual steps enhances the overall output of the cascade.

1.2 Dissertation Organization

Conventional enzyme bioconjugation is effective in improving stability; however, conjugation strategies to enhance the kinetics of enzyme reactions are still scarce, and the underlying mechanisms are worth investigating. In addition, there is no precise design specification for existing conjugation strategies, which is potentially challenged by the position effect. Therefore, the overall goal of this thesis is to further extend the conjugation strategies for enzyme reaction kinetics and clarify the relevant engineering design rules. After addressing the above issues, we hope to extend our design regulations and techniques to a broader range of cascade reactions performed by multiple enzymes.

In chapter 2, DNA fragments and scaffold sequences are rationally designed to attract the target molecules (VX agent and paraoxon but no interaction with DDVP). A schematic of this approach is shown in Figure 1.4; the attraction of substrate around the enzyme increases the local reactant concentration. As a result, PTE's VX second order hydrolysis reaction rate after this rationally designed DNA conjugation is enhanced by ~3-fold. Moreover, the paraoxon hydrolysis rate can be increased by ~10-fold after DNA conjugation. On the contrary, DDVP, which does not bind to the DNA scaffold, is not affected by the conjugation of DNA to PTE.

We answer the position effect by controlling the conjugation site in Chapter 3 and the reactant concentration around DNA was studied by MD and BD simulation. In each

simulation, the rationally designed DNA sequence maintains a similar attraction of a specific substrate flux. The different locations of DNA bring about different substrate concentration around the enzyme active site, impacting enzyme reaction kinetics. Based on the enzyme structure and the substrate concentration distribution, eight positions on PTE were modified with a DNA scaffold by the incorporation of a non-natural amino acid with a side chain that can be used for click chemistry. To describe the kinetics change, based on (1) the distance from the position to the active site of the enzyme, (2) the substrate concentration around the enzyme due to the presence of the DNA scaffold, and (3) the potential blockage of active site access by the DNA scaffold, a kinetic model was developed.

Modifying enzyme microenvironments to control enzyme catalysis is not limited to single enzyme systems but can be applied to enzyme cascades. Chapter 4 constructs an enzyme complex model by covalently connected hexokinase II (HK2) and glucose-6-phosphate dehydrogenase (G6PD) with a charged super folder GFP. Three different charged sfGFPs bring different impacts on the local electrostatic environment. For the negatively charged molecule G6P: (1) +36sfGFP attracts G6P because of the opposite charge. This attraction helps G6P no need to diffusion ultimately into the bulk environment. As a result, G6P's existence time is reduced hugely in simulation, and HK2-(+36)sfGFP-G6PD arrives at the steady-state earlier compared with no modification samples. (2) The negative electrostatic charge of -30sfGFP repels G6P towards the bulk environment, proved by the simulation estimation. As a result, HK2-(-30)sfGFP-G6PD arrives later at the steady-state time. (3) (0)sfGFP has no electrostatic charge and barely impacts G6P

diffusion and overall kinetics. The results of the simulations reveal that the cascade is altered by sfGFP not only by substrate channeling but also by the assembly enzyme kinetics.

In this thesis, we induce the transfer of target molecules and the formation of microenvironments (local concentration enhancement) through DNA and charged sfGFP, thus enhancing the kinetics of single and multiple enzyme systems. We also elucidate the positional effects that exist during the modification of enzyme kinetics. In conclusion, the above studies fully understand that the microenvironment plays a crucial role in enzyme modification. We can design controlled experiments that provide excellent opportunities for our proposed revolutionary enzyme engineering techniques when the limits of enzyme activity engineering are reached under reasonable circumstances.

1.3 Reference

1. Cooper, G. M. The Central Role of Enzymes as Biological Catalysts. in *The Cell: A Molecular Approach. 2nd edition* (Sinauer Associates, 2000).

2. Wu, S., Snajdrova, R., Moore, J. C., Baldenius, K. & Bornscheuer, U. T. Biocatalysis: Enzymatic Synthesis for Industrial Applications. *Angewandte Chemie International Edition* vol. 60 88–119 (2021).

3. Fernandes, P. Enzymes in Food Processing: A Condensed Overview on Strategies for Better Biocatalysts. *Enzyme Res.* **2010**, (2010).

4. Robinson, P. K. Enzymes: principles and biotechnological applications. *Essays Biochem.* **59**, 1–41 (2015).

5. Milczek, E. M. Commercial Applications for Enzyme-Mediated Protein Conjugation: New Developments in Enzymatic Processes to Deliver Functionalized Proteins on the Commercial Scale. *Chem. Rev.* **118**, 119–141 (2018).

6. Yang, C., Lu, D. & Liu, Z. How PEGylation enhances the stability and potency of insulin: a molecular dynamics simulation. *Biochemistry* **50**, 2585–2593 (2011).

7. Lang, X., Hong, X., Baker, C. A., Otto, T. C. & Wheeldon, I. Molecular binding scaffolds increase local substrate concentration enhancing the enzymatic hydrolysis of VX nerve agent. *Biotechnol. Bioeng.* **117**, 1970–1978 (2020).

8. Korendovych, I. V. & DeGrado, W. F. Catalytic efficiency of designed catalytic proteins. *Current Opinion in Structural Biology* vol. 27 113–121 (2014).

9. Free convective PCR: From principle study to commercial applications—A critical review. *Anal. Chim. Acta* **1108**, 177–197 (2020).

10. Gao, Y., Roberts, C. C., Toop, A., Chang, C.-E. A. & Wheeldon, I. Mechanisms of Enhanced Catalysis in Enzyme-DNA Nanostructures Revealed through Molecular Simulations and Experimental Analysis. *Chembiochem* **17**, 1430–1436 (2016).

11. Abdallah, W., Hong, X., Banta, S. & Wheeldon, I. Microenvironmental effects can masquerade as substrate channelling in cascade biocatalysis. *Curr. Opin. Biotechnol.* **73**, 233–239 (2021).

12. Organophosphorus Compounds. 714–719 (2014).

13. Neuroinflammation in organophosphate-induced neurotoxicity. in *Advances in Neurotoxicology* vol. 3 35–79 (Academic Press, 2019).

14. Thakur, M., Medintz, I. L. & Walper, S. A. Enzymatic Bioremediation of Organophosphate Compounds—Progress and Remaining Challenges. *Frontiers in Bioengineering and Biotechnology* vol. 7 (2019).

15. Hertz-Picciotto, I. *et al.* Organophosphate exposures during pregnancy and child neurodevelopment: Recommendations for essential policy reforms. *PLoS Med.* **15**, e1002671 (2018).

16. Chagas, M. A., Pereira, E. S., Godinho, M. P. B., Da Silva, J. C. S. & Rocha, W. R. Base Mechanism to the Hydrolysis of Phosphate Triester Promoted by the Cd/Cd Active site of Phosphotriesterase: A Computational Study. *Inorg. Chem.* **57**, 5888–5902 (2018).

17. Benning, M. M., Kuo, J. M., Raushel, F. M. & Holden, H. M. Three-dimensional structure of phosphotriesterase: an enzyme capable of detoxifying organophosphate nerve agents. *Biochemistry* **33**, 15001–15007 (1994).

18. Roodveldt, C. & Tawfik, D. S. Directed evolution of phosphotriesterase from Pseudomonas diminuta for heterologous expression in Escherichia coli results in stabilization of the metal-free state. *Protein Eng. Des. Sel.* **18**, 51–58 (2005).

19. Griffiths, A. D. & Tawfik, D. S. Directed evolution of an extremely fast phosphotriesterase by in vitro compartmentalization. *EMBO J.* **22**, 24–35 (2003).

20. Yan, M., Ge, J., Liu, Z. & Ouyang, P. Encapsulation of single enzyme in nanogel with enhanced biocatalytic activity and stability. *J. Am. Chem. Soc.* **128**, 11008–11009 (2006).

21. Zhang, P. *et al.* Zwitterionic gel encapsulation promotes protein stability, enhances pharmacokinetics, and reduces immunogenicity. *Proc. Natl. Acad. Sci. U. S. A.* **112**, 12046–12051 (2015).

22. Koskinen, A. & Klibanov, A. *Enzymatic Reactions in Organic Media*. (Springer Science & Business Media, 1995).

23. Chapman, R. & Stenzel, M. H. All Wrapped up: Stabilization of Enzymes within Single Enzyme Nanoparticles. *J. Am. Chem. Soc.* **141**, 2754–2769 (2019).

24. Gao, Y. *et al.* Tuning Enzyme Kinetics through Designed Intermolecular Interactions Far from the Active Site. *ACS Catalysis* vol. 5 2149–2153 (2015).

25. Zhang, Y. & Hess, H. Toward Rational Design of High-efficiency Enzyme Cascades. *ACS Catalysis* vol. 7 6018–6027 (2017).

26. Senkovich, O., Schormann, N. & Chattopadhyay, D. Structures of dihydrofolate reductase-thymidylate synthase of Trypanosoma cruzi in the folate-free state and in

complex with two antifolate drugs, trimetrexate and methotrexate. *Acta Crystallogr. D Biol. Crystallogr.* **65**, 704–716 (2009).

27. Omini, J., Wojciechowska, I., Skirycz, A., Moriyama, H. & Obata, T. Association of the malate dehydrogenase-citrate synthase metabolon is modulated by intermediates of the Krebs tricarboxylic acid cycle. doi:10.1101/2021.08.06.455447.

28. Wu, X. M., Gutfreund, H., Lakatos, S. & Chock, P. B. Substrate channeling in glycolysis: a phantom phenomenon. *Proc. Natl. Acad. Sci. U. S. A.* **88**, 497–501 (1991).

29. Zhang, Y., Tsitkov, S. & Hess, H. Proximity does not contribute to activity enhancement in the glucose oxidase–horseradish peroxidase cascade. *Nature Communications* vol. 7 (2016).

30. Poshyvailo, L., von Lieres, E. & Kondrat, S. Does metabolite channeling accelerate enzyme-catalyzed cascade reactions? *PLoS One* **12**, e0172673 (2017).

1.4 Figures and Tables

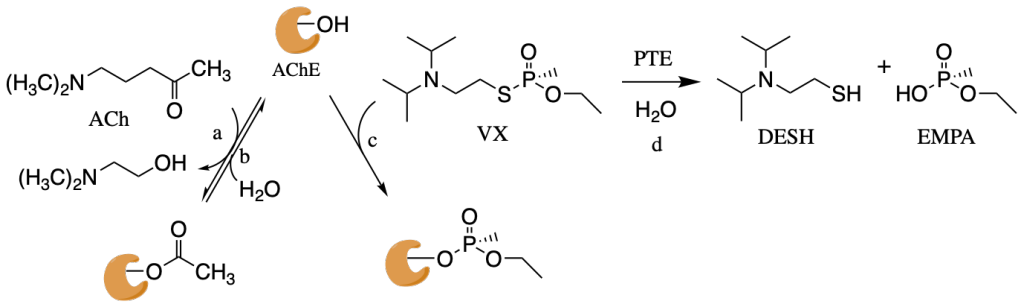

Figure 1.1 The mechanism of Organophosphate (VX) toxicity and detoxification by PTE treatment. (a) Acetylcholinesterase (AChE, the yellow structure) is an enzyme that catalyzes the breakdown of acetylcholine (ACh) which serves as neurotransmitters. (b) AChE hydrolysis recovery, the reversible process of a. (c) AChE phosphorylation and deactivation by warfare agent VX. (d) phosphotriesterase (PTE) hydrolysis VX to ethyl methylphosphonic acid (EMPA) and 2-(diisopropylamino) ethanethiol (DESH) before VX inhibits AChE.

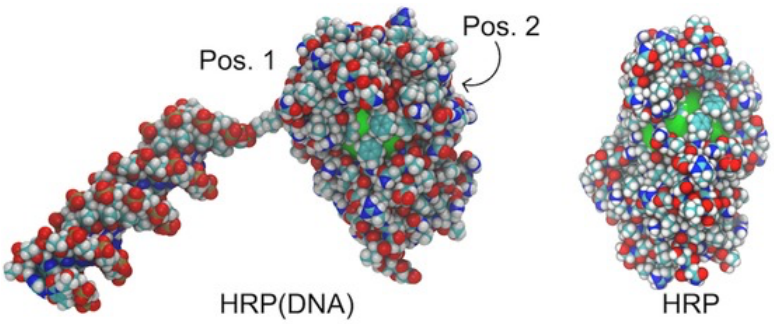

		k_1 / k_1 (HRP(DNA) / HRP)	τ_{local} / τ_{local} (HRP(DNA) / HRP)
TMB	**HRP(DNA) (Pos. 1)**	1.33±0.04	1.20
	HRP(DNA) (Pos. 2)	1.00±0.04	1.00
H_2O_2	**HRP(DNA) (Pos. 1)**	1.07±0.01	1.22
	HRP(DNA) (Pos. 2)	1.03±0.01	1.21

Figure 1.2 Molecular simulation analysis of HRP and HRP(DNA) nanostructures with TMB and H_2O_2 co-substrates. Top: Molecular models of (left) HRP with a 20 bp dsDNA fragment, and (right) unmodified HRP. DNA conjugation to position 1 (Lys150) is shown, with position 2 (Lys175) also indicated. The green area on HRP indicates the substrate binding area. Bottom: Simulation results for HRP and HRP(DNA) at positions 1 and 2.

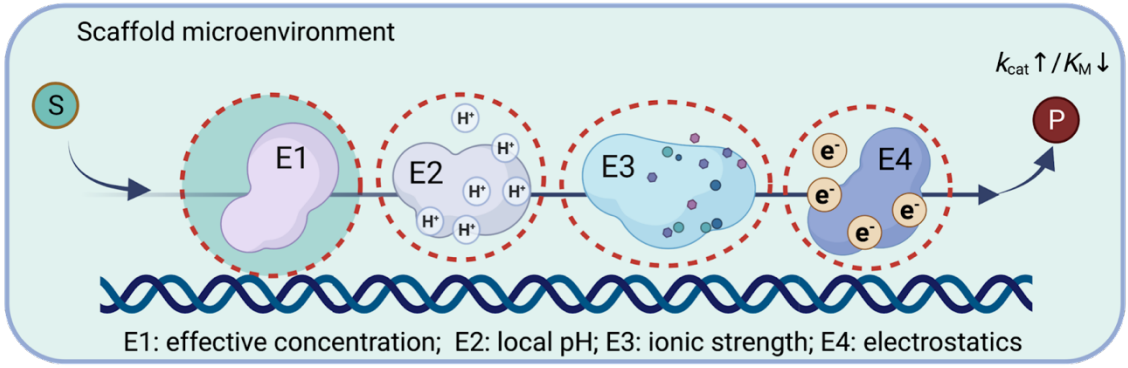

Figure 1.3 The local chemical and physical environment of a multienzyme scaffold can alter the kinetics of one or more of the assembled enzymes, thus increasing cascade activity. The effects that the microenvironment can have on enzyme activity and kinetics are shown, including increased effective substrate concentration (E1), beneficial pH and ionic strength (E2 and E3, respectively), and electrostatic interactions (E4). In many cases enhanced cascade activity is likely due to one or more of these effects as well as the potential enhancement from engineered substrate channeling. A DNA scaffold is shown here as an example, but the scaffold could also be protein-, lipid-, or polymer-based.

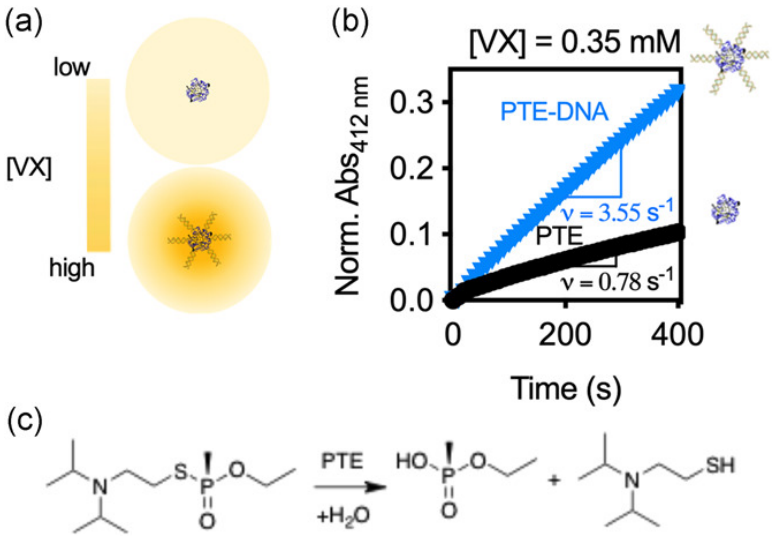

Figure 1.4 Nanoscale DNA scaffolds increase the local concentration and initial reaction rate of VX hydrolysis by phosphotriesterase (PTE). (a) A schematic representation of the VX concentration profile in close proximity to PTE (top) and PTE modified with DNA scaffolds with μM binding to VX (bottom). (b) The time course reaction of VX hydrolysis by PTE-DNA and PTE. PTE-DNA is a covalent conjugate of PTE and a 20 bp double-stranded DNA fragment of defined sequence with predicted VX binding ($K_{d,VX\text{-}DNA} = 120 \pm 10$ μM). The reaction was monitored using Ellman's reagent (Abs412 nm) to quantify the production of free thiol groups from the VX hydrolysis reaction shown in (c). Reaction conditions: 0.35 mM VX, 0.75 mM Ellman's reagent (5,5′-dithiobis 2-nitrobenzoic acid), and 1-2 mg of PTE or PTE-DNA. Reported absorbance values were normalized to the amount of PTE and PTE-DNA added to the reaction.

Chapter 2. Molecular Binding Scaffolds Increase Local Substrate Concentration Enhancing the Enzymatic Hydrolysis of VX Nerve Agent [1]

2.1 Abstract

Kinetic enhancement of organophosphate hydrolysis is a long-standing challenge in catalysis. For prophylactic treatment against organophosphate exposure, enzymatic hydrolysis needs to occur at high rates in the presence of low substrate concentrations and enzymatic activity should persist over days and weeks. Here, the conjugation of small DNA scaffolds was used to introduce substrate binding sites with micromolar affinity to VX, paraoxon, and methyl-parathion in close proximity to the enzyme phosphotriesterase (PTE). The result was a decrease in K_M and an increase in the rate at low substrate concentrations. An optimized system for paraoxon hydrolysis decreased K_M by 11-fold, with a corresponding increase in the second-order rate constant. The initial rates of VX and methyl-parathion hydrolysis were also increased by 3.1- and 6.7-fold, respectively. The designed scaffolds not only increased the local substrate concentration, but they also resulted in increased stability and PTE-DNA particle size tuning between 25 and ~150 nm. The scaffold engineering approach taken here is focused on altering the local chemical and physical microenvironment around the enzyme and is therefore compatible with active site engineering via combinatorial and computational approaches.

---

[1] This chapter previously appeared as an article in *Biotechnology and Bioengineering*. The original citation is as follows: Hong X, Lang X, Baker CA, Otto TC, Wheeldon I. Molecular binding scaffolds increase local substrate concentration enhancing the enzymatic hydrolysis of VX nerve agent. *Biotechnol Bioeng*. 2020 Jul;117(7):1970-1978. doi: 10.1002/bit.27346. Epub 2020 Apr 16. PMID: 32239488.

2.2 Introduction

Organophosphates are some of the most toxic compounds. The nerve agents VX and sarin are deadly at levels as low as 10 mg per kg and ~100 μg per kg of body mass, respectively [1,2]. The toxicity comes from the rapid inhibition of synaptic acetylcholinesterase (AChE) as the phosphate leaving group from the organophosphate cleavage reaction covalently binds to the active site serine. The result is cholinergic shock, paralysis, and in cases of severe toxicity, death. Other organophosphate derivatives such as azinphos, chlorpyrifos, and diazinon are used for pest control on food and commodity crops worldwide [3]. Persistence in the environment after agricultural use is limited, but more than 100,000 deaths per year result from organophosphate poisoning, mostly from self-ingestion [4]. The model compounds paraoxon and parathion also have pesticidal activity and are commonly used as model compounds for chemical warfare agents.

One strategy to combat organophosphate poisoning is biocatalytic scavenging. Catalytic scavenging works to prevent AChE inhibition by hydrolyzing the toxic organophosphate before binding in the active site of AChE. High turnover at low substrate concentrations is critical because the most harmful organophosphates are highly toxic even with low doses. A days- to weeks-long period of high activity is a goal for prophylactic treatments for personnel with high risk of exposure.

Phosphotriesterase (PTE), serum paraoxonase/arylesterase (PON1) and other similar enzymes are promising candidates for biocatalytic scavenging due to their high activity toward organophosphate hydrolysis [5–7]. Active site engineering has improved

reaction kinetics, with some enzymes reaching the estimated minimum second order rate constant for effective scavenging of 1 x 10^7 M^{-1} min^{-1} [8]. PEGylation has produced PTE conjugates with multi-day circulation in animal models, but this can come at the cost of reduced kinetics [9,10] . PTE-polymer conjugates also increase in vivo stability, in some cases with only minimal kinetic penalty [11–13]. Despite these advances, a technology gap remains and methods to enhance kinetics at low substrate concentrations, tune enzyme-particle size, and increase stability are still needed.

We recently discovered that paraoxon, methyl-parathion, and other organophosphates bind to double stranded DNA in a sequence-dependent manner [14]. We leveraged the binding interactions between an organophosphate and DNA conjugated to PTE to increase the local substrate concentration, thus increasing reaction rates under non-saturating conditions [15,16]. DNA scaffolds were also selected because DNA can be used to create nanoscale structures, the base pair sequence is tunable, and such scaffolds have been shown to resist degradation by proteolytic enzymes [17] . Given these characteristics, we created a series of PTE-DNA conjugates made from sequence-tunable DNA nanostructures, including short double stranded fragments and nanoscale DNA DX tiles, dual helix structures that are commonly used as building blocks in nanotechnology [18,19]. Conjugation of the structures to PTE had the intended effect: reaction kinetics with the tested organophosphates VX, paraoxon, and parathion-methyl were enhanced through a reduction in the apparent Michaelis constant and a corresponding increase in the second order rate constant. We demonstrate that this effect is dependent on the binding interactions between substrate and conjugated DNA scaffold, enzyme-DNA size is tunable, and PTE

modification with the DNA scaffolds increased catalytic stability in simulated in vivo conditions.

2.3 Results and Discussion

Figure 2.1a depicts the DNA scaffolding concept where PTE is modified with 20-80 base pairs (bp) of double stranded DNA or DNA DX tiles [19] with micromolar-range binding to the substrate of interest (Figure 2.1). The predicted and experimentally determined dissociation constants (K_d) for each DNA structure are shown in Table 2.1. PTE-DNA conjugates were synthesized with bifunctional NHS-ester/maleimide crosslinkers that joined thiolated DNA to free lysine side chains on the surface of PTE. This synthesis method produced conjugates with 12-14 DNA scaffolds per PTE dimer (Figure S2.1). The effect of DNA conjugation on the initial reaction rate is shown for the hydrolysis of VX (Figures 2.1b and c), which binds to the conjugated double stranded DNA (dsDNA) with a predicted dissociation constant of 120 ± 10 μM (DNA1; see Table 2.1 and Figure S2.2). In the absence of DNA, hydrolysis was slow in the presence of 0.35 mM VX, 0.52 ± 0.04 s^{-1}. Modification with the designed 20 bp DNA fragment increased the initial rate by 3.1-fold to 1.5 ± 0.7 s^{-1}. Given this result, we explored the effect of organophosphate-DNA binding strength on PTE kinetics. The initial rate of VX hydrolysis increased with decreasing $K_{d\,VX\text{-}DNA}$ (Figures 2.2 a and S2.3). The maximum working range of VX available to us was not sufficient to produce a full kinetic curve for the selected PTE mutant (Figure S2.3), which is consistent with the reported ~5 mM K_M for VX [20]. It is important to note that VX is highly toxic and should not be used outside of certified

laboratories. In this work, all VX experiments were performed at the U.S. Army Medical Research Institute of Chemical Defense. Concentration limitations established for research with surety materials in the U.S. Army Medical Research Institute of Chemical Defense prevented substrate saturation studies with VX, we were not able to complete a full kinetic analysis and turned to a model organophosphate compound to investigate the mechanisms of the observed enhancement.

In our previous work [14], we defined and characterized a series of DNA structures with experimentally validated dissociation constants for paraoxon ranging from 1.4±0.8 μM to 287±14 μM (here labeled DNA3-7; Table 2.1 and Figure S2.4). Paraoxon binding was found to primarily occur in the major and minor grooves of the double helix structure and binding strength varied by bp-sequence and structure (double stranded fragments bound less tightly than the designed DNA tiles). This series of molecular binding scaffolds created a system with tunable binding strength to evaluate the relationship between PTE kinetics and the binding function of the DNA (Figures 2.2b and c). In all cases, conjugation had no effect on k_{cat} (e.g., PTE-DNA3, k_{cat} = 2180±124 s^{-1}; and, PTE, k_{cat} = 2255±260 s^{-1}; Table 2.2). Kinetic enhancement was found to occur through a specific reduction in K_M. As the K_d of paraoxon to DNA decreased so did the apparent Michaelis constant, $K_{M,APP}$, of PTE-DNA. Unmodified PTE exhibited a K_M of 71±16 μM, a value consistent with other reports of this PTE variant [21]. Conjugation to the weak binding DNA4 reduced the observed K_M to 38±4 μM. The strongest binder, DNA7 reduced $K_{M,APP}$ for PTE-DNA by 10.8-fold to 6.6±0.7 μM. Similar fold-reductions were also achieved with DNA6 ($K_{d\ paraoxon\text{-}DNA}$ = 3.3±0.3 μM) and with DNA3 ($K_{d\ paraoxon\text{-}DNA}$ = 6.9±1.5 μM). We also tested the DNA

scaffolding approach with the organophosphate methyl-parathion and observed a 6.7-fold reduction in $K_{M,APP}$ with a parathion K_d to the conjugated DNA of 20±2 μM (Figure S2.5). Given the significant enhancement with DNA3 and the relative ease of producing PTE-DNA3 over PTE modified with multi-stranded DX tiles (DNA6 and -7), all subsequent investigations into the mechanisms of kinetic enhancement were accomplished with PTE modified with DNA3 and concatenations of DNA3 from 20 to 80 bp.

We hypothesize that the binding interactions between enzyme substrate and the DNA structures conjugated to the enzyme result in higher substrate concentration in close proximity to the enzyme in comparison to the bulk environment. Molecular dynamics simulations of a model HRP-DNA system support this hypothesis [15]. Given an appropriately selected control, it should also be possible to support this hypothesis experimentally for organophosphates and PTE-DNA. To this end, we identified an organophosphate with very weak predicted binding to DNA, 2,2-dichlorovinyl dimethyl phosphate (DDVP; Table 2.1). Full kinetic analysis of PTE and PTE-DNA3 revealed equivalent kinetics with DDVP (Table 2.2 and Figure S2.6).

The putative increase in local concentration can also be observed by evaluating the association of substrate to enzyme, k_1 (Eqn. 1).

$$E + S \underset{k_{-1}}{\overset{k_1}{\rightleftharpoons}} ES \overset{k_2}{\rightarrow} E + P \qquad (1)$$

The on-rate, k_1, can be determined for diffusion limited enzymes by comparing the apparent second order rate constant, k_{app} (k_{cat}/K_M), with decreasing substrate diffusion

coefficient through the addition of glycerol (or other inert viscous additive) to the reaction mixture [22,23]. We do not anticipate that the intrinsic on-rate is modified, but that an increase in local concentration would increase the rate of collision between substrate and active site resulting in an apparent increase in k_1 for PTE-DNA over k_1 for unmodified PTE. With DDVP as a substrate, k_1 for PTE and PTE-DNA3 were statistically similar. The binding function of the DNA can be seen with paraoxon hydrolysis, which exhibited an apparent on-rate, $k_{1,app}$, ~12-fold higher with PTE-DNA than with PTE alone.

The data thus far reveals two effects. One, that introducing DNA scaffolds with substrate binding interactions can decrease $K_{M,APP}$. Two, that the suppression of K_M increases with stronger binding between the substrate and DNA. Changing substrates to one with no binding to the scaffold underscores the mechanism of enhancement. A comparison of PTE-DNA activity with paraoxon and parathion suggests a third trend: PTE-DNA3 catalysis of parathion exhibited a k_{cat} of 220 s^{-1} and a second order rate constant ($k_{cat}/K_{M,APP}$) of 2.47×10^6 M^{-1} s^{-1}, and achieved a 6.7-fold reduction in $K_{M,APP}$; a 10.8-fold reduction in $K_{M,APP}$ was realized with PTE-DNA7 hydrolysis of paraoxon with a k_{cat} = 2185 s^{-1} and a second order rate constant of 3.3×10^8 M^{-1} s^{-1}. Given the difference in kinetic enhancement with different intrinsic turnover rates, we used a set of known PTE mutations to create a series of variants with maximum turnover (k_{cat}) that spans from 103±4 to 2250±110 s^{-1} (Figure S2.7). The k_{cat} of each PTE mutant modified with DNA3 is shown in Figure 2.4 along with the corresponding enhancement in $K_{M,APP}$. Fold enhancement increased with k_{cat}, reaching 6.6-fold with a turnover of 2250 s^{-1}. The system was limited to a ~2-fold increase with k_{cat} of 346±11 and 103±4 s^{-1}. This result suggests a possible

correlation between the limits of K_M enhancement and k_{cat}. Of note, is that there was no observed correlation between K_M enhancement and intrinsic PTE K_M (Figure S2.7).

DNA as a scaffold also proved valuable in addressing stability and particle size tuning. The conjugation of increasing lengths of DNA including the 20 bp of DNA3 and two, three, and four repeats of the sequence, had no statistically significant effect on kinetics (Figure 2.5a and S2.8). $K_{M,APP}$ was reduced and k_{cat} remained constant across the PTE-DNA set. Modification with DNA3 and $(DNA3)_4$ also increased enzyme stability (Figure 2.5b). After 48 hrs in 50% fetal bovine serum (FBS) and PBS at 37 °C, PTE modified with DNA3 and $(DNA3)_4$ maintained 53±9% and 57±5% of their initial activity, respectively. Conjugation with PEG, a common method of increasing stability, resulted in a greater loss of activity with only 13±1% remaining while unprotected PTE lost 90% of its initial activity towards paraoxon (Figure 2.5b and S2.9). The increase in PTE-DNA stability over unmodified PTE is likely due to increased resistance to protease attack as has been observed with other enzyme-DNA nanostructures [13,24]. It is also possible that the conjugated DNA scaffolds increase the barrier to protein unfolding at elevated temperatures.

In addition to the increase in stability, DNA fragments of various lengths were used to create a series of PTE-DNA particles of increasing size. The addition of 20, 40, 60, and 80 bp scaffolds (DNA3, $(DNA3)_2$, $(DNA3)_3$, $(DNA3)_4$) increased the hydrodynamic diameter of PTE as measured by dynamic light scattering (DLS) from ~12 nm to upward of 150 nm (Figure 2.5c). We note that the repetitive nature of the 40 to 80 bp sequences

may lead to DNA fragments that are longer than the prescribed length due to oligomer binding that is not matched end-to-end with the template strand.

Here, we show that PTE modified with rationally designed DNA scaffolds creates an organophosphate hydrolysis system with tunable particle size, enhanced stability at *in vivo* temperature, and high catalytic rates at low substrate concentrations. Enzyme particles with diameters between 100 and 200 nm are preferred for *in vivo* circulation applications because foreign bodies less than ~100 nm are quickly cleared from the bloodstream and particles greater than ~200 nm typically collect in the liver after short periods of time [20,25]. PTE-DNA with 60 to 80 bp fragments span the optimal range (Figure 2.5c) but additional experiments are necessary to determine optimal structures for both *in vivo* and *in vitro* applications. Finally, the conjugates increased reaction rates at low substrate concentration where organophosphates already have toxic effects.

The kinetic enhancement due to the DNA-enzyme conjugate comes about through an increase in local substrate concentration. The decrease in $K_{M,APP}$ with increasing binding strength supports this conclusion (Figure 2.2). Similarly, the increase in observed on-rate results from high local substrate concentrations (Figure 2.3). Our previous simulations of a model HRP-DNA system are also supportive of the hypothesis. Simulation of the system shows that binding to the conjugated DNA can increase the residence time of a substrate molecule in close proximity to the active site [15].

One possible alternative is that the high negative charge density of the DNA creates a microenvironment with a lower pH than the bulk environment, a phenomenon that has

been suggested as the mechanism of enhanced catalysis with HRP and GOx/HRP cascade reactions assembled on DNA nanostructures [26]. Two control experiments suggest that this is not the case for PTE-DNA: (1) In all PTE-DNA cases the k_{cat} remains statistically equivalent to unmodified PTE (Figure 2.2 and Table 2.1); and (2) The DDVP control experiment that removed DNA binding interactions from the PTE-DNA system showed identical kinetics to PTE alone (Figure 2.3).

Our approach is one of an increasing number of strategies designed to enhance enzyme catalysis by engineering the enzyme microenvironment [27]. For example, a series of recent studies developed and optimized a PTE-DNA-Au nanoparticle system that enhances k_{cat} by altering the reaction mechanism [28–30]. PTE-Protein hydrogel systems also modified reaction kinetics by altering the local chemical environment [31,32]. Our approach uses molecular scaffolds to add new chemical and physical features to the surface of an enzyme. When rationally designed, the scaffolds alter the local environment with a predictable effect on enzyme kinetics. We realized this concept by enhancing the kinetics of VX, paraoxon, and methyl-parathion hydrolysis by PTE-DNA nanostructures. An optimized system for paraoxon hydrolysis reduced $K_{M,APP}$ by 11-fold with an equivalent increase in the second order rate constant to more than 3.3×10^8 M^{-1} s^{-1}, above the target goals of *in vivo* bioscavenging. Hydrolysis of VX was also enhanced by more than 3-fold. This new enzyme engineering strategy is locally applied and is not specifically directed towards the active site, thus enabling tandem approaches with rate and selectivity enhancement through active site engineering and additional kinetic enhancements and tunable physical properties achieved with molecular scaffolds.

2.4 Materials and Methods

Chemicals. Kanamycin, Luria-Bertani (LB) broth, 10×PBS buffer, Tris-Base, dithiothreitol (DTT) and ethanol were purchased from Fisher BioRegents. Sodium chloride was purchased from Fisher Chemical. Sulfosuccinimidyl 4-(N-maleimidomethyl) cyclohexane-1-carboxylate (Sulfo-SMCC), 10 and 30 kDa filters (UFC801024, UFC803024), and SOB medium were purchased from Thermo Fisher Scientific. Paraoxon, methyl-parathion, zinc chloride, 2,2-dichlorovinyl dimethyl phosphate (DDVP), 2-Thiobarbituric acid (TBA), O-(2-Mercaptoethyl)-O'-methyl-polyethylene glycol (10 kDa thiolated PEG), fetal bovine serum (FBS), and ammonium sulfate (A4418) were obtained from Sigma-Aldrich. 4-nitrophenol was purchased from Acros. 0.2 μM filters were purchased from Corning and sodium acetate was purchased from Fisher Scientific.

Phosphotriesterase (PTE) cloning, expression, and purification. PTE and PTE mutant genes were inserted into pET-28b(+) plasmid backbone (Figure S10) via Gibson assembly. Expression plasmids were transformed into BL21DE 3(+) cells for expression in 250 mL of sterilized LB broth with 100 μg mL^{-1} kanamycin and 0.5 mM $ZnCl_2$ in 1 L shake flasks. Cultures were inoculated with 3.75 mL overnight culture at 37 °C. PTE expression was induced with 0.5 mM IPTG at an OD_{600} 0.6. Post induction cultures were moved to a 20 °C shaker incubator and expression continued for 48 hours.

All purification steps were carried out at 0-4 °C. Cells were harvested by centrifugation at 5000 g for 20 min and 4°C and the recovered cell pellets were re-suspended in 100 mL Tris-base buffer (50 mM Tris, 100 μM $ZnCl_2$, pH 8.5). After

sonication, clarified lysates were obtained by centrifugation at 15000 g for 30 min at 4°C. Soluble protein fractions were first isolated purified by ammonium sulfate precipitation, with PTE identified in the 30%-45% fraction. Two rounds of ammonium sulfate precipitation were completed prior to buffer exchange and PTE isolation by anion exchange chromatograph (HiPrep DEAE FF 16/10) in pH 8.5, 50 mM Tris buffer. Finally, PTE samples were subject to size exclusion chromatography in PBS (Superdex 200 Increase 10/300 GL). Protein samples were filtered through 0.22 μM filters prior to all liquid chromatography steps, and when necessary, PTE samples were concentrated, and buffer exchanged to PBS by filtration over a 30 kDa filter.

PTE-DNA and PTE-PEG conjugation. PTE-DNA conjugates were obtained by crosslinking thiolated single stranded DNA (IDT-DNA) and surface accessible lysine side chains on PTE with the bifunctional crosslinker Sulfo-SMCC. Prior to reaction, the 5' thiolated DNA was activated as follows. First, 20 mL 1 mM 5' thiolated ssDNA was reduced by incubating with 120 μL of 1M DTT for three hours at room temperature. Post reduction, excess DTT was removed by centrifugation (4 °C, 15000 g, 30 mins) after overnight precipitation at -20 °C in ethanol with sodium acetate (0.1 sample volumes of 3 M sodium acetate and 2.5 sample volumes ice cold 100% ethanol). After precipitation, the DNA pellet was washed twice with 0.5 mL of ice cold 75% ethanol. The washed DNA was collected by centrifugation at 15000 g and 4 °C for 30 mins. Second, the thiolated DNA was reacted with Sulfo-SMCC at room temperature for three hours in the absence of light. Excess extra Sulfo-SMCC was removed as described for DTT removal.

Thiolated PEG did not require activation and was directly reacted with the Sulfo-SMSS crosslinker. Briefly, PEG (O-(2-Mercaptoethyl)-O'-methyl-polyethylene glycol, MW:10000) was stored in inert gas at room temperature prior to reaction. The thiolated PEG was reacted with Sulfo-SMCC in pH 7.4, PBS buffer for 3 hours at room temperature. During the reaction Sulfo-SMCC was present in 5-fold excess to the thiolated PEG. Post reaction, extra Sulfo-SMCC was removed by filtration over 3 kDa filter.

Purified PTE and activated ssDNA were mixed at a ratio of 1:100, and the conjugation reaction was carried out at room temperature for three hours, again in the absence of light. Post conjugation, excess DNA was removed by size exclusion chromatography (Superdex 200 Increase 10/300 GL) using a PBS buffer. PTE-ssDNA complexes were then concentrated and buffer exchanged to TBS (20 mM Tris, 120 mM NaCl, pH 7.4) by filtration over a 30 kDa filter. Final PTE-DNA conjugates with double stranded DNA were then produced by incubating PTE with conjugated ssDNA with equal molar concentration of a complementary DNA strand or with DNA tiles with the complementary sticky end. PTE-PEG conjugates were obtained in a similar manner.

Tiles were assembled from the ssDNAs listed in Figure S5 and assembly was carried out in 200 μM TAE-Mg^{2+} buffer (40 mM, pH 8.0, Tris-acetic acid; 2 mM EDTA·Na_2; 12.5 mM magnesium acetate). Briefly, tiles strands were mixed together in an equal molar ration and heated to 95 °C for 5 min followed by cooling at 65 °C, 50 °C, 37 °C and room temperature for 20 mins at each temperature. Assembled tiles were analyzed and recovered by SDS-PAGE.

Enzymatic VX hydrolysis. All VX experiments were carried out by the co-authors at the U.S. Army Medical Research Institute of Chemical Defense (USAMRICD, Aberdeen Proving Ground, MD). VX was obtained from the U.S. Army Combat Capabilities Development Command Chemical Biological Center (Aberdeen Proving Ground, MD). Briefly, enzyme samples (n=3) were incubated in PBS, pH 7.4 in the presence of 2.8 mM 5,5'-dithiobis(2-nitro-benzoic acid) (Ellman's reagent) and a range of VX concentrations from 0.011 mM to 1.4 mM in 96 well microtiter plates. Enzyme turnover was followed by monitoring the absorbance at 412 nm in a UV/VIS SpectraMax Plus 384 spectrophotometer (Molecular Devices, San Jose, CA) for 1 h at room temperature. All measurements were normalized by the concentration of PTE in each sample.

PTE, PTE-DNA, and PTE-PEG kinetic assays. All kinetic assays were accomplished in 96 well microtiter plates at room temperature. Organophosphate hydrolysis was carried out in 150 mL of pH 7.4, PBS buffer with 20 nM of enzyme and 5, 10, 20, 40, 80, and 100 mM paraoxon, 50, 100, 250, 500, 1000, 2000, 300 mM methyl-parathion, and 0, 50, 100, 200, 400, 800 mM DDVP. Activity towards paraoxon and methyl-parathion was monitored by measuring the absorbance of the p-nitrophenol leaving group at 405 nm (BioTek Synergy Neo). The extinction coefficient of p-nitrophenol at 405 nm was determined to 12920 $cm^{-1}M^{-1}$ under the reaction buffer conditions (Figure S11). DDVP hydrolysis was monitored by measuring the absorbance at 490 nm after the addition of TBA (final concentration, 2 mM) and acetic acid (final concentration, 30 % (v/v)), and heating for 1 hour at 100 °C (GuzmanChozas, Vicario, & GuillenSans, 1997). A minimum of three replicates was performed for each kinetic assay.

Determining organophosphate-PTE on-rate. Organophosphate hydrolysis in solutions of increasing viscosity was accomplished by adding 0, 1, 5, 10, 20, and 30 % glycerol (v/v) to the reaction mixture. Reactions were carried out with 200 mM paraoxon or 1 mM DDVP and 20 nM of enzyme. All the viscosity-dependent experiments were carried out in 96 well microtiter plates and each reaction was conducted in triplicate.

PTE and PTE-DNA stability assay. Stability assays were conducted in a similar manner to the kinetic analysis, but with 10 mM PTE/PTE-DNA/PTE-PEG. Enzyme in pH 7.4 1×PBS was mixed with an equal volume of FBS. The reaction mixture was then incubated at 37 °C for 0, 2, 4, 8, 24, 48 hours. After incubation at 37 °C for different times, the residual enzyme activity of PTE/PTE-DNA/PTE-PEG was measured with 200 mM paraoxon in pH 7.4 1XPBS at room temperature. The residual enzyme activity was presented by the fraction of activity left compared to time zero.

Substrate-DNA docking simulation. The binding affinity between VX, DDVP and double stranded DNA (dsDNA) was predicted by Autodock 4.2 simulation software (Morris et al., 2009). DNA structures were created using the 3D-DART Web server, and polar hydrogen atoms and Kollman charges were assigned by Autodock (van Dijk & Bonvin, 2009). The chemical structures of VX and DDVP were obtained from the online ChemSpider database, and hydrogen atoms and Gasteiger charges were assigned using VEGA ZZ (Pedretti, Villa, & Vistoli, 2004). Simulation by Autodocking used a Lamarckian 4 genetic algorithm. All simulations were conducted for at least 70 runs and were repeated in triplicate.

Dynamic light scattering (DLS). The diameters of PTE-DNA conjugates were determined by DLS (Beckman Coulter-Delsa Nano C). The DLS measurement was carried in a 1x PBS buffer at room temperature with 100 pin. Briefly, purified enzyme samples were concentrated to 5 g L^{-1} in PBS. Each DLS measurement required 0.5 mL and measurements were compared to a blank sample of PBS.

2.5 Acknowledgments

This study was supported by HDTRA1-14-1-0045 and by the Army Research Office MURI #W911NF1410263 to IW, and through a cooperative research and development agreement between the University of California Riverside and the USAMRICD. The views expressed in this manuscript are those of the author(s) and do not reflect the official policy of the Department of Army, Department of Defense, or the U.S. Government.

2.6 Reference

1. Grob, D. & Harvey, J. C. EFFECTS IN MAN OF THE ANTICHOLINESTERASE COMPOUND SARIN (ISOPROPYL METHYL PHOSPHONOFLUORIDATE)1. *Journal of Clinical Investigation* vol. 37 350–368 (1958).

2. Thiermann, H., Worek, F. & Kehe, K. Limitations and challenges in treatment of acute chemical warfare agent poisoning. *Chem. Biol. Interact.* **206**, 435–443 (2013).

3. Sidhu, G. K. *et al.* Toxicity, monitoring and biodegradation of organophosphate pesticides: A review. *Critical Reviews in Environmental Science and Technology* vol. 49 1135–1187 (2019).

4. Eddleston, M. Novel Clinical Toxicology and Pharmacology of Organophosphorus Insecticide Self-Poisoning. *Annual Review of Pharmacology and Toxicology* vol. 59 341–360 (2019).

5. Evolved Stereoselective Hydrolases for Broad-Spectrum G-Type Nerve Agent Detoxification. *Chem. Biol.* **19**, 456–466 (2012).

6. Pang, Z. *et al.* Detoxification of Organophosphate Poisoning Using Nanoparticle Bioscavengers. *ACS Nano* **9**, 6450–6458 (2015).

7. Tsai, P.-C. *et al.* Enzymes for the homeland defense: optimizing phosphotriesterase for the hydrolysis of organophosphate nerve agents. *Biochemistry* **51**, 6463–6475 (2012).

8. Gupta, R. D. *et al.* Directed evolution of hydrolases for prevention of G-type nerve agent intoxication. *Nature Chemical Biology* vol. 7 120–125 (2011).

9. Efremenko, E. N. *et al.* A simple and highly effective catalytic nanozyme scavenger for organophosphorus neurotoxins. *J. Control. Release* **247**, 175–181 (2017).

10. Daffu, G. K. *et al.* Sulfhydryl-specific PEGylation of phosphotriesterase cysteine mutants for organophosphate detoxification. *Protein Engineering Design and Selection* vol. 28 501–506 (2015).

11. Ilyushin, D. G. *et al.* Chemical polysialylation of human recombinant butyrylcholinesterase delivers a long-acting bioscavenger for nerve agents in vivo. *Proceedings of the National Academy of Sciences* vol. 110 1243–1248 (2013).

12. Novikov, B. N., Grimsley, J. K., Kern, R. J., Wild, J. R. & Wales, M. E. Improved pharmacokinetics and immunogenicity profile of organophosphorus hydrolase by chemical modification with polyethylene glycol. *Journal of Controlled Release* vol. 146 318–325 (2010).

13. Zhang, P. *et al.* Nanoscavenger provides long-term prophylactic protection against nerve agents in rodents. *Science Translational Medicine* vol. 11 eaau7091 (2019).

14. Gao, Y., Or, S., Toop, A. & Wheeldon, I. DNA Nanostructure Sequence-Dependent Binding of Organophosphates. *Langmuir* **33**, 2033–2040 (2017).

15. Gao, Y., Roberts, C. C., Toop, A., Chang, C.-E. A. & Wheeldon, I. Mechanisms of Enhanced Catalysis in Enzyme-DNA Nanostructures Revealed through Molecular Simulations and Experimental Analysis. *ChemBioChem* vol. 17 1430–1436 (2016).

16. Gao, Y. *et al.* Tuning Enzyme Kinetics through Designed Intermolecular Interactions Far from the Active Site. *ACS Catalysis* vol. 5 2149–2153 (2015).

17. Zhao, Z. *et al.* Nanocaged enzymes with enhanced catalytic activity and increased stability against protease digestion. *Nat. Commun.* **7**, 10619 (2016).

18. Jones, M. R., Seeman, N. C. & Mirkin, C. A. Programmable Materials and the Nature of the DNA Bond*. *Spherical Nucleic Acids* 167–197 (2020) doi:10.1201/9781003056676-7.

19. Li, X., Yang, X., Qi, J. & Seeman, N. C. Antiparallel DNA double crossover molecules as components for nanoconstruction. *J. Am. Chem. Soc.* **118**, 6131–6140 (1996).

20. Bigley, A. N., Xu, C., Henderson, T. J., Harvey, S. P. & Raushel, F. M. Enzymatic Neutralization of the Chemical Warfare Agent VX: Evolution of Phosphotriesterase for Phosphorothiolate Hydrolysis. *Journal of the American Chemical Society* vol. 135 10426–10432 (2013).

21. Roodveldt, C. & Tawfik, D. S. Directed evolution of phosphotriesterase from Pseudomonas diminuta for heterologous expression in Escherichia coli results in stabilization of the metal-free state. *Protein Eng. Des. Sel.* **18**, 51–58 (2005).

22. Brouwer, A. C. & Kirsch, J. F. Investigation of diffusion-limited rates of chymotrypsin reactions by viscosity variation. *Biochemistry* **21**, 1302–1307 (1982).

23. Nakatani, H. & Dunford, H. B. Meaning of diffusion-controlled association rate constants in enzymology. *The Journal of Physical Chemistry* vol. 83 2662–2665 (1979).

24. Wu, T. *et al.* A Nanobody-Conjugated DNA Nanoplatform for Targeted Platinum-Drug Delivery. *Angew. Chem. Int. Ed Engl.* **58**, 14224–14228 (2019).

25. Park, J.-H. *et al.* Biodegradable luminescent porous silicon nanoparticles for in vivo applications. *Nat. Mater.* **8**, 331–336 (2009).

26. Zhang, Y., Tsitkov, S. & Hess, H. Proximity does not contribute to activity enhancement in the glucose oxidase–horseradish peroxidase cascade. *Nature Communications* vol. 7 (2016).

27. Lancaster, L., Abdallah, W., Banta, S. & Wheeldon, I. Engineering enzyme microenvironments for enhanced biocatalysis. *Chem. Soc. Rev.* **47**, 5177–5186 (2018).

28. Breger, J. C. *et al.* Understanding How Nanoparticle Attachment Enhances Phosphotriesterase Kinetic Efficiency. *ACS Nano* **9**, 8491–8503 (2015).

29. Breger, J. C. *et al.* Assembling high activity phosphotriesterase composites using hybrid nanoparticle peptide-DNA scaffolded architectures. *Nano Futures* vol. 1 011002 (2017).

30. Samanta, A. *et al.* DNA–Nanoparticle Composites Synergistically Enhance Organophosphate Hydrolase Enzymatic Activity. *ACS Applied Nano Materials* vol. 1 3091–3097 (2018).

31. Lu, H. D., Wheeldon, I. R. & Banta, S. Catalytic biomaterials: engineering organophosphate hydrolase to form self-assembling enzymatic hydrogels. *Protein Eng. Des. Sel.* **23**, 559–566 (2010).

32. Campbell, E. C. *et al.* Hydrogel-Immobilized Supercharged Proteins. *Advanced Biosystems* vol. 2 1700240 (2018).

2.7 Figures and Tables

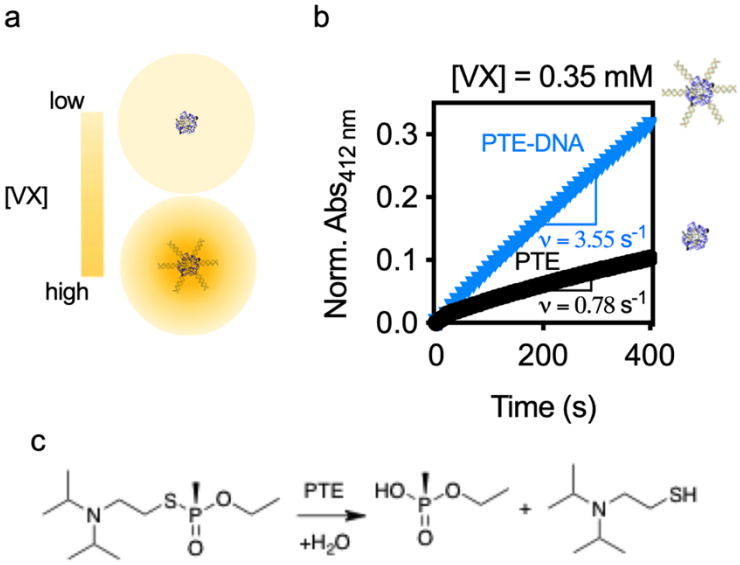

Figure 2.1 Nanoscale DNA scaffolds increase the local concentration and initial reaction rate of VX hydrolysis by phosphotriesterase (PTE). (a) A schematic representation of the VX concentration profile in close proximity to PTE (top) and PTE modified with DNA scaffolds with μM binding to VX (bottom). (b) The time course reaction of VX hydrolysis by PTE-DNA and PTE. PTE-DNA is a covalent conjugate of PTE and a 20 bp double-stranded DNA fragment of defined sequence with predicted VX binding ($K_{d,VX\text{-}DNA} = 120 \pm 10$ μM). The reaction was monitored using Ellman's reagent (Abs412 nm) to quantify the production of free thiol groups from the VX hydrolysis reaction shown in (c). Reaction conditions: 0.35 mM VX, 0.75 mM Ellman's reagent (5,5′-dithiobis 2-nitrobenzoic acid), and 1-2 mg of PTE or PTE-DNA. Reported absorbance values were normalized to the amount of PTE and PTE-DNA added to the reaction.

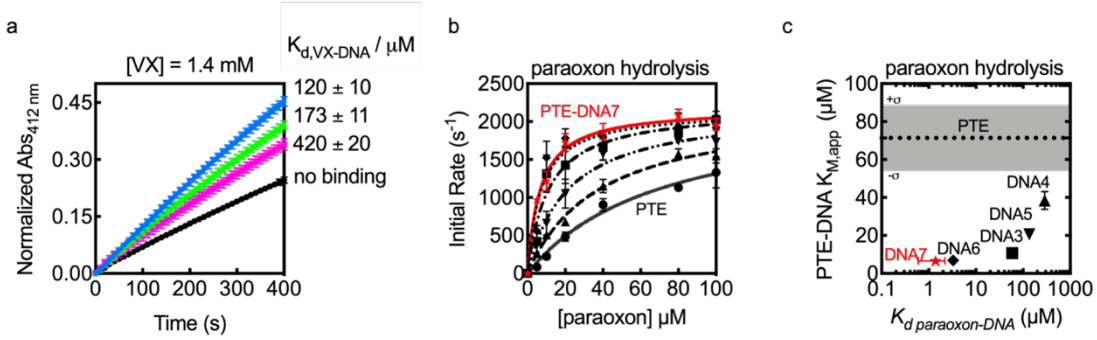

Figure 2.2 Binding interactions between phosphotriesterase (PTE) substrates and DNA scaffolds drive enhanced kinetics through a reduction in apparent Michaelis constant. (a) The reaction time course of VX hydrolysis by PTE-DNA and PTE with a range of VX-DNA predicted binding strengths. PTE was conjugated to three unique 20 bp double-stranded sequences (Table 2.1 and Figure S2.2). The reaction was monitored as described in Figure 2.1 but in this case with 1.4 mM VX and 2.8 mM Ellman's reagent. (b) Kinetic analysis of paraoxon hydrolysis by PTE and PTE-DNA. PTE was modified with 20 bp double-stranded DNA3 (■), DNA4 (▲), and DNA5 (▼), as well as two different DNA DX tiles DNA6 (♦), and DNA7 (★). All sequences are provided in Figure S4. Reactions were carried out in pH 7.4 phosphate-buffered saline (PBS) with 20 nM enzyme, and 0–100 µM paraoxon. (c) The apparent enzyme K_M ($K_{M,APP}$) as a function of paraoxon-DNA dissociation constant derived from the data presented in b. The Kd values were experimentally determined as measured by MicroScale Thermophoresis (MST), and are listed in Figure S2.4. All data points are the mean of three independent replicates with the error bars indicating the standard deviation.

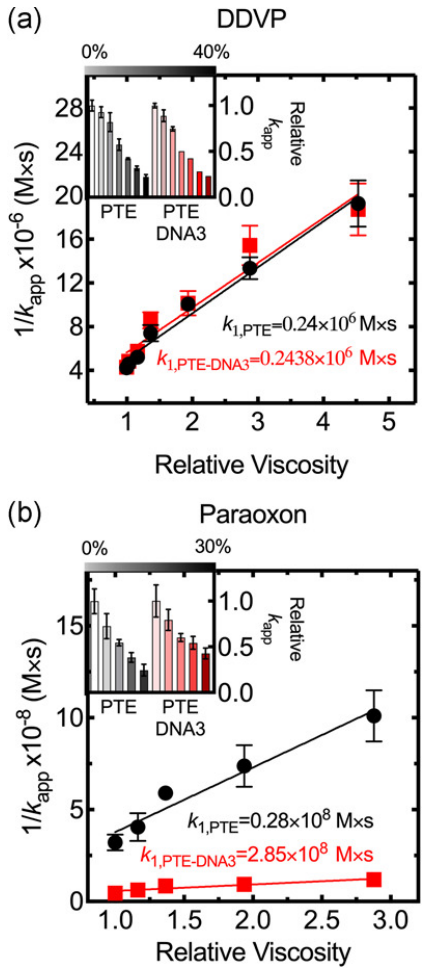

Figure 2.3 Diffusion-limited kinetic analysis of phosphotriesterase (PTE)-DNA and PTE with DNA binding and nonbinding substrates. The inverse of the observed second-order rate constant of 2,2-dichlorovinyl dimethyl phosphate (DDVP). (a) and paraoxon (b) hydrolysis with increasing reaction solution viscosity through the addition of glycerol. The insets show the relative second order rate constant, k_{app}, of PTE and PTE-DNA3 with 0%, 1%, 5%, 10%, 20%, 30%, and 40% glycerol. k1 is the slope of a linear fit to the inverse of the observed rate as a function of viscosity. Reaction conditions: 20 nM PTE or PTE-DNA, 200 μM substrate, pH 7.4 buffered with phosphate buffered saline (PBS), and variable concentration of glycerol to alter solution viscosity.

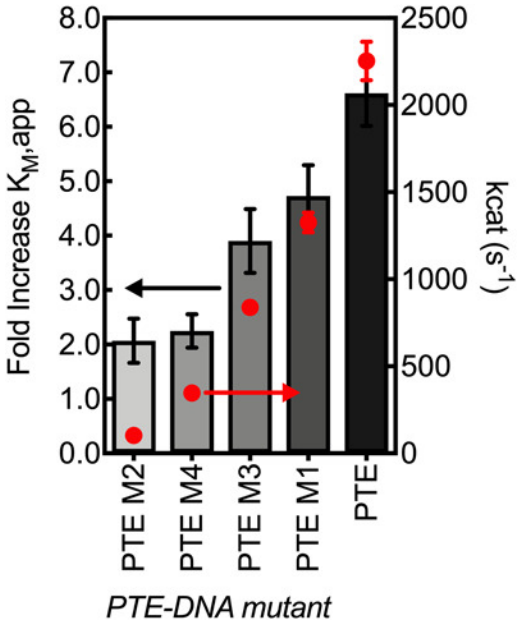

Figure 2.4 The $K_{M,\ app}$ fold increase (Bars, left y-axis) of phosphotriesterase (PTE)/PTE mutants after conjugation with DNA and the k_{cat} of PTE mutant (red dots, right y-axis). PTE is PTE(S5) from the Tawfik group with the series of mutants M1 (S319R), M2(S319R, R185K), M3(R185K), and M4(D208G). All experiments were conducted in triplicate.

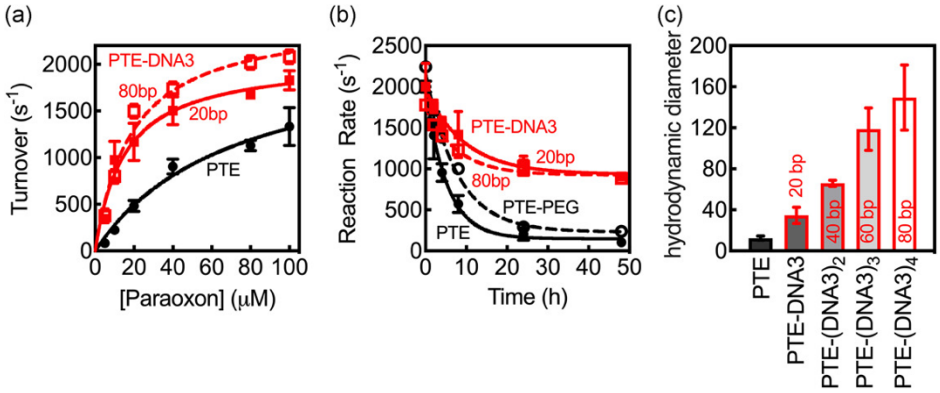

Figure 2.5 Kinetics and stability of sized controlled phosphotriesterase (PTE)-DNA. (a) Kinetic analysis of PTE, PTE-DNA3, and PTE-(DNA3)4; the subscript indicates the number of concatenations of 20 bp DNA3. Reactions were carried out in pH 7.4 phosphate-buffered saline (PBS) with 20 nM enzyme and 0–100 μM paraoxon. (b) Stability of PTE, PTE-DNA3, PTE-(DNA3)4, and PTE modified with 10 kDa PEG in 1:1 PBS and fetal bovine serum (FBS) at 37°C. Activity was measured with 200 μM substrate and 20 nM enzyme. (c) Size measurements by dynamic light scattering. Particle diameter is shown for PTE and PTE-DNA3, -$(DNA3)_2$, -$(DNA3)_3$, and -$(DNA3)_4$. All data points are the mean of three replicates and the standard deviation is shown as error bars.

Table 2.1 DNA nanostructure interactions with selected organophosphates.

	Kd (μM)	
	Predicted	Experimental
DNA1 (20 bp dsDNA)	120 ± 10 (VX)	n.d.
DNA2 (20 bp dsDNA)	174 ± 11 (VX)	n.d.
DNA3 (20 bp dsDNA)	33 ± 2 (paraoxon)	59 ± 6 (paraoxon)
		20 ± 2 (methyl-parathion)
	420 ± 21 (VX)	
	988 ± 70 (DDVP)	
DNA4 (20 bp dsDNA)	72 ± 6 (paraoxon)	287 ± 14 (paraoxon)
		90 ± 4 (methyl-parathion)
	238 ± 17 (VX)	
DNA5 (20 bp dsDNA)	132 ± 13 (paraoxon)	136 ± 3 (paraoxon)
		25 ± 2 (methyl-parathion)
	275 ± 19 (VX)	
DNA6 (Dx Tile)	n.d.	3.3 ± 0.3 (paraoxon)
DNA7 (Dx Tile)	n.d.	1.4 ± 0.8 (paraoxon)

Note: Dissociation constants were predicted by AutoDock simulation and experimental dissociation constants were determined by microscale thermophoresis.
Data are mean ± standard derivation.
Abbreviations: DDVP, 2,2-dichlorovinyl dimethyl phosphate; dsDNA, double-stranded DNA; n.d., not determined.

Table 2.2. Kinetic parameters for PTE and PTE-DNA with selected organophosphates

	Substrate	k_{cat} (s^{-1})	K_M (μM)
PTE	paraoxon	2253 ± 258	71 ± 16
	DDVP	56 ± 8	237 ± 83
	Methyl-parathion	212 ± 9	457 ± 62
PTE-DNA3 (dsDNA)	Paraoxon	2180 ± 124	11 ± 2
	DDVP	55 ± 4	240 ± 44
	Methyl-parathion	220 ± 6	85 ± 12
PTE-DNA4 (dsDNA)	Paraoxon	2224 ± 102	38 ± 4
PTE-DNA5 (dsDNA)	Paraoxon	2190 ± 93	21 ± 2.7
PTE-DNA6 (DX tile)	Paraoxon	2145 ± 108	6.9 ± 1.5
PTE-DNA7 (DX tile)	Paraoxon	2184 ± 49.0	6.6 ± 0.7

Abbreviations: DDVP, 2,2-dichlorovinyl dimethyl phosphate; dsDNA, double-stranded DNA; PTE, phosphotriesterase.
Data are mean ± standard derivation.

2.8 Supporting Information

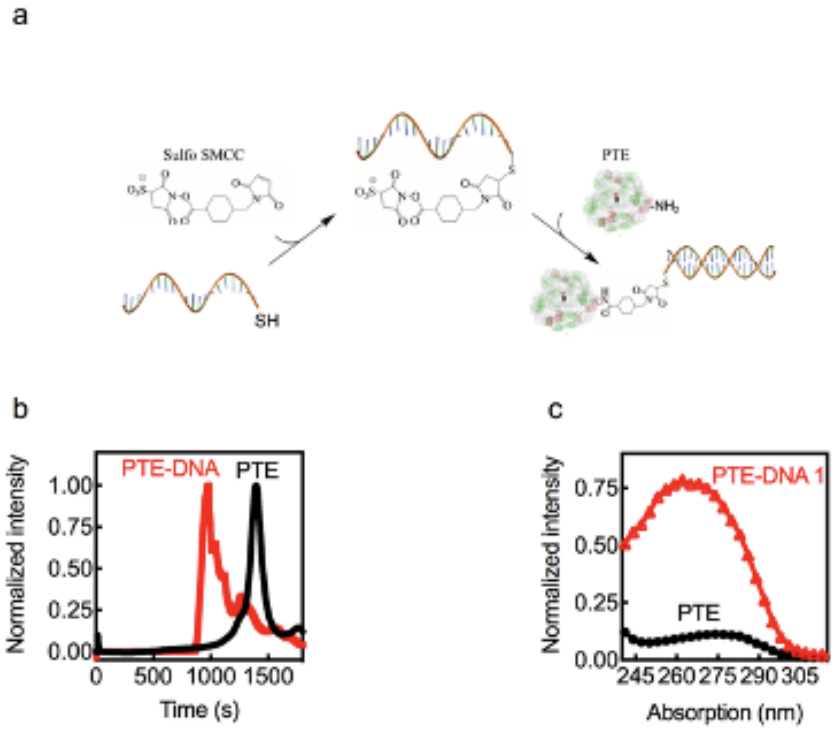

Figure S 2.1 PTE-DNA conjugation. (a) Chemical crosslinking strategy of PTE and DNA scaffolds, (b) Size exclusion chromatography of PTE and PTE-DNA1, (c) the absorbance spectrum of PTE and PTE-ssDNA1. The PTE and PTE-DNA1 absorbance spectrum was normalized based on the PTE concentration. The protein absorption peak of PTE (at 280 nm) is blue-shifted to 260 nm after DNA conjugation. The pathlength, $l = 0.5$mm, $\varepsilon_{260,PTE} = 24454\ M^{-1}cm^{-1}$, $\varepsilon_{260,DNA} = 193300\ M^{-1}cm^{-1}$, $\varepsilon_{280,PTE} = 29280 M^{-1}cm^{-1}$, and $\varepsilon_{280,DNA} = 96650\ M^{-1}cm^{-1}$. The PTE extinction coefficient was reported by Jackson et al. [1], the DNA extinction coefficient was determined by Integrated DNA Technology (IDTDNA). Analysis of 5 PTE-DNA samples resulted in an average value of 7.5±1.0 DNA modifications per PTE monomer. These modifications occur on a subset of the 26 surface accessible amine groups (see PDB:1hzy).

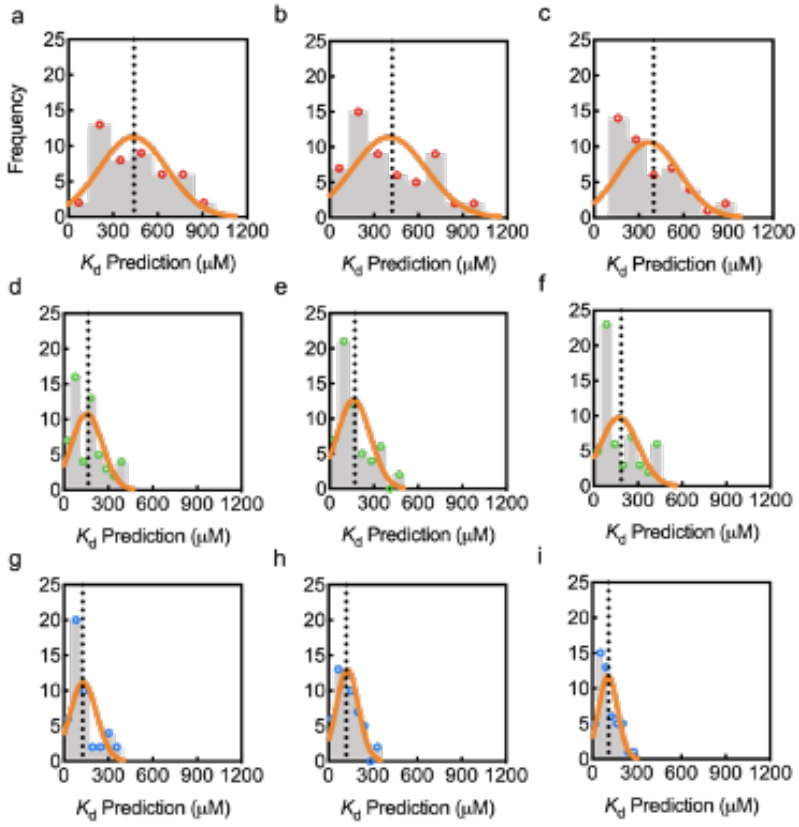

	Sequence	Predicated K_d (μM)
DNA1	ATAACTGTACATAACTGTAC	119.9±10.4
	GTACAGTTATGTACAGTTAT	
DNA2	AAGTCATCATAAGTCATCAT	173.6±11.3
	ATGATGACTTATGATGACTT	
DNA3	CAGGTTGCAGCAGGTTGCAG	420.2±20.8
	CTGCAACCTGCTGCAACCTG	

Figure S 2.2 The determination of K_d between different DNA fragments and VX by Autodock simulation. (a-c) The distribution of predicted K_d between DNA 1 and VX. (d-f) The distribution of predicted K_d between DNA 5 and VX. (g-i) The predicted distribution of K_d between DNA 39 and VX. (bottom) Summary of predicted K_d values or each DNA fragment. Autodock simulation experiments were carried out in triplicate for each DNA sequence, and 70 potential interactions were simulated for each simulation. The resulting 70 K_d predictions were organized in a histogram, and the peak value was determined as the K_d between DNA and VX.

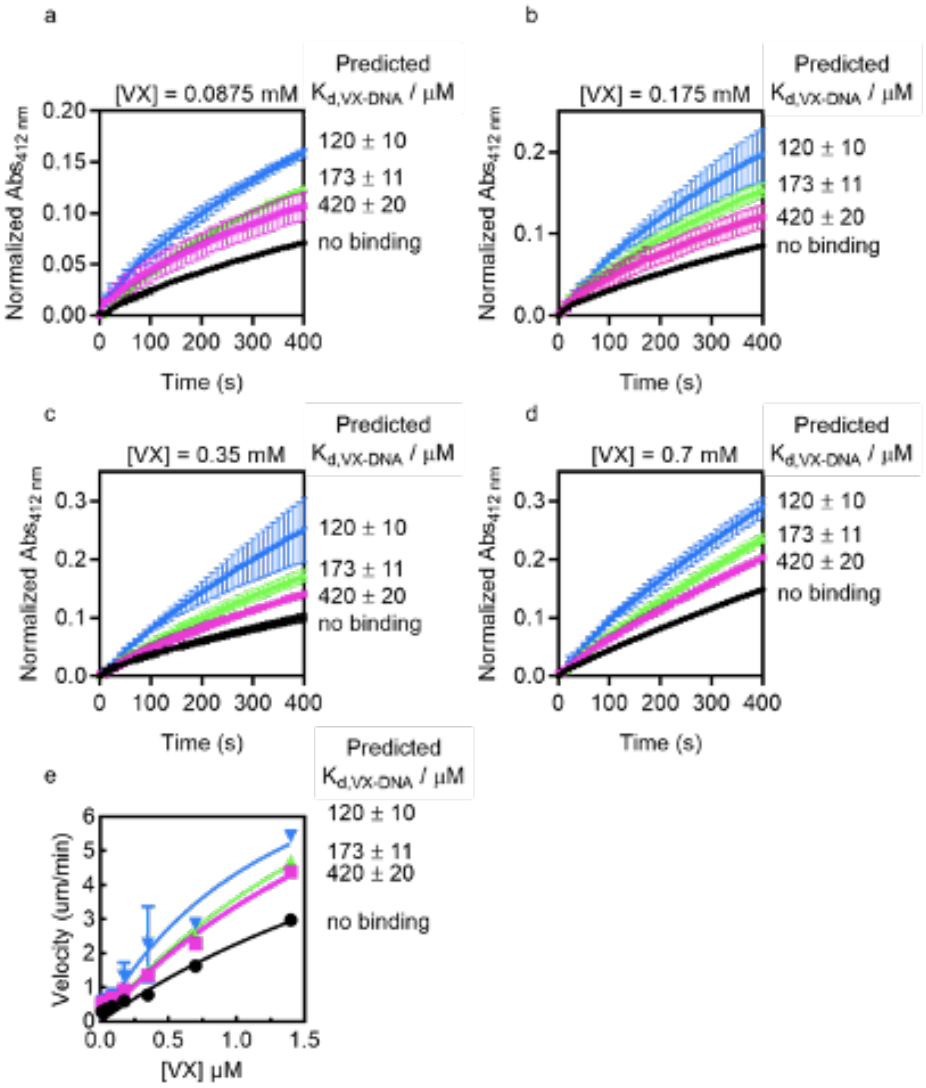

Figure S 2.3 VX hydrolysis with PTE-DNA variants. (a-d) The time course reaction of VX hydrolysis by PTE and PTE-DNA modified with different 20 bp double stranded DNA fragments (1-2 mg PTE/PTE-DNA with 0.0875, 0.175, 0.35, 0.7 mM and 1.4 mM of VX). The reaction was monitored by recording the absorbance at 412 nm of Ellman's reagent. (e) The kinetic analysis of the linear kinetic region of VX hydrolysis with PTE and PTE-DNA.

	Sequence (All from 5' to 3')	MW (g/mol)	Ext. Coefficient (L/(mole.cm))	K_d measured by MST (μM)
DNA5	CCTAAAAGAGCCTAAAAGAG	6412.5	203200	136±3
	CTCTTTTAGGCTCTTTTAGG	6146.1	204000	
DNA4	GAATCTTCGGGAATCTTCGG	6412.5	205100	287±14
	CCGAAGATTCCCGAAGATTC	6146.1	199100	
DNA3	CAGGTTGCAGCAGGTTGCAG	6526.5	193300	59±6
	CTGCAACCTGCTGCAACCTG	6038	175700	
DNA6	CAGGTTGCAGCAGGTTGCAG	6526.5	193300	3.3±0.3
	CGCAGACATCCTGCCGTAGCCTGAGGCACACG	9780.4	298400	
	GCATTGGTCGGACTGAACAGGACTACGCTGGC	9890.4	305400	
	CGTGTGCCTACCCGACCAATGC	6656.4	197900	
	GCCAGCGTAGTGGATGTCTGCG	6807.4	208800	
	TCAGTGGCTACGGCACCTGT	6109	183100	
DNA7	CAGGTTGCAGCAGGTTGCAG	6526.5	193300	1.4±0.8
	CAAGTGGTTCTGCCGTAGCCTGAGGCACACG	9841.4	300000	
	CGTGTGCCTCACCGACCAATGC	6656.4	197900	
	GCATTGGGTCGGACTGAACAGGACTACGCTGGC	9890.4	305400	
	GCCAGCGTAGTGAACACACTTG	6744.4	213400	
	TCAGTGGCTACGGCACCTGT	6109	183100	

Figure S 2.4 Summary of DNA sequences and the measured K_d between DNA scaffolds (DNA 3, DNA4, DNA5, DNA6 and DNA7) and paraoxon. DNA1 to DNA 5 are double strand DNA. DNA6 and DNA7 are DNA DX tiles made from the listed oligos.

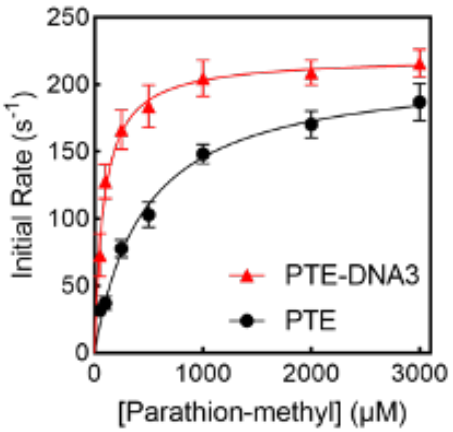

	PTE	PTE-DNA3
K_M (μM)	456.9 ± 61.7	84.9 ± 12.2
k_{cat} (s^{-1})	212.2 ± 8.9	220.3 ± 6.3

Figure S 2.5 PTE-DNA hydrolysis of parathion-methyl. The kinetic assay of PTE (●) and PTE-DNA3 (▲) reacting with parathion-methyl. Data are mean ± standard derivation.

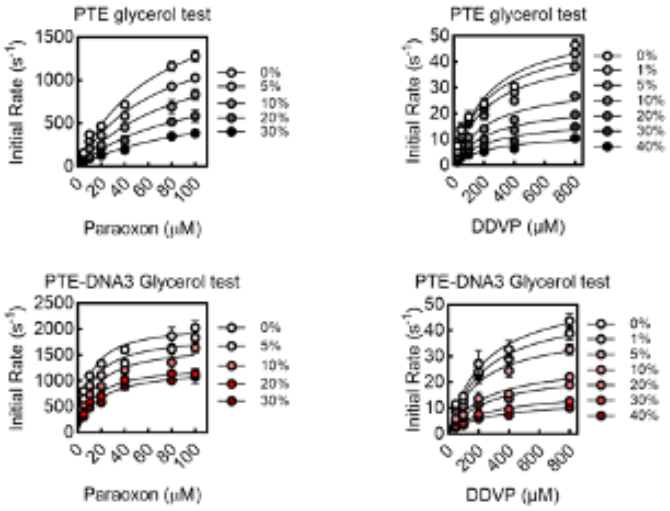

Glycerol %	Kinetics	Paraoxon		DDVP	
		PTE	PTE-DNA3	PTE	PTE-DNA3
0%	k_{cat} (s^{-1})	2143 ± 231.5	2102 ± 86	56.1 ± 7.8	55.2 ± 4.2
	K_M (μM)	69.0 ± 14.7	9.6 ± 1.6	237.4 ± 83.1	239.6 ± 44.2
1%	k_{cat} (s^{-1})			50.7 ± 10.6	49.4 ±8.3
	K_M (μM)			218.9 ± 120.5	238.6 ± 102.4
5%	k_{cat} (s^{-1})	1733 ± 139	1894 ± 89	45.2 ± 8.8	40.3 ± 6.7
	K_M (μM)	70.3 ± 10.9	11.9 ± 2.1	224.0 ± 113.4	206.8 ± 90.9
10%	k_{cat} (s^{-1})	1546 ± 195	1712 ± 110.5	32.0 ± 6.2	27.5 ± 5.1
	K_M (μM)	91.2 ± 17	14.5 ± 3.3	230.8 ± 114.9	239.7 ± 112.4
20%	k_{cat} (s^{-1})	1125 ± 263.2	1309 ± 69	24.0 ± 4.1	24.2 ± 4.2
	K_M (μM)	94.3 ± 18.8	13.5 ± 2.6	237.2 ± 104	251.6 ± 109.1
30%	k_{cat} (s^{-1})	780 ± 102.8	1251 ± 81	17.7 ± 4.0	16.3 ± 2.5
	K_M (μM)	102.3 ± 22.9	17.5 ± 3.7	237.6 ± 136.7	255 ± 98.1
40%	k_{cat} (s^{-1})			12.6 ± 3.1	13.0 ± 1.9
	K_M (μM)			249.7 ± 155.9	257.6 ± 94.4

Figure S 2.6 The kinetic assay of PTE and PTE-DNA1(red) reacting with paraoxon and 2,2-dichlorovinyl dimethyl phosphate (DDVP) in 0%,1%, 5%, 10%, 20%, 30%, 40% (v/v) respectively. Data are mean ± standard derivation.

MQTRRVVLKSAAAAGTLLGG LAGCASVAGSIGTGDRINTV RGPITISEAGFTLTHEHICG ***1-60***
SSAGFLRAWPEFFGSRKALA EKAVRGLRRARAAGVRTIVD VSTFDIGRDVSLLAEVSRAA ***61-120***
DVHIVAATGLWFDPPLSMRL RSVEELTQFFLREIQYGIED TGIRAGIIKVATTGKATPFQ ***121-180***
ELVLRAAARASLATGVPVTT HTAASQRDGEQQAAIFESEG LSPSRVCIGHSDDTGDLSYL ***181-240***
TALAARGYLIGLDHIPHSAI GLEDNASASALLGIRSWQTR ALLIKALIDQGYMKQILVSN ***241-300***
DWLFGFSSYVTNIMDVMDSV NPDGMAFIPLRVIPFLREKG VPQETLAGITVTNPARFLSP ***301-360***
TLRAS ***361-365***

PTE	
PTE M1	S319R
PTE M2	S319R, R185K
PTE M3	R185K
PTE M4	D208G

	PTE	PTE M1	PTE M3	PTE M4	PTE M2
$k_{cat,app}$ (s^{-1})	2087 ± 119	1004 ± 35	85 ± 3	347 ± 6	1325 ± 75
K_M (μM)	65 ± 7	26 ± 3	27 ± 3	19 ± 1	88 ± 9

	PTE-DNA3	PTE M1-DNA3	PTE M3-DNA3	PTE M4-DNA3	PTE M2-DNA3
$k_{cat,app}$ (s^{-1})	2189 ± 110	1101 ± 26	101 ± 4	358 ± 11	1365 ± 58
K_M (μM)	11 ± 2	10 ± 1	24 ± 3	8 ± 1	20 ± 3

Figure S 2.7 Enzyme kinetics of PTE mutants. (top) PTE amino acid sequence and list of studied mutants. (bottom) Kinetic analysis of PTE variants. Data are mean ± standard derivation.

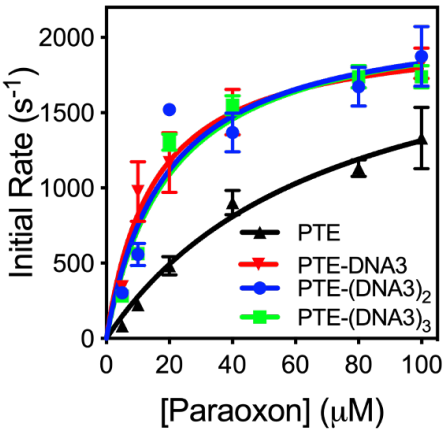

Figure S 2.8 Kinetic assay of paraoxon hydrolysis by PTE and PTE-DNA with different length DNA3.

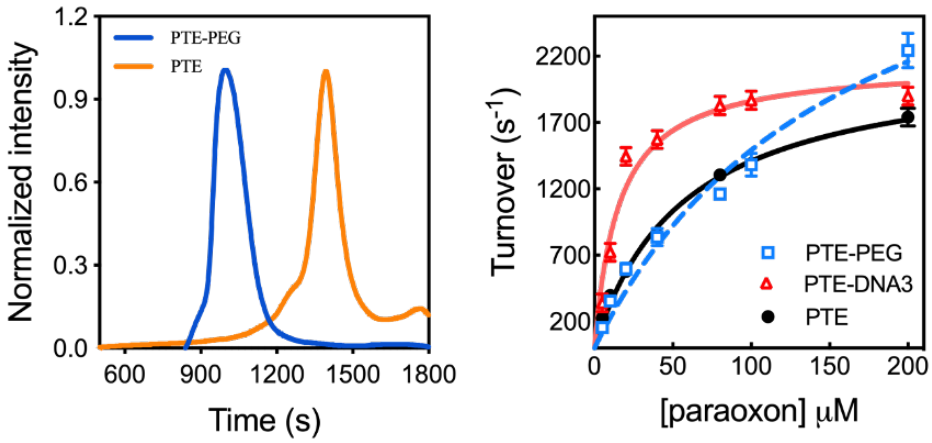

Figure S 2.9 Analysis of PTE-PEG. (a) Size exclusion chromatography of PTE and PTE-PEG conjugation. The sample elution time positively correlates with sample size. The peak of PTE conjugated with 10 kDa PEG is approximately 230 kDa, indicating the approximate size of the conjugate. Thus, the number of PEG is qualified based on the equation. From the calculation, PTE:PEG≈1:18 (b) The kinetic assay of paraoxon hydrolysis by PTE, PTE-DNA3 and PTE-PEG.

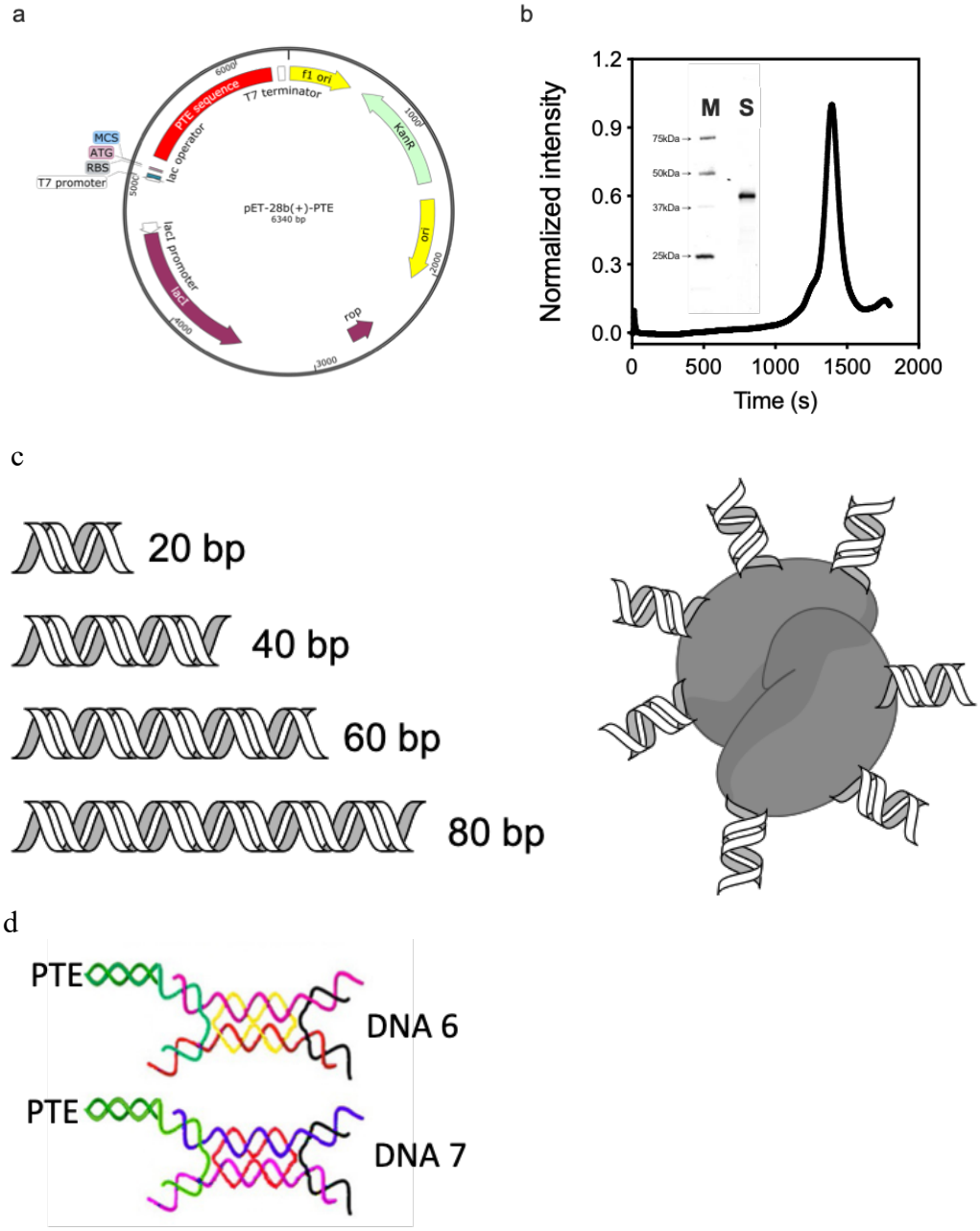

Figure S 2.10 PTE-DNA concept. (a) PTE expression plasmid map. The backbone is pET-28b(+). PTE expression is regulated by lacI promoter with IPTG. The selectable marker is kanamycin. (b) PTE SDS-PAGE result after size exclusion chromatography (inset; M indicates the protein marker and S indicates the soluble PTE fraction). (c) Schematic representation of the DNA scaffolds and PTE-DNA conjugates with DNA fragments (not to scale). (d) Schematic of DNA tile motifs with PTE conjugation site indicated.

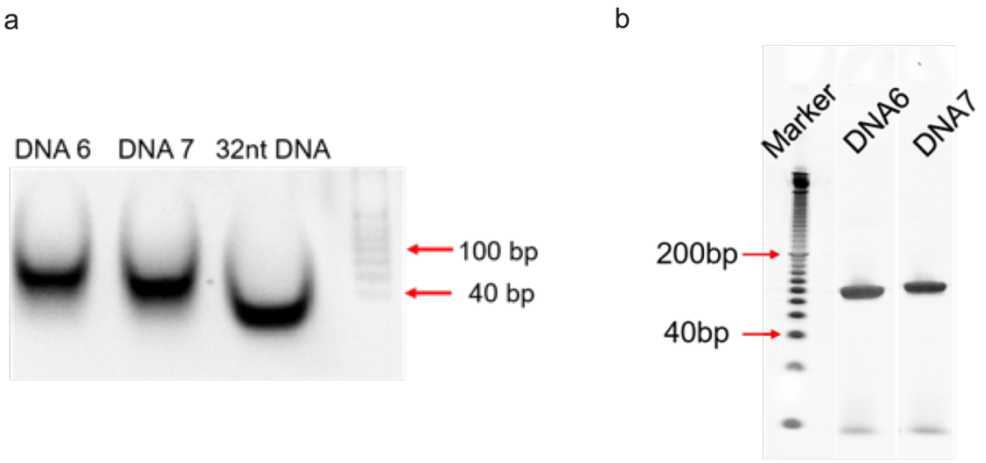

Figure S 2.11 Electrophoretic analysis of assembled DNA motifs. (a) Non-denaturing agarose gel with assembled DNA6, DNA7 (100 pmol each), and a single stranded 32nt DNA for comparison. The 32nt strand is typically used as one of the primers in DNA6 (CGCAGACATCCTGCCGTAGCCTGAGGCACACG). Electrophoresis was performed at room temperature under a constant 80 volts for 20 min. (b) Non-denaturing PAGE with assembled DX motifs DNA6 and 7 (left lane: 20bp DNA ladder; middle lane, 2 pmol of DNA6; right lane, 2 pmol of DNA7). Electrophoresis performed at 4 ºC under constant 120 volts for 45 min. The bands were visualized by using Ethidium bromide.

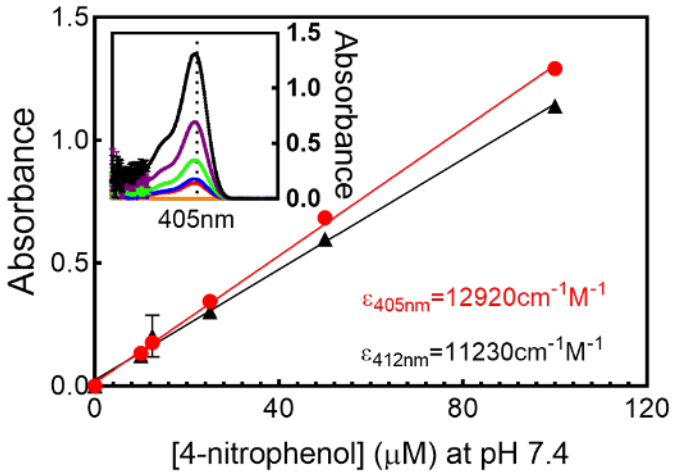

Figure S 2.12 4-nitrophenol extinction coefficient at wavelength 405 nm and 412 nm in pH 7.4 1×PBS buffer at room temperature.

Chapter 3. Multiscale simulation-guided design of enzyme bioconjugates with enhanced catalysis[2]

3.1 Abstract

Nano-scaffolds chemical conjugation to an enzyme is a widely used strategy to enhance enzyme activity. A fundamental understanding of the impact of scaffold location on the desired enzyme property is a critical problem in designing such systems. We developed and validated a prediction model for the impacts of DNA scaffold location on the improvement of phosphotriesterase (PTE) activity using a combined computational and experimental method. PTE modified with a 20 bp double-stranded DNA scaffold that micromolar-level binds to its substrate, paraoxon, improves the effective substrate concentration, lowering the Michaels constant and increasing the second-order rate constant, k_{cat}/K_M. The model requires (i) the effective substrate concentration calculated by a multiscale modeling technique integrating molecular dynamics and Brownian dynamics simulations, and (ii) the physical geometry of the enzyme, conjugated DNA scaffold, and the attachment site. The predicted K_M enhancements when the DNA scaffold is conjugated with site-specific click chemistry to one of seven different positions on the enzyme (ranging from 1.0 to 7.3 nm between the conjugation site and the catalytic center) match the enhancements observed in PTE-DNA. The study also revealed the greatest kinetics

[2] This chapter is under review for publication with the title, "Multiscale simulation-guided design of enzyme bioconjugates with enhanced catalysis". This paper is co-authored by Xiao Hong and Tim Cholko (co-first authors) along with Drs. Chia-en Chang and Ian Wheeldon (co-corresponding authors). Xiao Hong was responsible for the experiment. Tim Cholko conducted the molecular simulations, and the two co-first authors worked on the modeling aspects of the paper together.

enhancement (a >7-fold drop in K_M and a corresponding rise in k_{cat}/K_M) achieved when the DNA scaffold is connected near to, but not blocking, the enzyme's active site. While proven using the hydrolysis of organophosphates with PTE, this work is generally applicable to different enzymes, and molecular scaffolds used to raise effective substrate concentration and boost enzyme kinetics by controlling the enzyme microenvironment.

3.2 Significance statement

Nanotechnology has shifted the immobilization of enzymes from the fixed surface to the enzyme itself. Here, we show that the structural rearrangement induced by enzyme immobilization leads to changes in the enzyme's surroundings and, consequently, the kinetics. Therefore, it is crucial to understand how immobilization changes the local substrate environment. We use multi-scale modeling and experiments to understand when and how the local environment of enzymes changes kinetics. We show that changes in the enzyme's surroundings yield dramatic changes in kinetics, and therefore the location of enzyme modification should be given as much attention in enzyme engineering as how the enzyme is modified.

3.3 Introduction

A successful strategy to enhance enzyme catalysis is conjugation to a biological or synthetic polymer. Typically, these approaches work to maintain a microenvironment around the enzyme that is favorable to activity and stabilizes an active enzyme structure, thus enabling catalysis at elevated temperatures, in extreme pH, or in non-aqueous solvents

[1–4]. Controlling an enzyme's microenvironment can also enhance reaction kinetics [5–7]. For example, polymers and other modifications that create a charged environment around or near the active site of an enzyme can be used to control substrate specificity through charge-complementarity, attracting substrates with opposite charge and repelling like-charged substrates [8,9]. PEGylation, one of the most common enzyme modifications, is often used to increase *in vivo* circulation times for therapeutic proteins and enzymes by protecting against protease degradation, but increased catalytic turnover has also been observed [10,11], an effect likely due to the creation of a microenvironment favorable to reaction kinetics. Similarly, encapsulation in DNA nanostructures or other charged polymers can enhance enzyme turnover by providing a microenvironment that maintains an optimal pH or solvent conditions favorable to catalysis [12].

In a similar approach, we have pursued conjugation strategies to enhance enzyme catalysis using sequence-defined DNA scaffolds to increase the effective substrate concentration around an enzyme. This strategy exploits weak substrate-scaffold binding interactions that create a local environment with a higher substrate concentration than the bulk solution. The result is higher reaction rates than would be achieved if the enzyme was exposed to the lower bulk substrate concentration, an effect that is observable by a decrease in the apparent Michaelis constant ($K_{M,app}$) and a corresponding increase in the second order rate constant (k_{cat}/K_M)of the enzyme-DNA conjugate [13–15]. This strategy of controlling an enzyme's effective substrate concentration is also found in nature, where tethered kinase substrates increase phosphorylation rates and substrate selectivity [16–18]. Synthetic mimics of this strategy that tether redox cofactors in close proximity to their enzyme have also

been successful in increasing the turnover of NAD^+-dependent oxidoreductases. Collectively, these and other examples that provide a means of controlling the effective concentration of an enzyme's substrate [19,20], represent a new approach to engineering enhanced enzyme kinetics.

While engineering stability through conjugation is well understood, design rules explaining how to increase enzyme reaction kinetics above wild type levels using conjugation strategies are lacking. To better understand the molecular mechanisms of these effects and advance conjugation approaches focused on enhanced kinetics, a more fundamental understanding of the relationships between the conjugate chemistry, structure, and enzyme kinetics is needed. Here, we address this lack of knowledge through a combined computational, experimental, and modeling approach, the output of which begins to set design rules on how to bring about an increase in effective substrate concentration in an enzyme-DNA conjugate system, and in doing so, links kinetic enhancements to enzyme-DNA features. We do this in the context of a phosphotriesterase-DNA conjugate system (PTE-DNA) that can catalyze the hydrolysis of organophosphates, including the chemical warfare agents VX and Sarin as well as the insecticide paraoxon, use of which is band in the US and other countries [21,22].

Experimental techniques alone often lack the resolution to accurately explain and predict the enhancements gained from conjugation. As such, we set out to combine computational modeling and simulation to study the PTE-DNA system in greater detail and quantify effects that are difficult to assess experimentally. Specifically, we use

multiscale modeling including atomistic molecular dynamics (MD) and rigid-body Brownian dynamics (BD) simulations to capture detailed intermolecular interactions and investigate the concentration gradient of organophosphates around the DNA scaffolds used to modify PTE. Thus, we attempt to quantify the potential increase in effective concentration gained by conjugation of substrate-binding scaffolds to an enzyme of interest. We support the computational studies by experimentally testing the positional effect of a single DNA scaffold on enzyme kinetics, and subsequently combine the simulation and experimental data to develop a mechanistic model of the effects of the DNA scaffolds and the position of the conjugation on catalysis. Our results show that our DNA scaffold modifications to PTE decrease K_M through a combination of increased effective substrate concentration around the DNA and by expanding the region of enhanced effective concentration to include the enzyme's active site, that is, by enlarging the substrate capture radius of the conjugated complex.

3.4 Results and Discussion

We previously developed an enzyme-DNA conjugation strategy that exploits weak interactions between a DNA scaffold and the enzyme's substrate to enhance catalysis by decreasing the apparent Michaelis constant, K_{M}. When appropriately designed, catalytic turnover, k_{cat}, is not affected and the second order rate constant, k_{cat}/K_M is increased via the reduction of K_M. The central hypothesis is that the conjugated DNA acts as a substrate-binding scaffold, transiently tethering the substrate to the enzyme and increasing the effective concentration. When applied to PTE and the hydrolysis of organophosphates, we

observed an ~11-fold decrease in K_M; PTE monomer was modified with ~7 DNA scaffolds distributed across the surface and with a nucleic acid sequence known to bind the organophosphate paraoxon with a K_d of ~1.4 μM [13]. We have also produced similar results with the model enzyme HRP and an aldo-keto reductase by conjugating 20 bp DNA scaffolds with μM substrate binding to a series of different HRP substrates and to an NAD^+ cofactor mimic [14,15]. In each of these cases, modeling and experiments show that substrate binding occurs in the major and minor groove of the double stranded DNA and via intercalation between base pairs, and that binding to a given substrate is DNA sequence-dependent [23]. Here, we take a computational approach to quantify the increase in effective concentration that is possible with DNA scaffolds. Our approach begins with MD- and BD-analysis of the concentration gradient of organophosphate substrates around a double stranded DNA scaffold. The substrates include paraoxon, which exhibits low μM binding to DNA, the other is DDVP, which does not bind specifically to DNA (predicted K_d of ~1 mM) [13]

3.4.1 Multiscale simulations predict an increase in effective substrate concentration

We utilized a multiscale modeling that captures both molecular interactions in atomistic details and large-scale substrate concentration gradients. As shown in Figure 3.2a, our simulations began by first defining 5Å-wide regions around a DNA fragment. These shells were used to quantify the substrate concentration in each volume at the end of the simulations. Classical MD simulations were used to model substrate-DNA interaction within a 10 Å thick cylindrical shell (the first 2 shells). The detailed intermolecular

interactions, including solutes, waters, and ions, can be modeled explicitly and therefore accurately quantify local substrate concentration while the substrate is close to the enzyme. Notably, substrates sometimes can bind on the DNA grooves and become unavailable for catalysis. Therefore, these bound substrates were not included for estimating the effective concentration. Once the substrates cannot form close contacts with the DNA, the computationally more efficient BD simulations were used to model the concentration of substrates in all other shells.[24] Because a 12 Å cutoff was applied to compute vdW interactions, the BD runs that modeled substrate motions beyond the first 2 shells did not include vdW forces to speedup calculations. We omitted the PTE enzyme for creating a more generalized model and for computational efficiency as well. The highly negatively charged DNA, (-40 e^- overall) compared to PTE (+1 e^-) at physiological conditions, is significantly more important to provide long-ranged electrostatic steering attractions to the substrates. [25] Therefore, the omission of PTE should not introduce any sizable artifacts. The BD simulations were carried out at 60 μM to match our experiments. However, using the experimental concentration in MD would result in an unrealistically large size of the water box; therefore, we used a 16 mM substrate concentration, 64 substrates in total within a tractable water box, for the MD simulations. We ran two replicates of each simulation to ensure consistency, but present data from only one set of simulations in the main text. Both data sets are available in the supporting information (Figure S3.1).

The resulting substrate distributions show a smooth upward trend in all shells, and this effect is stronger for paraoxon than for DDVP, in agreement with experimental measurements13. We quantified the effects by use of the simulated gradient of normalized

substrate concentration, [S]/[S]0, as a function of distance from the DNA (Figure 3.2b). Both paraoxon and DDVP show increased effective concentration when the substrates are close to DNA. In the first shell modeled by MD, where both electrostatic and vdW forces were present, paraoxon concentration was higher than that of DDVP and $[S]/[S]_0$ was equal to 3.6 for paraoxon and 1.0 for DDVP. In more distant shells modeled by BD, both substrates maintained effective concentrations above the bulk (*i.e.*, $[S]/[S]_0$ values greater than 1) that gradually decreased with increasing distance. The marginally higher effective paraoxon concentration in the 3rd and 4th shells suggested a slightly stronger long-ranged electrostatic attraction between DNA and a more polar molecule paraoxon, compared with the attractions between DNA and DDVP. Note that substrate molecules bound to the DNA were not included in the calculations, as such molecules are not accessible to the enzyme and consequently are not an accurate reflection of the effective concentration. Simulation results including the bound molecules are presented in Figure S3.1 and show an exaggerated increase in concentration within the first shell. Notably, BD simulations did not utilize a fixed number of substrate molecules, which avoids artificial substrate depletion observed in MD (with 64 substrates) due to substrate-DNA binding (Figure S3.1). We proceed to model the overall effect on K_M in later sections using the effective concentration shown in Figure 3.2b.

3.4.2 Transient binding, effective concentration, and substrate catalytic accessibility

The effective substrate concentration produced by the conjugated DNA should reflect the increased number of substrate molecules available for catalysis. Therefore, we calculated the average residence time of the two different substrates on the DNA molecule from the MD trajectories to ensure that substrate is in a close proximity of the biomolecule for the chemical reaction. The residence time is the amount of time for which one substrate molecule was within 4.5 Å from the DNA. Average residence times for paraoxon and DDVP were 208 ps and 86 ps, respectively. The number of distinct substrate-DNA contacts for each substrate was similar, meaning a roughly equal number of DDVP and paraoxon molecules encountered the DNA, but paraoxon stayed close to DNA for 2.4 times longer.

In addition to the residence time calculations, we also explored the binding modes of each substrate to gain mechanistic insights into intermolecular attractions. We observed that paraoxon bound in the DNA minor groove as well as to the terminal DNA bases through pi-stacking interactions, and at least one paraoxon molecule bound to the major groove before intercalating between two base pairs (Figures S2a and S2b). The intercalated molecule formed a stable interaction that lasted ~70 ns, the longest interaction observed in any of our simulations. DDVP interactions with DNA were shorter-lived and electrostatic in nature, primarily taking place near the highly polar backbone and at the ends of the DNA strand (Figure S3.2c). Overall, the average residence times of both substrates were tens to hundreds of picoseconds, much shorter than the catalytic rate of PTE, which is on the order

of 2000 s^{-1} (see refs. [13,26]). Taken together, these simulations are highly supportive of our central concept, the effective concentration, of the PTE-DNA system. That the rationally-designed DNA sequence with micromolar strength binding to a substrate of interest can increase the effective concentration near the conjugated scaffold, and importantly increase the available substrate molecules for catalysis.

3.4.3 Azido side chain amino acid incorporation enables site specific bioconjugation of DNA scaffolds

Given that our simulations predicted that the local concentration of paraoxon is significantly increased within 1-2 nm from the DNA scaffold, we sought to test the positional effect of the scaffold on catalysis and determine the distance from the active site when catalysis can be enhanced. To do so, we used non-canonical amino acid technology to create a series of PTE mutants that enabled the bioconjugation of a DNA fragment at defined distances from the active site, where a 20 bp DNA scaffold is conjugated to PTE at position K175 via click chemistry [27]; DNA modified with dibenzocyclooctyl (DBCO) was reacted with the azido side chain of p-azido-phenylalanine (pAzf). Figure S3.3a shows the successful incorporation of the pAzf amino acid at positions K175, F149, A78, K294, and A364, positions selected because they differ in distance to the active site and incorporation of pAzf did not disrupt enzyme activity. In addition, positions D133, D160, and T352 were also modified to create a series of eight unique PTE-DNA constructs each with a different distance between the attached DNA to the active site. The mutant positions and distance from DNA to active site, measured based on the 1HZY structure of PTE, are

D133 (0.6 nm), K175 (1 nm), F149 (1.6 nm), A78 (3.6 nm), D160 (4 nm), T352 (5.3 nm), K294 (7 nm), and A363 (7.3 nm). Confirmation that a single DNA scaffold was attached to a PTE mutant is shown in Figure S3.3b. A 260 nm spectral peak proportional to the amount of attached DNA is observed with conjugation to PTE (see Supporting Information (SI): Experimental Methods), and analysis of PTE-DNA K175pAzF revealed that on average 1.1±0.1 DNA fragments where attached to each PTE monomer using the click chemistry approach (note, PTE is a functional dimer). In comparison, when DNA is conjugated to PTE at every accessible lysine side chain via bifunctional sulfo-NHS-ester/maleimide chemistry to thiolated DNA fragments, 7.2±0.7 scaffolds were attached per monomer. This construct, PTE-DNA_7, includes DNA scaffolds that are conjugated to PTE at distances that overlaps with the range of the distances of the singly modified constructs, including positions K175 (1 nm), K185 (1.6 nm), K82 (3.2 nm), K77 (3.6 nm), K285 (6.5 nm), K295 (7 nm), and K339 (7.2 nm) of each PTE monomer.

3.4.4 The Michaelis constant, K_M, decreases as the distance between scaffold and active site decreases

With the series of PTE-DNA constructs in hand, we set out to characterize the effect of DNA position on enzyme kinetics. Figure 3.3 presents both the kinetic analysis of each mutant as well as an image of the crystal structure of PTE with the position of the active site and incorporated pAzf amino acid indicated; the kinetic analyses and images are arranged according to the distance between conjugated DNA and the active site increasing in distance from the top left to the bottom right, with the PTE-DNA_7 control construct as

the last entry of the figure. Indicated on each image is the shortest surface distance between the conjugation site and the zinc molecule of the catalytic active site (see Figure S3.4 for additional details). PTE-DNA$_7$ is notable because the turnover rate (k_{cat}) is unchanged in comparison to unmodified PTE (Table 1). Similarly, the k_{cat} values of the PTE-DNA constructs are relatively unchanged in comparison to unmodified PTE; only mutations to positions 133, 160, and 352 resulted in a significant decrease in k_{cat}. In the case of position 133, turnover with and without attached DNA was substantially reduced in comparison to PTE, likely because the active site was altered with the incorporation of pAzf. Incorporation at positions 160 and 352 also decreased k_{cat}, but in these cases the reduction was limited to ~10% or less. Given this, we focused on the effect of DNA position on K_M using the series of mutants that established a distance range between the DNA scaffold attachment site and the enzyme's active site of 1.0 to 7.3 nm. The kinetic effect of DNA conjugation position can be visually seen in the series of kinetic curves for the PTE-DNA complexes (Figure 3.3). When the DNA is attached far from the active site (*i.e.*, A364pAzf; 7.3 nm) the kinetic curves and parameters (k_{cat} and K_M) of the modified and unmodified PTE mutants are identical. As the distance between the DNA scaffold and the active site is decreased, the PTE-DNA kinetic curve shifts leftward, rates at lower substrate concentrations are increased, and the K_M parameter is reduced. At 1.0 nm distance (attachment at position 175), K_M is reduced by 7.1-fold, an enhancement that is well-matched with that achieved with PTE-DNA$_7$, which contains a scaffold at the same position. At longer distances, a reduction in K_M was also maintained: at 1.6 nm (position 149), the DNA scaffold reduced K_M by 4.4-fold, at distances between 3.6 and 5.3 nm (positions 78,

160, and 352) the enhancement ranged between 2.1- and 2.2-fold, and finally at 7.0 nm (position 294) the enhancement was less than 30% reduction of K_M.

To verify that the enhancements in K_M were a result of the paraoxon-DNA interactions and the predicted increase in effective concentration that result from these interactions, we repeated the kinetic analysis with the non-binding control substrate DDVP (Figure S3.5 and Table S1). Mutation to D133, the closest conjugation site at 0.6 nm distance, was again detrimental on kinetics, but the effect with DDVP as a substrate was more pronounced in K_M, which increased 5-fold in the presence of a DNA scaffold. Attachment to the K175pAzF mutant, which is 1 nm from the active site and enhanced paraoxon binding by 7.1-fold, did not have an effect on the hydrolysis of DDVP, likely due to the lack of DDVP-DNA interactions and absence of an increased effective substrate concentration. As expected, conjugation to position 364 showed no significant changes in reaction kinetics with DDVP or with paraoxon, as the conjugation position is too far from the active site to affect the local substrate concentration. Additional evidence for the increased effective concentration effect on PTE kinetics was acquired through a series of activity assays with increasing viscosity. When enzyme activity is wholly or partially diffusion limited, such assays can be used to determine the substrate on-rate, k_1 [13,15,28]. This analysis revealed that decreases in K_M due to the attachment of a DNA scaffold were accompanied by an increase in paraoxon on-rate, and that in the absence of a change in K_M, DDVP and paraoxon on-rates were unchanged in comparison to unmodified PTE.

3.4.5 Modeling the substrate capture radius enables prediction of K_M enhancements

To help render our kinetic analyses into a more fundamental understanding of how the position of a conjugated scaffold can affect enzyme catalysis, we set out to develop a biophysical model to predict the fold enhancement of K_M achieved for any conjugation site. The model begins with a definition of K_M, where K_M is inversely proportional to the enzyme-substrate association rate, k_{on}, and can be expressed as

$$K_M = \frac{k_{\text{off}} + k_{\text{cat}}}{k_{\text{on}}} \tag{1}$$

where k_{cat} is the catalytic turnover rate and k_{off} is the rate of dissociation of substrate from the enzyme [33]. Since turnover is largely unaffected by conjugation of the DNA scaffold (see Table 1), we make the assumption that k_{off} is also unchanged. Given this, changes in K_M are dependent on k_{on} (or k_1 as presented in Figure S3.5), and a model that captures changes to the on-rate should enable the prediction of K_M after conjugation ($K_{M,app}$).

The multiscale simulations Figure 3.2 and kinetic analysis of PTE-DNA constructs with various conjugation sites suggest a direct proportionality between the effective substrate concentration, $[S]/[S]_0$, and the enhancement in K_M. Such a relationship is also observed when enzymes are immobilized on a charged support that creates a substrate concentration gradient from the bulk to the surface [29], where,

$$\frac{K_{\mathrm{M}}}{K_{\mathrm{M,app}}} = \frac{[S]}{[S]_o} \tag{2}$$

While this intuitive relationship is observed with our simulation data, it is not the only factor contributing to the enhancement in K_M. The size of the attached DNA scaffold is also likely to contribute to the effect as it can act as an extension of the enzyme, increasing the substrate capture radius of the PTE-DNA complex relative to unmodified PTE. The standard kinetic theory for collisions per unit time, α, between to molecules experiencing attractive intermolecular forces is

$$\alpha = \frac{4\pi CD}{\int_{r_o}^{\infty} \frac{1}{r^2} e^{\frac{-U(r)}{kT}}} = 4\pi CDr^* \tag{3}$$

The collision rate depends on C, the substrate concentration; D, the relative diffusion coefficient of the molecules; and the length r, the sum of the radii of the reactive portions of the two molecules. The radius r* is the larger effective radius after accounting for intermolecular attraction [30,31]. Here, we model the effect of DNA conjugation as an increase in r* since the DNA strand acts as a lure for substrate both energetically and sterically. The energetic contribution to the molecular collision rate is already accounted for in the substrate distribution quantified by the simulations; that is, it can be thought of as an increase in C in equation (3). Next, we can relate the ratio of the capture radius of the DNA-modified enzyme to that of the unmodified enzyme as

$$\frac{r_{\text{AS+DNA}}}{r_{\text{AS}}} \tag{4}$$

where r_{AS} depends on the size of the active site and r_{AS+DNA} depends on the size of the active site plus the size of the DNA fragment. Since both the active site and DNA can be approximated as ellipsoids, equation (5) can be used to estimate the effective radii

$$r = \frac{a}{ln\frac{2a}{b}} \tag{5}$$

where a and b are the major and minor oval semiaxes [31]. However, simply accounting for the linear extension of the active site and DNA is not adequate. As the conjugation site becomes more distant from the active site, the angle between DNA and the active site grows, and the efficiency of substrate capture diminishes. Our study shows that this angle has great influence on the K_M enhancement, and it is the dominant term in our model. This "offset angle" (θ_{DNA}) is well-defined as the angle between a vector from the enzyme center to the active site catalytic residues and a vector from the enzyme center to the conjugation site (Figure S3.6). The overall effect of the conjugated DNA, γ, is then modeled as

$$\gamma = 1 + \beta\left[\frac{\pi - \theta_{\text{DNA}}}{\pi}\left(\frac{r_{\text{AS+DNA}}}{r_{\text{AS}}} - 1\right)\right] \tag{6}$$

In the parameter γ, the offset angle is allowed to cover the range of π radians, or 180 degrees. When θ_{DNA} is 0, the enlargement of the active site due to DNA conjugation

can be fully exploited. When θ_{DNA} is π radians, the effective extension from DNA conjugation is 0 since the DNA is too far from the active site to increase the flow of substrate there. The factor β is defined as the "blocking factor", and represents the spatial overlap of the conjugated DNA and active site. If the active site is completely unobstructed, β = 1. If it is 30% blocked, β = 1 - 0.3 = 0.7, and so on. Altogether, the fold decrease in K_M can then be predicted as

$$\frac{K_{\mathrm{M}}}{K_{\mathrm{M,app}}} = \frac{[S]}{[S]_{\mathrm{o}}}\gamma \tag{7}$$

As shown in Figure 3.4, the substrate-capture window model described by equations (6) and (7) is in good agreement with our experiments (see SI for example calculations). At positions far from the active site the offset angle is 180 degrees, γ is equal to 1, and the model predicts that K_M will remain unchanged with the conjugation of a DNA scaffold, a result in quantitative agreement with the kinetics analysis of PTE-DNA (A364pAzF) and qualitative agreement with PTE-DNA (K294pAzF). When the DNA scaffold is attached closer to the active site, for example at positions 175, 149, 78, 160, and 352, γ is greater than 1 and the predicted enhancement in K_M is in good agreement with the kinetic analysis. The exception is again position 133. Conjugation here yielded 4.4-fold decrease in K_M, significantly less than observed for position 175, which is only 0.4 nm farther away from the active site. We can account for this discrepancy through the blocking factor, β. Molecular modeling suggests that the motion of the attached scaffold blocks 5-40% of the active site entrance depending on the rotational state of the DNA (Figure S3.7).

A β value for the D133pAzF mutant with attached DNA of 0.31 brings the model and experiment into agreement. However, 0.31 implies about 69% reduction in active site accessibility, indicating the blocking effect predicted by the molecular modeling underestimated the effect. It is also possible that mutation to this position contributes to the decrease in kinetic enhancement.

Overall, these results show that the K_M enhancement is not entirely explained by local substrate concentration increase, and that structural features of the conjugated complex also play a role. Our capture radius model demonstrates this effect by taking account of three structural parameters. . The first is γ, which is a function of the size of the active site, size of the scaffold (in our case a 20 bp DNA fragment), and the attachment position, all of which can be determined given a crystal structure (or accurate homology model) of the enzyme, an approximation of the scaffold structure, and knowledge of the conjugation site. The second critical parameter is the effective substrate concentration ($[S]/[S]_o$), which is a function of the strength of the substrate-scaffold interactions. Here, we use a multiscale approach that is suitable for many other substrates and scaffolds. Alternatively, BD-based or other modeling approaches could potentially be used to generate a reasonable approximation of $[S]/[S]_o$ as a function of distance from the selected scaffold. Lastly, for conjugation sites close to the catalytic center, the blocking factor β is required. This parameter can be difficult to estimate because the dynamics of the conjugated scaffold are likely system- and conjugation-chemistry dependent. For example, given a sufficiently flexible chemical linker, DNA or other highly charged scaffold could adsorb to a positively charged enzyme surface, or various conjugation chemistries could

alter the conformation of key active site residues (as is likely with incorporation of pAzF to positions 133). However, these challenges are only present when conjugation occurs very close to the active site, modifications that also often result in detrimental changes in catalytic turnover as observed with mutation to the D133 site of PTE. Using the PTE-DNA systems as an example, we show how experimental analyses combined with simple computational techniques can help explain and predict catalytic enhancement in enzyme-scaffold conjugates.

3.5 Conclusion

Enzyme activity can be enhanced through a wide range of bioconjugation strategies that create enzyme-scaffold complexes with controlled microenvironments. In this work, we show that computationally-guided enzyme-scaffold design can result in predictable enhancements in an enzyme's Michaelis constant, K_M, and increase the second order rate constant k_{cat}/K_M. A rationally designed DNA covalently attached to the enzyme PTE attracts the desired substrate (paraoxon) increasing the effective substrate concentration around the enzyme, an effect that results in a substantial decrease in K_M, an increase in substrate on-rate, k_1, and maintains the high catalytic turnover of the unmodified enzyme. The multiscale simulations combining MD and BD simulations showed that the increase in substrate concentration in close proximity to the DNA scaffold is due to both electrostatic attraction and short-range vdW forces and allowed the concentration gradient around the scaffold to be quantified. Using site selective conjugation, we created a series of PTE-DNA complexes that differ in the distance between conjugated DNA scaffold and

the enzyme's active site (0.6 to 7.3 nm), and in doing so were able to experimentally determine the effect of scaffold position on enzyme kinetics. Based on the experimental and computational results, we develop a capture radius model that predicts K_M enhancements based on the position of the conjugated scaffold; conjugation in close proximity to the active site without sterically blocking access achieved the greatest enhancement in enzyme kinetics, a 7.1-fold decrease in K_M. The model, along with the experimental and computational results, represent a new design approach to enhancing enzyme catalysis through controlled microenvironments where conjugated scaffolds are used to increase the effective substrate concentration of an enzyme. While this work and the resulting design principles were developed using PTE modified with a DNA scaffold, we anticipate that this approach can be used to design other enzyme-scaffold bioconjugates with enhanced activity and kinetics.

3.6 Materials and Methods

See SI Appendix, Materials and Methods for detailed materials and methods that describe computational Methods including (1) molecular dynamics simulations; (2) Brownian dynamics simulations; (3) radial distribution of paraoxon and DDVP around DNA; (4) calculation of paraoxon and DDVP residence time on DNA, and experimental methods including (5) PTE cloning, expression and purification; (6) incorporation of, and click-chemistry with p-azido-phenylalanine (pAzF); (7) PTE-DNA conjugation by bifunctional sulfo-NHS-ester/maleimide chemistry; (8) UV-vis analysis of PTE:DNA complexes; (9) PTE and PTE-DNA kinetic analysis; (10) Electrophoretic analysis of

pAzF incorporation into PTE; (11) calculation of model parameters; and (12) example calculation of predicted K_M enhancement.

3.7 Acknowledgements and funding sources

This study was supported by Army Research Office MURI grant W911NF1410263, the US National Science Foundation grant MCB-1932984 and US National Institutes of Health grant GM-109045.

3.8 References

1. Yan, M., Ge, J., Liu, Z. & Ouyang, P. Encapsulation of single enzyme in nanogel with enhanced biocatalytic activity and stability. *J. Am. Chem. Soc.* **128**, 11008–11009 (2006).

2. Zhang, P. *et al.* Zwitterionic gel encapsulation promotes protein stability, enhances pharmacokinetics, and reduces immunogenicity. *Proc. Natl. Acad. Sci. U. S. A.* **112**, 12046–12051 (2015).

3. Zaks, A. & Klibanov, A. Enzymatic catalysis in organic media at 100 degrees C. *Science* vol. 224 1249–1251 (1984).

4. Chapman, R. & Stenzel, M. H. All Wrapped up: Stabilization of Enzymes within Single Enzyme Nanoparticles. *J. Am. Chem. Soc.* **141**, 2754–2769 (2019).

5. Zhang, Y., Ge, J. & Liu, Z. Enhanced Activity of Immobilized or Chemically Modified Enzymes. *ACS Catalysis* vol. 5 4503–4513 (2015).

6. Lancaster, L., Abdallah, W., Banta, S. & Wheeldon, I. Engineering enzyme microenvironments for enhanced biocatalysis. *Chem. Soc. Rev.* **47**, 5177–5186 (2018).

7. Huber, G. A. & McCammon, J. A. Brownian Dynamics Simulations of Biological Molecules. *Trends Chem* **1**, 727–738 (2019).

8. Azuma, Y., Bader, D. L. V. & Hilvert, D. Substrate Sorting by a Supercharged Nanoreactor. *J. Am. Chem. Soc.* **140**, 860–863 (2018).

9. Kraj, P., Selivanovitch, E., Lee, B. & Douglas, T. Polymer Coatings on Virus-like Particle Nanoreactors at Low Ionic Strength-Charge Reversal and Substrate Access. *Biomacromolecules* **22**, 2107–2118 (2021).

10. Daffu, G. K. *et al.* Sulfhydryl-specific PEGylation of phosphotriesterase cysteine mutants for organophosphate detoxification. *Protein Eng. Des. Sel.* **28**, 501–506 (2015).

11. Efremenko, E. N. *et al.* A simple and highly effective catalytic nanozyme scavenger for organophosphorus neurotoxins. *J. Control. Release* **247**, 175–181 (2017).

12. Zhang, Y., Wang, Q. & Hess, H. Increasing Enzyme Cascade Throughput by pH-Engineering the Microenvironment of Individual Enzymes. *ACS Catalysis* vol. 7 2047–2051 (2017).

13. Lang, X., Hong, X., Baker, C. A., Otto, T. C. & Wheeldon, I. Molecular binding scaffolds increase local substrate concentration enhancing the enzymatic hydrolysis of VX nerve agent. *Biotechnol. Bioeng.* **117**, 1970–1978 (2020).

14. Gao, Y. *et al.* Tuning Enzyme Kinetics through Designed Intermolecular Interactions Far from the Active Site. *ACS Catalysis* vol. 5 2149–2153 (2015).

15. Gao, Y., Roberts, C. C., Toop, A., Chang, C.-E. A. & Wheeldon, I. Mechanisms of Enhanced Catalysis in Enzyme-DNA Nanostructures Revealed through Molecular Simulations and Experimental Analysis. *Chembiochem* **17**, 1430–1436 (2016).

16. Dyla, M. & Kjaergaard, M. Intrinsically disordered linkers control tethered kinases via effective concentration. *Proc. Natl. Acad. Sci. U. S. A.* **117**, 21413–21419 (2020).

17. Siddiqui, J. K. *et al.* Myofilament Calcium Sensitivity: Consequences of the Effective Concentration of Troponin I. *Front. Physiol.* **0**, (2016).

18. Cool, A. M. & Lindert, S. Computational Methods Elucidate Consequences of Mutations and Post-translational Modifications on Troponin I Effective Concentration to Troponin C. *J. Phys. Chem. B* **125**, (2021).

19. Fu, J. *et al.* Multi-enzyme complexes on DNA scaffolds capable of substrate channelling with an artificial swinging arm. *Nat. Nanotechnol.* **9**, 531–536 (2014).

20. Ozbakir, H. F., Garcia, K. E. & Banta, S. Creation of a formate: malate oxidoreductase by fusion of dehydrogenase enzymes with PEGylated cofactor swing arms. *Protein Eng. Des. Sel.* **31**, 103–108 (2018).

21. Olsvik, P. A. & Søfteland, L. Mixture toxicity of chlorpyrifos-methyl, pirimiphos-methyl, and nonylphenol in Atlantic salmon () hepatocytes. *Toxicol Rep* **7**, 547–558 (2020).

22. Laetz, C. A., Baldwin, D. H., Hebert, V., Stark, J. D. & Scholz, N. L. Interactive neurobehavioral toxicity of diazinon, malathion, and ethoprop to juvenile coho salmon. *Environ. Sci. Technol.* **47**, 2925–2931 (2013).

23. Lang, X., Zhu, L., Gao, Y. & Wheeldon, I. Enhancing Enzyme Activity and Immobilization in Nanostructured Inorganic–Enzyme Complexes. *Langmuir* vol. 33 9073–9080 (2017).

24. Votapka, L. W. & Amaro, R. E. Multiscale Estimation of Binding Kinetics Using Brownian Dynamics, Molecular Dynamics and Milestoning. *PLoS Comput. Biol.* **11**, e1004381 (2015).

25. Breger, J. C. *et al.* Understanding How Nanoparticle Attachment Enhances Phosphotriesterase Kinetic Efficiency. *ACS Nano* **9**, 8491–8503 (2015).

26. Roodveldt, C. & Tawfik, D. S. Directed evolution of phosphotriesterase from Pseudomonas diminuta for heterologous expression in Escherichia coli results in stabilization of the metal-free state. *Protein Eng. Des. Sel.* **18**, 51–58 (2005).

27. Chin, J. W. *et al.* Addition of p-azido-L-phenylalanine to the genetic code of Escherichia coli. *J. Am. Chem. Soc.* **124**, 9026–9027 (2002).

28. Brouwer, A. C. & Kirsch, J. F. Investigation of diffusion-limited rates of chymotrypsin reactions by viscosity variation. *Biochemistry* **21**, 1302–1307 (1982).

29. Clark, D. S. & Blanch, H. W. *Biochemical Engineering*. (CRC Press, 1997).

30. Jackson, M. B. *Molecular and Cellular Biophysics*. (Cambridge University Press, 2010). doi:10.1017/cbo9780511754869.

31. Berg, O. G. & von Hippel, P. H. Diffusion-controlled macromolecular interactions. *Annu. Rev. Biophys. Biophys. Chem.* **14**, 131–160 (1985).

3.9 Figures and Tables

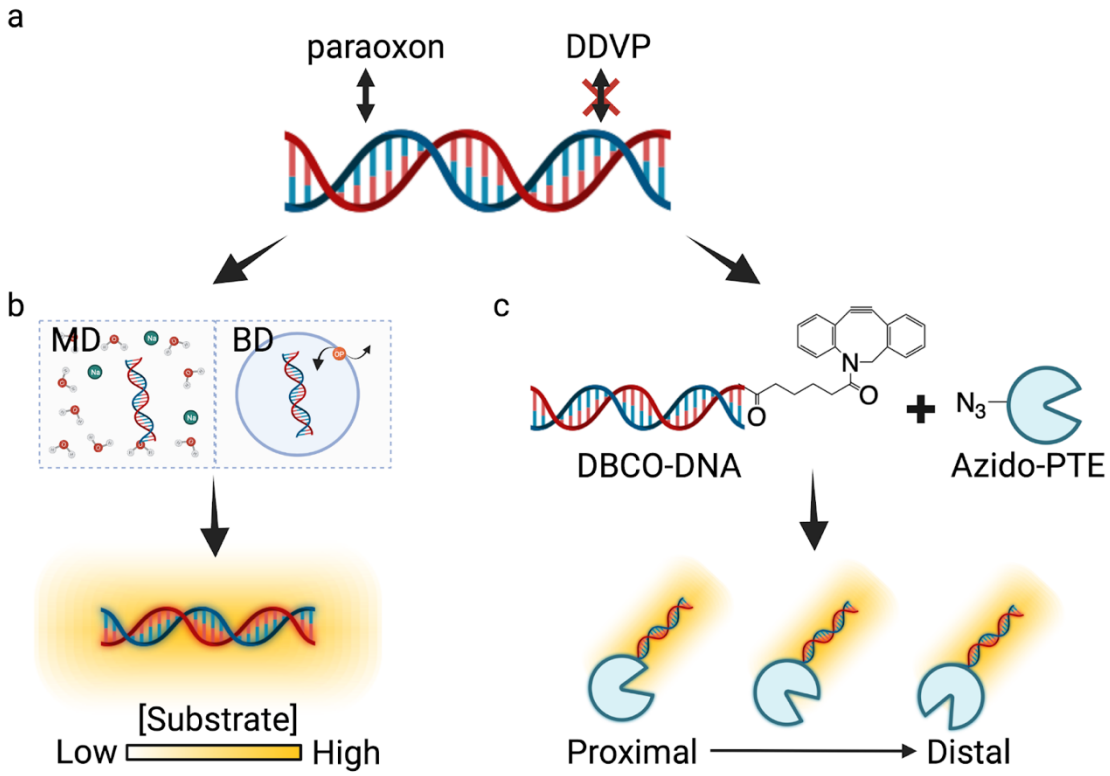

Figure 3.1 The concept map of the effective concentration around the DNA scaffold that controls the altered kinetics of the PTE at different DNA modified locations. (a) The rational designed DNA scaffold attracted paraoxon but did not interact with DDVP. (b) Multi-scale modeling calculated the effective substrate concentration around the DNA scaffold. (c) DBCO modified DNA scaffold site-clicked at the azido group (from proximal site to distal site) of PTE and changed the local substrate concentration around PTE's active site. Light blue Pacman indicates the PTE where the "mouse" represents as the active site.

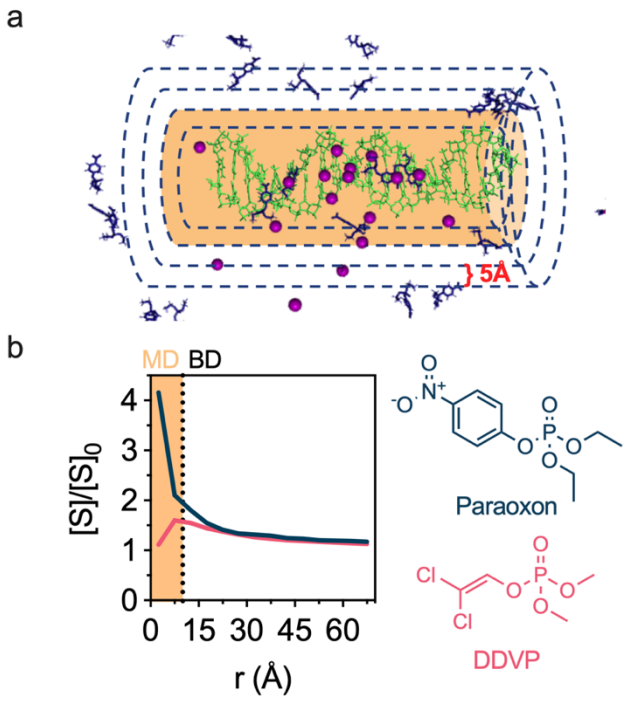

Figure 3.2 Multiscale modeling of the effective concentration around DNA scaffolds. (a) A screenshot of a molecular dynamics (MD, 0 to 10Å, stained by yellow) simulation featuring paraoxon (red) around a length of double-stranded DNA containing salt (purple). The effective substrate concentration in concentric shells enclosing the DNA (green) was calculated by averaging substrate concentrations in a 5 Å thick cylindrical shell across the simulation time. The shells extend outward from the DNA by around 100 Å; only the first four shells are depicted here for clarity. The concentration up to 10 Å from DNA (yellow shells) was quantified using MD simulations; the concentration beyond 10 Å was quantified using BD simulations. (**b**) Paraoxon and DDVP (structure shown as right) effective concentration curves after combining MD data from the first two shells (yellow) with BD data for all other shells.

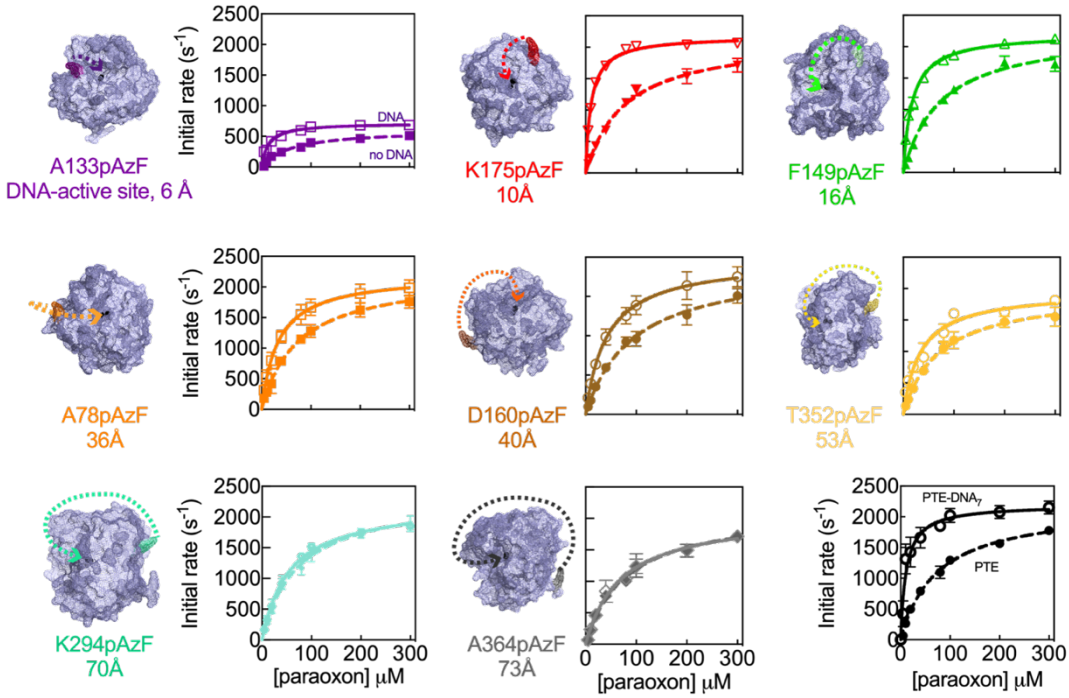

Figure 3.3 The effect of DNA position on PTE kinetics. Kinetic analysis and the crystal structure of PTE is shown for each PTE^{pAzF} mutant with (solid line) and without (dashed line) the conjugation of one or more DNA scaffolds. The image of each crystal structure has been modified to show the position of pAzF incorporation and the distance between the pAzF residue and the PTE active site. Approximate distances are stated for each mutant. DNA fragments are not shown for clarity. (Bottom, Right) PTE and PTE modified with ~7 DNA scaffolds per PTE monomer conjugated to free lysine groups by NHS-conjugation chemistry is shown as a comparison to the single DNA modifications achieved with the site-specific incorporation of pAzF.

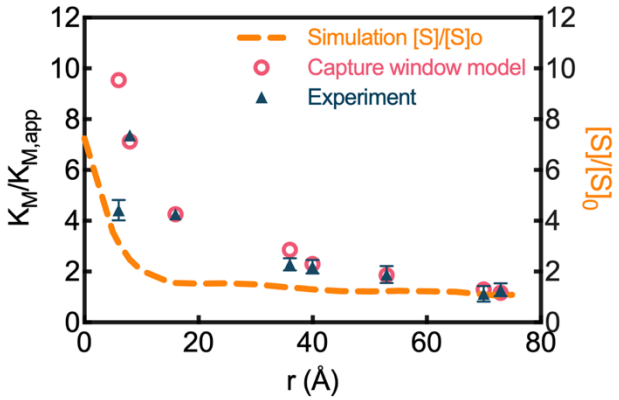

Figure 3.4 Mechanistic modeling captures the position-dependent kinetic enhancements of PTE-DNA conjugates. Left y-axis: Experimental and model predicted enhancement of K_M for paraoxon hydrolysis by DNA modified PTE. Right y-axis: Effective substrate concentration, $[S]/[S]_0$, predicted by multiscale simulations.

Table 3.1 Kinetic parameters of PTE-DNA and PTE mutants. Statistical significance in comparison to PTE in the absence of DNA conjugation is stated with "ns" indicating a p value > 0.05, * is $p<0.05$. The ± sign is a standard deviation (SD).

PTE Mutants	Distance (Å)	PTE				PTE-DNA$_1$			
		k_{cat} (s^{-1})		K_M (μM)		k_{cat} (s^{-1})		$K_{M,app}$ (μM)	
D133pAzF	6	612±39	*	61±10	ns	730±38	*	14±3.1	*
K175pAzF	10	2175±120	ns	78±12	ns	2180±35	ns	11±0.87	*
F149pAzF	16	2030±120	ns	74±14	ns	2110±58	ns	17±2.4	*
A78pAzF	36	2210±143	ns	74±12	ns	2210±117	ns	34±5.8	*
D160pAzF	40	1990±143	*	93±16	*	1980±110	*	42±7.3	*
T352pAzF	53	1950±146	*	70±13	ns	1963±164	*	34±9.1	*
K294pAzF	70	2140±172	ns	71±14	ns	2240±113	ns	55±9.8	*
A364pAzF	73	2350±163	ns	78±15	ns	2070±151	ns	69±13	ns
PTE	-	2185±122		73±10		-		-	
PTE-DNA$_7$	-	-		-		2198±143		11±3.1	

3.10 Supporting Information

3.10.1 Materials and Methods

3.10.1.1. Computational Methods

Molecular dynamics simulations. Molecular dynamics (MD) simulations contained the DNA sequence surrounded by substrate molecules in a cuboid simulation box of explicit TIP3P water solvent (Figure 1a). Both substrates were simulated at concentrations of 16 mM, requiring 64 molecules in a simulation box of approximately 6.5 × 106 Å3. Systems were minimized using the conjugate gradient method in three steps: first water only, then solute only, and finally the entire system, for 40000, 10000, and 20000 steps, respectively. This was followed by two-stage equilibration, first for water only then for the entire system, for 20-50 ps at 50, 100, 150, 200, 250, 275 and 298 K before production MD runs. Paraoxon and DDVP molecules started their trajectories from the same positions to avoid biasing their relative distribution. Simulations were run for 100 ns in the isothermal-isobaric (NPT) ensemble with three-dimensional periodic boundary conditions and a 2-fs time step using the NAMD 2.12 simulation software[1]. The Amber force fields Parmbsc1 [2] and GAFF [3] were used to model the DNA and substrate, respectively. Parameters for both substrate molecules were assigned by Amber's antechamber program using the AM1-BCC semi-empirical charge method [4]. 40 Na+ ions were added to neutralize the overall system charge. Long-range electrostatics were calculated using the particle mesh Ewald method and a 12 Å cutoff was employed for non-bonded force calculations. The SHAKE algorithm was used to constrain all bonds

involving hydrogen and the Langevin thermostat was used to maintain constant temperature.

Brownian dynamics simulations. To study the interaction of paraoxon and DDVP with DNA at 60 μM, it was necessary to use Brownian dynamics (BD) simulations in implicit water in order to sample a statistically significant number of trajectories. Simulations were performed with the GeomBD program[5], for 80750 ns using a 2 fs timestep. The set-up was similar to the MD simulations, except that, to achieve a 60 μM concentration, only one substrate molecule was present in the 2.75×10^7 Å^3 simulation box, starting its trajectory from a randomly selected point around the stationary DNA positioned at the center. All molecules in these simulations were modeled as all-atom rigid bodies (no internal degrees of freedom) and the solvent and ions were both implicit. The simulations use a stationary grid representation of the DNA's electric field computed by a screened Coulomb potential, which extended 100 Å beyond the edges of the DNA. The program ran 500 independent trajectories of both paraoxon and DDVP under identical conditions except for their randomly-chosen starting positions. For both substrates, we repeated another set of 500 trajectories to ensure consistency in the observations (Figure S3.1).

In the BD simulations, only one substrate molecule diffused in the simulation space around the stationary DNA sequence. In this way, we were able to perform 500 replicate trajectories of 800 ns each, at concentrations that more closely match the experimental conditions. These simulations were performed in active electrostatics, but in the absence of van der Waals forces to avoid an artifact that a substrate adsorption to DNA. As a result,

substrates could diffuse freely for the entire BD simulation period and revealed that the effective concentration of paraoxon in all shells is higher than predicted by the MD calculations.

Radial distribution of paraoxon and DDVP around DNA. To quantify the influence of DNA on the distribution of surrounding paraoxon or DDVP molecules, we calculated the radial distribution of both substrates. The simulation space was partitioned into cylindrical shells centered on DNA as shown in Figure 1a. The number of substrate molecules (m_i) appearing in each cylindrical shell in a given frame, *i,* was summed over *n* total simulation frames and then divided by *n* to give the average number of molecules in each shell per frame. This quantity divided by the volume *V* of the shell is [S], the effective substrate concentration in a shell

$$[S] = \frac{\frac{1}{n}\sum_{i=1} nm_i}{V} \tag{8}$$

The bulk concentration $[S]_0$ is the number of substrate molecules being simulated divided by the total simulation volume, which can be compared to [S] to yield the ratio $[S]/[S]_0$, the effective concentration enhancement in each shell.

Calculation of paraoxon and DDVP residence time on DNA. The duration of substrate stay in close proximity to DNA was quantified from the MD simulation trajectories. We refer to the amount of time over which a molecule remains bound to the DNA as the "residence time" of the molecule. The residence time was calculated by

counting the number of consecutive frames in which a molecule was less than a cutoff distance (4.5 Å) from the DNA, measured between the closest atomic centers. To eliminate counting small molecular fluctuations, a molecule had to be below this cutoff for longer than 10 ps before being considered as "associated" or past this cutoff for longer than 10 ps before being considered as "dissociated".

3.10.1.2. Experimental Methods

SAFETY STATEMENT: The PTE substrate paraoxon is a known chemical irritant, please consult the appropriate Materials Data Safety Sheet (MSDS) and other safety information prior to using this chemical.

***Chemicals*.** 4-azido-L-phenylalanine was purchased from VWR. Chloramphenicol, kanamycin, Luria-Bertani (LB) broth, 10X PBS buffer, Tris-Base, dithiothreitol (DTT) and ethanol were purchased from Fisher BioRegents. Sodium chloride was purchased from Fisher Chemical. Sulfosuccinimidyl 4-(N-Maleimidomethyl) cyclohexane-1-carboxylate (Sulfo-SMCC), 10 and 30 kDa filters (UFC801024, UFC803024), SOC medium and SOB medium were purchased from Thermo Fisher Scientific. M9 media, paraoxon, methyl-parathion, zinc chloride, glycine, 2,2-dichlorovinyl dimethyl phosphate (DDVP), 2-Thiobarbituric acid (TBA), and ammonium sulfate were obtained from Sigma-Aldrich. 4-nitrophenol was purchased from Acros. Glycerol, Glacial Acetic Acid, bromophenol blue, 0.2 μM filters were purchased from Corning and sodium acetate was purchased from Fisher Scientific. Synthetic complete (SC) powder was purchased from Sunrise Science Products. Coomassie Brilliant Blue was purchased from Bio-Rad.

PTE cloning, expression and purification. A gene encoding the high activity S5 mutant of PTE gene (PTE R185K, N208G, R319S, Q211L list mutations here) as previously reported [6] was commercially synthesized (IDT DNA) and cloned into a pET-28b(+) expression vector using the NEBuilder HiFi DNA assembly method . The assembled expression vector was transformed into BL21DE3 cells for protein expression. Briefly, chemically competent *E. coli* cells were thawed on ice for 5 mins, 2 µL of the chilled solution (~1 ng/ul DNA) was added to 80 µL of competent cells, and the solution was mixed by pipetting and placed on ice for 30 mins. The transformation mixture then was heat shocked for 30 s at 42 °C and subsequently cooled on ice for 2 minutes. Room temperature SOC media (2% Vegetable Peptone, 0.5% Yeast Extract, 10 mM NaCl, 2.5 mM KCl, 10 mM $MgCl_2$, 10 mM $MgSO_4$, 20 mM Glucose media contents) was added into the tube to reach a final volume of 1 mL, prior to incubation at 37 °C (220 rpm) for 60 mins. Finally, 100 µL cells were spread onto a 37 °C warmed selection plate and incubated overnight at 37 °C. A successfully transformed colony was picked and transferred to 250 mL of sterilized LB broth containing 50 µg/mL kanamycin and 0.5 mM $ZnCl_2$ in 1 L shake flask. PTE expression was induced with 0.5 mM IPTG when the culture reached an OD_{600} = 0.6 (~ 1 h after inoculation and growth at 37 °C with 220 rpm shaking). Post induction cultures were moved to a 20 °C shaker incubator and expression continued for 48 h. All purification steps were carried out at 0-4 °C. Cells were harvested by centrifugation at 5000 g for 10 minutes and resuspended in 100 mL Tris-Zinc buffer (50 mM Tris, 100 µM $ZnCl_2$, pH 8.5) twice. After lysis by sonication (30s on/90s off, with total 5 min on time, all processed on ice), sample lysates were harvested by centrifugation at 15000 g for 30 mins.

Soluble protein fractions were first purified by ammonium sulfate precipitation; PTE was isolated from fraction collected containing 30-45% ammonium sulfate. After precipitation, PTE was resuspended in Tris buffer (50 mM Tris, pH 8.5), filtered through a 0.22 μm syringe filter, and isolated by anion exchange chromatography (HiPrep DEAE FF 16/10) at pH 8.5 with Tris Buffer as the wash buffer and Tris-NaCl buffer (1X Tris Buffer, 2 M NaCl, pH 8.5) as elution buffer. After isolation, the PTE sample was filtered over a 30 kDa filter to concentrate the sample and then buffer-changed to PBS buffer (pH 7.4) using size exclusion chromatography (Superdex 200 Increase 10/300 GL).

Incorporation of, and click-chemistry with p-azido-phenylalanine (pAzF). The site-specific incorporation of the non-canonical amino acid pAzF into PTE was accomplished by first introducing an amber stop codon, TAG, into the desired incorporation sites. Mutagenesis on the PTE gene (expressed from the pET-28b(+) vector as described above) to accomplish this was conducted with a Q5® Site-Directed Mutagenesis Kit and associated protocols (NEB). Protein expression with incorporated pAzF was accomplished by transforming both the pEVOL-pAzF plasmid [7], encoding a tRNA synthetase/tRNA pair specific to pAzF, and pET-28b(+)-PTE into *E. coli* BL21-AI cells. Plasmid harboring cells were used to inoculate 250 mL of M9 media containing 2 g/L synthetic complete (SC) powder (Sunrise Science Products), 0.5 mM $ZnCl_2$, 1 mM pAzF, 50 μg/mL kanamycin and 25 μg/mL chloramphenicol in a 1 L flask at 37 °C. PTE expression was induced with 0.5 mM IPTG, while expression from pEVOL-pAzF was induced with 0.2% (v/v%) arabinose once cells reached an OD_{600} = 0.6. Post induction cultures were moved to a 20 °C, 250 rpm shaker incubator, and expression continued for

48 hours. All subsequent purification steps were carried out at ~4 °C unless noted otherwise. Cells were harvested by centrifugation at 5000 g for 10 min and resuspended in 100 ml Tris-Zinc buffer (twice). After sonication, clarified lysates were produced by centrifugation at 15000g for 30 mins and PTE-pAzF mutants were purified the lysates as described in the previous section. If click-chemistry conjugation was to occur, the final purification step was dialysis against pH 7.4 Tris Buffer (20 mM Tris, pH 7.4) for at least 1 h at 4 °C. Post dialysis, 100 μmol DBCO-ssDNA was added and mixed with PTE-pAzF at room temperature for 3 hours. All reactions and subsequent purification steps were performed in the dark or under red light to avoid photolysis of the aryl-azide. Reacted samples were filtered with 10 kD filter and purified with a strong anion exchange column (HiTrap Q Sepharose Fast Flow; GE Healthcare) to remove unreacted DNA fragments and PTE-pAzF. Subsequently, 100 μmol of the complementary DNA strand was added to create double stranded DNA conjugates. Extra complementary strand was removed by passing samples through a 10 kD filter.

PTE-DNA conjugation by bifunctional sulfo-NHS-ester/maleimide chemistry. The control construct PTE-DNA_7 was synthesized as previously described in ref. [1,8]. First, 20 μL of 1 mM 5'-thiolated DNA was incubated with 120 μL of 1 M DTT for 3 h at room temperature to remove excess disulfide bonds. After reduction, activated DNA was recovered from excess DTT by precipitation (0.1x sample volume of 3 M sodium acetate and 2.5x sample volumes of ice-cold 100% ethanol) at -20 °C overnight and centrifuged at 4°C and 15,000g for 30 minutes. After precipitation, the DNA pellet was washed twice with 0.5 mL of ice-cold 75% ethanol and centrifuged at 4°C and 15,000g for 30 min. Next,

the 5'-thiolated DNA was reacted with an excess of sulfuric acid-SMCC (2 mg) for 3 h at room temperature with 250 rpm shaking. DNA was recovered by ethanol precipitation as described in the DTT step and resuspended in the PBS buffer. The concentration of sulfo-SMCC-ssDNA was determined by UV-Vis spectroscopy using the parameters provided by IDT. Purified PTE and sulfo-SMCC-ssDNA were subsequently mixed at a molar ratio of 1:100 for 3 h at room temperature in the dark. Excess DNA was removed by size exclusion chromatography (Superdex 200 Increase 10/300 GL; GE Healthcare) using PBS buffer. Purified samples were concentrated, filtered, and buffer exchanged through a 30 kD filter with TBS buffer (20 mM Tris, 120 mM NaCl, pH 7.4). Twenty-μL of 1 mM complementary DNA strand was then added, samples were mixed, heated at 45 °C for 5 min, and cooled at room temperature for 30 min to create PTE-DNA constructs. Finally, the samples were filtered through a 10 kD filter to remove excess complementary strand DNA, and then the buffer was exchanged to PBS to facilitate kinetic analysis.

UV-vis analysis of PTE:DNA complexes. The concentration and ratio of DNA to PTE was determined by UV-vis spectroscopy using the Beer-Lambert law. The absorption at 260 nm and 280 nm was recorded from 1.5 μL drop (0.2 mm light length) or 1 mL cuvette samples (1 cm light length), and the ratio of DNA to PTE was determined using eqns (9) and (10), with the following extinction coefficients: $\varepsilon_{260,PTE}$ = 18450 $cm^{-1}M^{-1}$, $\varepsilon_{280,PTE}$ = 29280 $cm^{-1}M^{-1}$, $\varepsilon_{260,DNA}$ = 193300 $cm^{-1}M^{-1}$, $\varepsilon_{280,DNA}$ = 108300 $cm^{-1}M^{-1}$

$$A_{260} = \varepsilon_{260,PTE} \times [PTE] + \varepsilon_{260,DNA} \times [DNA] \quad (9)$$

$$A_{280} = \varepsilon_{280,PTE} \times [PTE] + \varepsilon_{280,DNA} \times [DNA] \quad (10)$$

where ε is the molar extinction coefficient and *l* is the pathlength.

PTE and PTE-DNA kinetic analysis. All kinetic assays were conducted in 96-well microtiter plates at room temperature with absorbance monitored using a Synergy Neo2 multi-mode microplate reader (BioTek). Paraoxon hydrolysis was carried out in 150 µL reactions buffered to pH 7.4 with 1×PBS buffer, 20 nM enzyme, and 5, 10, 20, 40, 80, 100, 200, and 300 µM substrate PTE activity was monitored by measuring the absorbance of the p-nitrophenol leaving group at 405 nm. The extinction coefficient of p-nitrophenol at 405 nm was determined to be 12920 $cm^{-1}M^{-1}$ under the reaction buffer conditions. For DDVP, organophosphate hydrolysis was carried out in 100 µL of pH 7.4 1×PBS buffer with 20 nM PTE, and 0, 50, 100, 200, 400, 800 µM DDVP. Fifty-µL of the red color reagent 2-thiobarbituric acid (TBA, 2mM) and acetic acid (30%, v/v%) were added to reach a final volume of 150 µL. Post reaction, samples were heated at 100 °C for 1 h to facilitate the TBA reaction with dichloroacetaldehyde (product of DDVP hydrolysis) and generate red color (A_{490nm}) [9]. In all cases, the initial rate of reaction was calculated using a linear fit to the initial product time-curve, ensuring that less than 10% of the initial substrate had been consumed. Lastly, to determine the substrate on-rate, kinetic assays were conducted in reaction buffers of increasing viscosity as previously described [8,10]. Briefly, organophosphate hydrolysis reactions were carried out as described above but with the addition of varying concentrations of glycerol (0, 1,5, 10, 20, 30, and 40% (v/v)). All

reactions were conducted in 96-well microtiter plates in at least triplicate. Statistical analysis was accomplished in Prism GraphPad.

Electrophoretic analysis of pAzF incorporation into PTE. SDS-Page: Any kD™ Mini-PROTEAN® TGX Stain-Free™ Protein Gels. The sample buffer and running buffer are listed below. Experimental conditions: room temperature, 200 V for 30 mins.

4x SDS-PAGE Sample Buffer (Total 40 mL)	
1M Tris-HCl, pH 6.8	5 ml
20% Glycerol	8 ml
20% SDS	8 ml
10% ß-Mercaptoethanol	4 ml
0.5 mg/ml Bromophenol Blue	20 mg
DDI H_2O	15 ml

10x SDS-PAGE Running Buffer (pH 8.3)	
Tris base	30.3 g
Glycine	144.0 g
SDS	10.0 g
D.I. Water	To final volume of 1 L

Fluorescent analysis: 4-20% Mini-PROTEAN® TGX™ Precast Protein Gel. Buffer contents are listed below. Precision Plus Protein dual color standards were used as

a maker. Experimental conditions: room temperature, 100 V for 45 mins. After running, the gel was stained by TAMRA-alkanyl (12 μl, 100 μM).

4x non-denaturing sample buffer (Total 40ml)	
1M Tris-HCl, pH determined based on requirement	5 ml
100% Glycerol	16 ml
0.5 mg/ml Bromophenol Blue	20 mg
DDI H_2O	19 ml

Native-Gel: 4-20% Mini-PROTEAN® TGX™ Precast Protein Gel. Buffer contents are listed below. Experimental conditions: 20 mM Tris running buffer, 4 °C, 120 V for 1 hour. After running, the gel was stained by Coomassie blue and distained by distaining solution.

Coomassie Stain Solution	
Ethanol	150 ml
Glacial Acetic Acid	50 ml
DDI H_2O	300 ml
Coomassie Brilliant Blue R250	1g

Destaining solution

Ethanol	1200 ml
Glacial Acetic Acid	400 ml
DDI H_2O	2.4 L

Calculation of Model Parameters. The parameter γ in our model depends only on structural and geometric features of the system. The offset angle, θ_{DNA}, grows as DNA is conjugated further from the active site. It is measured as the angle between a vector running from the enzyme center through the active site and a vector running from the enzyme center through the residue onto which DNA was conjugated (Figure S3.4). To choose conjugation sites covering a range of distances from the active site, the distances between each residue and active site had to be measured (Figure S3.2). To do this, dummy atoms were placed tracing the shortest path along the PTE surface from the conjugation position to the active site entrance. The straight-line distance between each pair of dummy atoms was summed to approximate the total distance to the active site. The radius of the active site cavity, r_{AS}, is measured by the distances between two pairs of residues bounding the active site cavity. These form the axes of an oval that roughly approximates the surface area of the cavity.

Example calculation of predicted K_M enhancement

	Distance (Å)	Θ_{DNA} (°)	$K_M/K_{M,app}$ (expt)	$[S]/[S]_0$	γ
D133^{pAz}F	6.0	22.00	4.36	3.60	1.21
K175^{pAz}F	8.0	35.00	7.09	2.00	3.55
F149^{pAz}F	16	46.00	4.35	1.72	2.75
A78^{pAz}F	36	86.00	2.18	1.38	2.23
D160^{pAz}F	40	120.00	2.21	1.35	1.78
T352^{pAz}F	53	141.00	2.06	1.26	1.51
K294^{pAz}F	70	166.00	1.29	1.18	1.18
A364^{pAz}F	73	172.00	1.13	1.10	1.10

The K_M enhancement for each conjugation site was calculated as follows. We will demonstrate the model for D160, for which θ_{DNA} is ~120° or 2.1 radians. With r_{AS} = 7.7 and r_{DNA} = 18.0, we have

$$\gamma = 1 + \beta\left[\frac{\pi - \theta_{DNA}}{\pi}\left(\frac{r_{AS+DNA}}{r_{AS}} - 1\right)\right] = 1 + 1\left[\frac{\pi - 2.1}{\pi}\left(\frac{18.0 + 7.7}{7.7} - 1\right)\right] = 1.78$$

We then use the effective concentration ($[S]/[S]_0$) in the shell 40-45 Å from DNA, 1.35, to predict the overall K_M enhancement

$$\frac{K_M}{K_{M,app}} = \frac{[S]}{[S]_o}\gamma = 1.35 \times 1.78 = 2.40$$

3.10.2 Supporting Figures

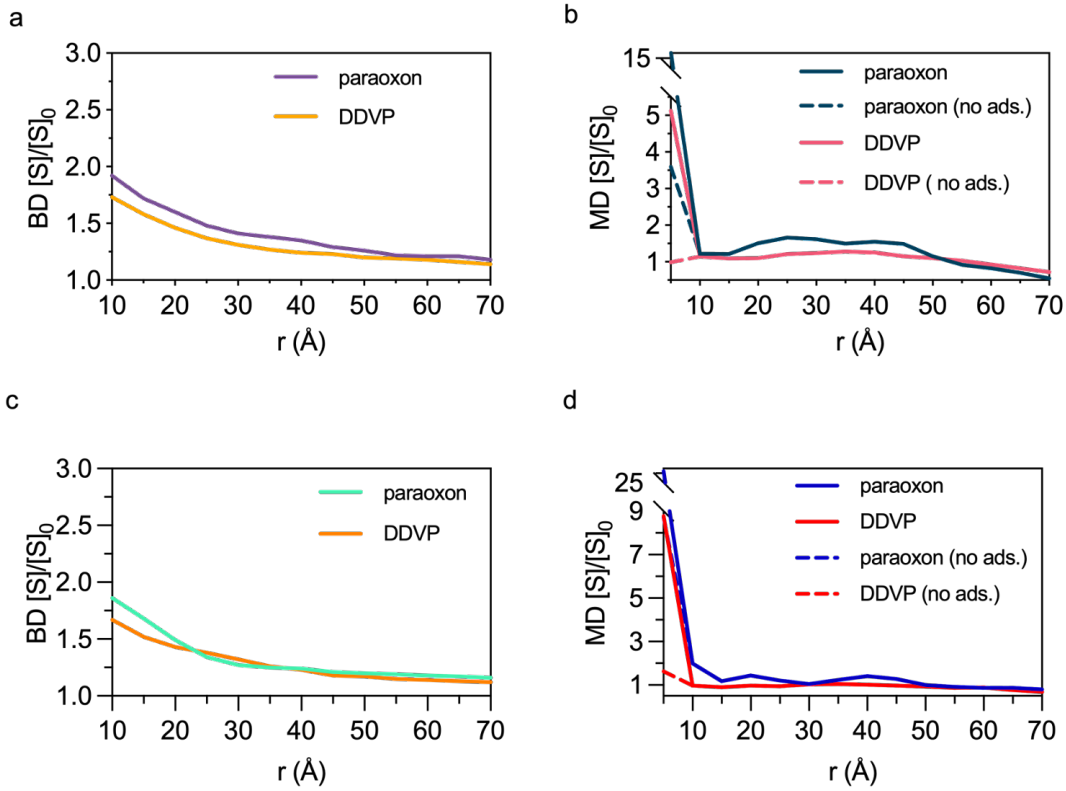

Figure S 3.1 Effective substrate concentration as a function of distance from DNA in the first set of BD (a) and MD (b) simulation, and second set of BD (c) and MD (d) simulation. Paraoxon shows larger effective concentration increase than DDVP over most of the range in both MD simulations. Dashed lines for each substrate are the concentration when adsorbed molecules are not included in the count. This only affects the value of the first shells. Substrate concentration in the first and second 60 µM BD simulations shows a smooth curve for both substrates in both simulations, with paraoxon showing greater effective concentration increase than DDVP over the entire range. Comparing the BD and MD results helps discern an effect that occurs due to the low number of substrate molecules (64) in the latter. Such a small number of simulated molecules results in the prediction of artificially low concentrations in shells beyond the first, since, when a substrate adsorbs to the DNA, nearby shells become depleted of substrate since there is no surrounding bulk solution from which other molecules can fill in behind. This results in the dip seen in Figure S3.1a and Figure S3.2b, which causes the gradual uptrend to reverse. Concentration reaches a minimum in the second shell before spiking upward in the closest shell due to the van der Waals (VdW) forces between substrate and DNA that become appreciable at intermolecular distances around 8-10 Å. However, in the BD simulations, this depletion artifact is not present since those simulations included only electrostatic interactions and excluded vdW forces, preventing substrate adsorption.

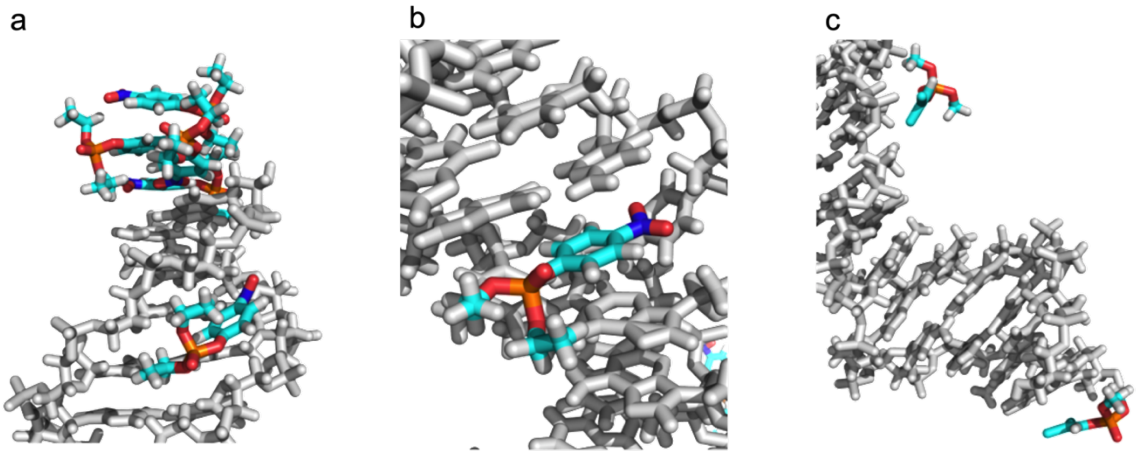

Figure S 3.2 Molecular simulation of paraoxon and DDVP binding to DNA. Frames from MD simulations show various binding modes for paraoxon and DDVP. (a) One molecule of paraoxon is shown bound in the minor groove, while four other paraoxon molecules are shown stacked on the end of DNA. (b) Paraoxon intercalated in the DNA major groove. Substrates adsorbed to the DNA were not included in the analysis to quantify the effective concentration shown in Figure 1. (c) DDVP molecules typically adsorbed only briefly through electrostatic interactions with the DNA backbone or with the DNA strand ends.

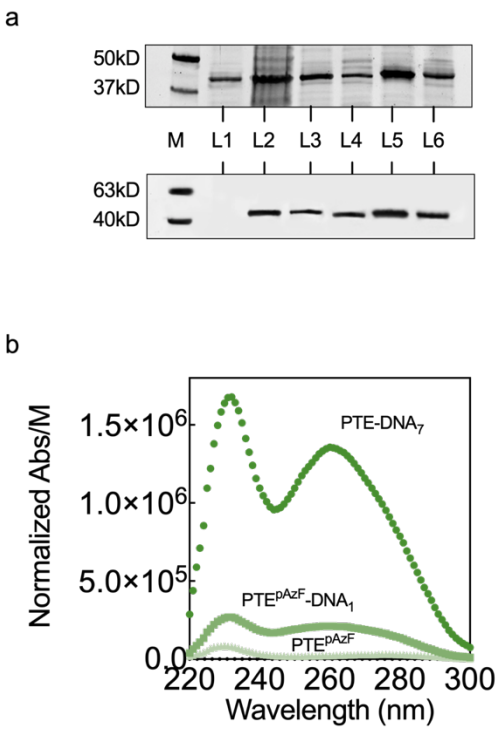

Figure S 3.3 Site specific DNA conjugation to phosphotriesterase (PTE). (a) Electrophoretic gel analysis of various PTE mutants. The top image is a stain free acrylamide gel showing the size of PTE and PTE mutant which incorporated with pAzF. The bottom is a fluorescent image of a separate gel containing the same samples modified in situ with a tetramethylrhodamine (TAMRA) alkyne probe to confirm incorporation of pAzF. M, protein marker; L1, PTE without incorporated pAzF; L2, K175pAzF; L3 F149pAzF; L4 A78pAzF; L5, K294pAzF; L6, A364pAzF. (b) UV-vis spectra of PTE K175pAzF, PTE K175pAzF-DNA_1, and PTE-DNA_7 normalized based on the PTE concentration. Conjugation of DNA to the PTE structure introduces a spectral peak at 260 nm that is proportional to the amount of DNA attached to the structure.

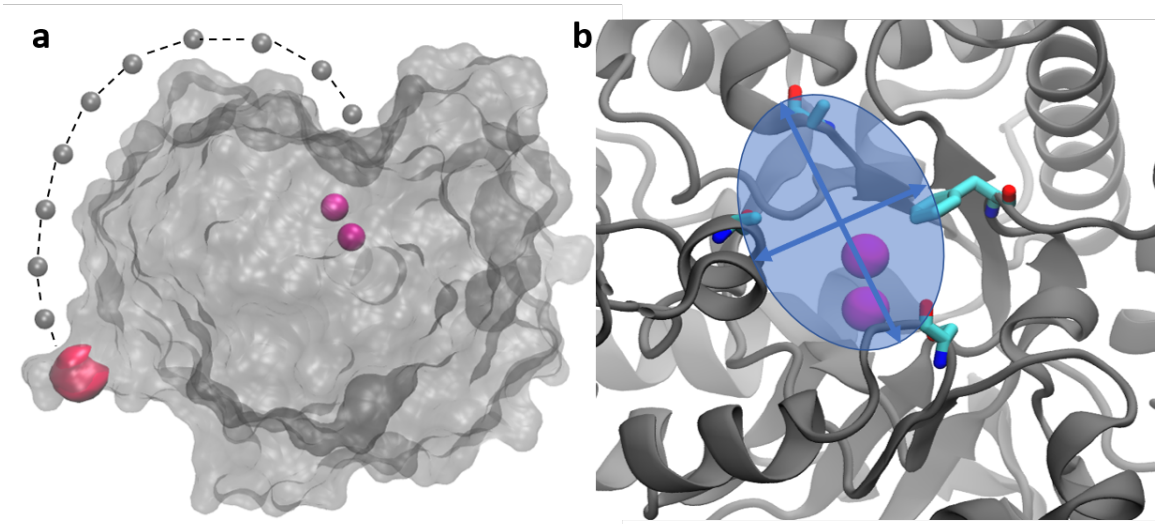

Figure S 3.4 Schematic diagram of measured distances and active sites. (a) Dummy atoms (grey spheres) were placed tracing the shortest path from the conjugation position (red) to the active site (Zn atoms shown in pink) to measure the total distance. (b) Distances between two pairs of residues bounding the active site cavity form the oval used to estimate r_{AS}.

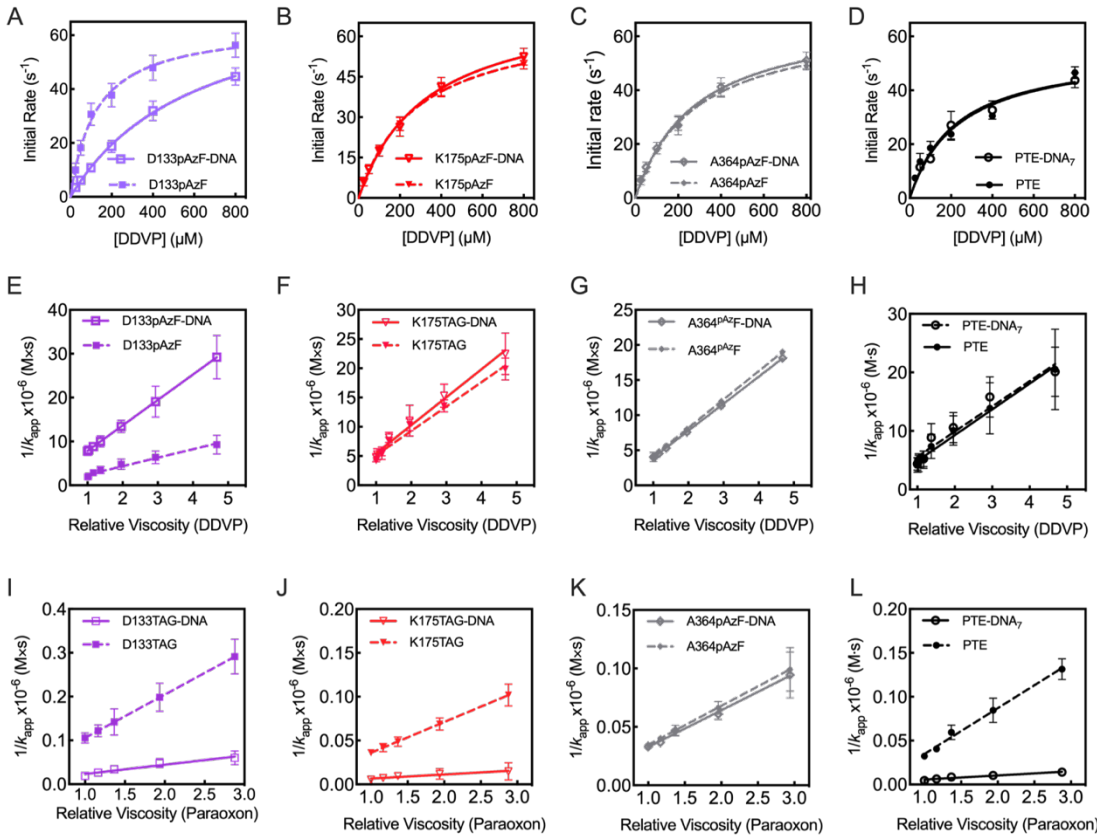

Figure S 3.5 Kinetics analysis of PTE and PTEpAzF (D133, K175, A364) with DDVP and paraoxon before and after DNA site-click. In all graphs PTE-pAzF (or PTE) without conjugated DNA is shown with a solid line and with a dashed line after DNA modification. (A, B, C, D) Kinetic analysis of PTE-pAzF and PTE-pAzF-DNA with DDVP. Plots of the reciprocal of the overall apparent reaction rate ($1/k_{app}$ or K_M/k_{cat}) vs. relative viscosity of PTE-pAzF and PTE-pAzF-DNA with DDVP (E, F, G, H) and paraoxon (I, J, K, L) are also shown. The reciprocal of the slope of the linear fit to $1/k_{app}$ vs time is the on-rate, k_1. Kinetic parameters for each analysis are provided in Table S3.1 below.

Table S 3.1 The kinetics parameters of PTE and PTE-DNA (D133, K175, A364) reacting with DDVP and paraoxon. Statistical significance in comparison to PTE in the absence of DNA conjugation is stated with "ns" indicating a p value > 0.05, * is p<0.05.

	DDVP						Paraoxon	
	k_{cat} (s^{-1})		K_M (μM)		k1 ($\mu M^{-1}s^{-1}$)		k1 ($\mu M^{-1}s^{-1}$)	
D133pAzF	64.27±5.09	ns	128.37±13.98	*	0.51±0.04	*	10.12±0.12	ns
D133pAzF-DNA	61.38±11.40	ns	648.37±80.38	*	0.17±0.01	*	47.25±2.86	*
K175pAzF	64.52±3.26	ns	283.70±31.79	ns	0.24±0.02	ns	28.57±0.27	ns
K175pAzF-DNA	64.53±6.37	ns	341.53±55.51	*	0.21±0.01	ns	213.58±36.01	*
A364pAzF	66.52±3.19	*	277.43±31.06	ns	0.25±0.02	ns	30.05±2.15	ns
A364pAzF-DNA	69.24±5.61	*	274.83±25.00	ns	0.26±0.02	ns	31.80±2.56	ns
PTE	56.47±5.63		246.53±30.26		0.24±0.06		24.41±2.67	
PTE-DNA_7	56.46±4.71	ns	253.73±25.79	ns	0.24±0.05	ns	221.71±15.93	*

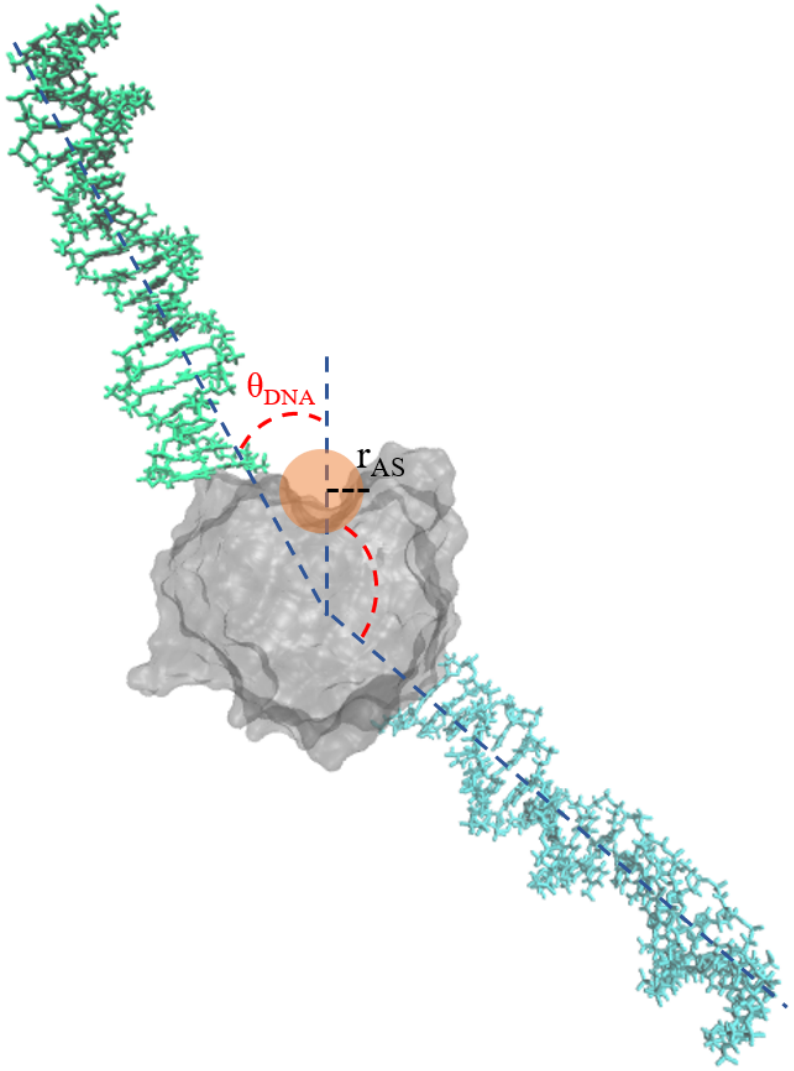

Figure S 3.6 Depiction of the offset angle, θDNA (red dashed lines). The green and blue DNA strands represent different possible conjugation positions. PTE active site indicated by orange circle.

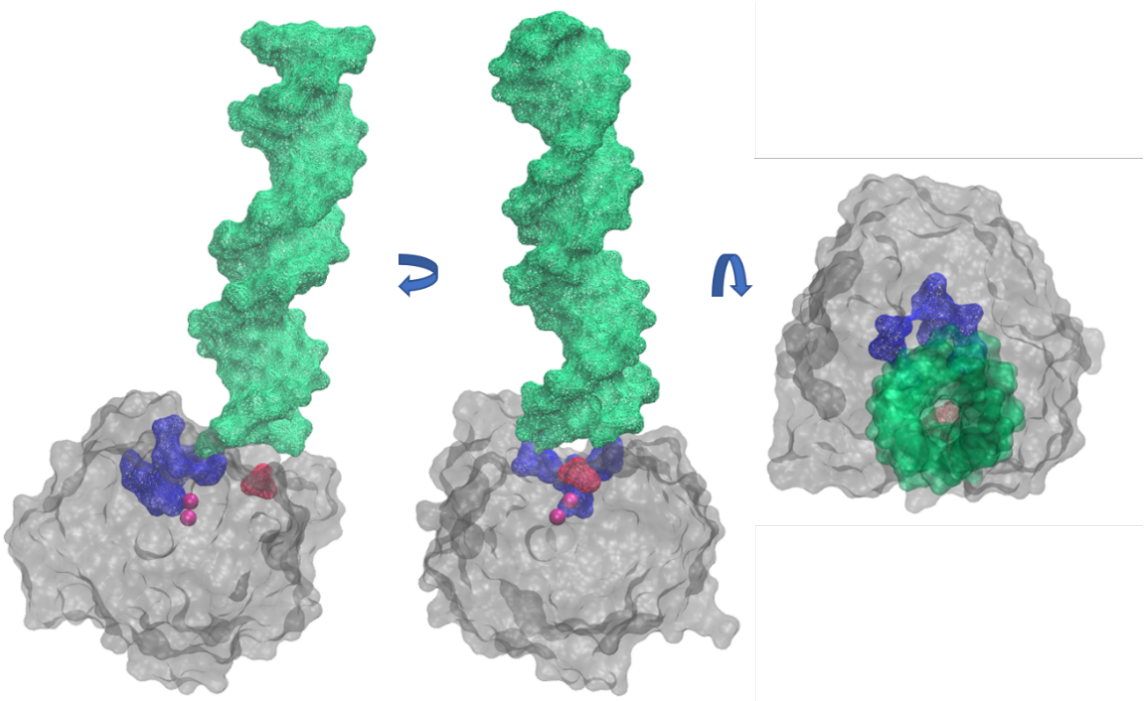

Figure S 3.7 DNA conjugated at a position proximal to the active site can partially block the active site cavity (blue, with Zn atoms in pink), resulting in a smaller than expected enhancement of K_M. Pictured here is PTE-DNA with DNA attached at residue Asp133 (red).

3.10.3 SI Reference

1. Phillips, J. C. *et al.* Scalable molecular dynamics with NAMD. *J. Comput. Chem.* **26**, 1781–1802 (2005).

2. Ivani, I. *et al.* Parmbsc1: a refined force field for DNA simulations. *Nat. Methods* **13**, 55–58 (2016).

3. Wang, J., Wolf, R. M., Caldwell, J. W., Kollman, P. A. & Case, D. A. Development and testing of a general amber force field. *J. Comput. Chem.* **25**, 1157–1174 (2004).

4. Jakalian, A., Jack, D. B. & Bayly, C. I. Fast, efficient generation of high-quality atomic charges. AM1-BCC model: II. Parameterization and validation. *J. Comput. Chem.* **23**, 1623–1641 (2002).

5. Roberts, C. C. & Chang, C.-E. A. Analysis of Ligand-Receptor Association and Intermediate Transfer Rates in Multienzyme Nanostructures with All-Atom Brownian Dynamics Simulations. *J. Phys. Chem. B* **120**, 8518–8531 (2016).

6. Roodveldt, C. & Tawfik, D. S. Directed evolution of phosphotriesterase from Pseudomonas diminuta for heterologous expression in Escherichia coli results in stabilization of the metal-free state. *Protein Eng. Des. Sel.* **18**, 51–58 (2005).

7. Chin, J. W. *et al.* Addition of p-azido-L-phenylalanine to the genetic code of Escherichia coli. *J. Am. Chem. Soc.* **124**, 9026–9027 (2002).

8. Lang, X., Hong, X., Baker, C. A., Otto, T. C. & Wheeldon, I. Molecular binding scaffolds increase local substrate concentration enhancing the enzymatic hydrolysis of VX nerve agent. *Biotechnol. Bioeng.* **117**, 1970–1978 (2020).

9. Guzmán-Chozas, M., Vicario, I. M. & Guillén-Sans, R. Spectrophotometric profiles of off-flavor aldehydes by using their reactions with 2-thiobarbituric acid. *J. Agric. Food Chem.* **45**, 2452–2457 (1997).

10. Gao, Y., Roberts, C. C., Toop, A., Chang, C.-E. A. & Wheeldon, I. Mechanisms of Enhanced Catalysis in Enzyme-DNA Nanostructures Revealed through Molecular Simulations and Experimental Analysis. *Chembiochem* **17**, 1430–1436 (2016).

Chapter 4. Effects of electrostatic guidance by different supercharged sfGFP scaffold on the cascade kinetics enhancement[3]

4.1 Abstract

The cascades in nature often use a spatial organization to generate substrate channeling processes, a method that has been widely used for increased catalysis in many manufactured multi-enzyme cascades. The mechanism of the enhancement in cascade kinetics by molecular scaffolds remains to be explained: molecular scaffolds can form substrate channels; yet, these scaffolds may also affect the microenvironment of the assembled enzyme. In this project, different-charged (+36, 0, -30) superfolder green fluorescent protein (sfGFP) regulated the molecular flux of the negatively charged intermediate, glucose-6-phosphate (G6P), between hexokinase II (HK2) and glucose-6-phosphate dehydrogenase (G6PD). Although the apparent turnover rate and transient time of the cascade were subject to the various sfGFP modifications, the change in the initial rate implies that the enhanced kinetics does not originate from channeling alone; sfGFP impacts the charged substrates microenvironment by electrostatic interaction, which manifests as a change in the affinity or apparent K_M of the individual enzyme for charged substrates. In addition, we evaluated the effect of sfGFP scaffolds on the kinetics of the cascade reaction by modeling. Specifically, we first used the kinetic constants of individual

[3] This chapter is in preparation for publication with the title, "Effects of electrostatic guidance by different supercharged sfGFP scaffold on the cascade kinetics enhancement". This paper is co-authored by Xiao Hong and Walaa Abdallah (co-first authors) along with Drs. Scott Banta and Ian Wheeldon (co-corresponding authors). Xiao Hong was responsible for the experimental aspects of this work, while the co-first authors worked together on the modeling aspects of the paper together.

enzymes before and after modification by sfGFP as parameters to build a cascade reaction kinetic model. In a statistically significant way, the simulated data were statistically closely related to the experimental data. This correlation suggests that the microenvironment in which sfGFP affects the charged substrate mainly electrostatically alters the kinetics of the individual enzymes, which in turn enhances the cascade reaction. Then, we described the kinetics of the cascade reaction by two models (channeling and non-channeling). The experimental data fitted two models. Although both models fed back k-values, the channeling model had non-negligible errors. Converting the k-values of the non-channel models into Michaelis constants was not statistically significantly different from the experimental results, suggesting that changes in single-step enzyme kinetics are more critical in cascade reaction enhancement. Thus, the altered kinetics of single-step enzymes due to microenvironmental changes is an essential part of the cascade, and we can design controlled experiments to enhance the discovery of substrate channels when necessary and provide alternative explanations when required.

4.2 Introduction

A wide range of life-sustaining enzyme cascades have been observed to form complexes in space by compartmentalization, co-localization, and sometimes through self-assembling. These complexes can isolate some or all the intermediates of the cascade reaction from the bulk environment, thus enhancing essential metabolism. Over the last five or more years, efforts have been made to create synthetic multienzyme structures that mimic similar structures found in nature, often with the goal of understanding the kinetic

effects of bringing two or more enzymes in close proximity [1–3]. Although there is some debate in the field [4–6], it is widely accepted that substrate channeling, that is the transfer of a cascade intermediate from an upstream to a downstream active site with first diffusing to the bulk environment, can occur through various various mechanisms, including bounded diffusion, physical tunnels [7], chemical swing arms [8], and electrostatic channeling [9,10]. Electrostatic channeling regulates the transition of charged intermediates between active sites via electrostatic interaction with the oppositely charged surface. In the past decades, two well-researched examples of electrostatic channeling have been a priority. In the tricarboxylic acid (TCA) cycle, malate dehydrogenase (MDH) and citrate synthase (CS) form a positive electrostatic channel to guide oxaloacetate, a negatively charged intermediate, through the active site without mixing in the bulk environment [11]. Another well-studied example is dihydrofolate reductase-thymidylate synthase (DHFR-TS), a bifunctional enzyme with a positively charged protein surface that crosses two active sites and guides the diffusion of negatively charged intermediates (dihydrofolate) [12].

In addition, further progress in biomolecular engineering and the design of enzymes capable of organizing and localizing at the nanoscale resolution enables substrate channeling in cascades. For example, charged residues control the diffusion of charged intermediates and form substrate channels by electrostatic interactions [13,14]. The cascade process consists of individual enzyme processing and intermediates diffusion and capture. The enhancement of cascade kinetics has been observed in the substrate channel. One assumption of this enhancement is shortening the transient time (the time required to reach the steady-state flux of intermediates in the cascade reaction). However, since substrate

channeling was first described more than 30 years ago, kinetic enhancement due to substrate channels has been a source of contention. This dispute is still ongoing today. Part of the dispute is that the scaffolds used to construct substrate channeling can themselves make significant changes to the kinetics of the enzyme [15]. Specifically, these scaffolds bring high charge density and potential substrate binding sites, introducing a complex local environment that leads to significant changes in enzyme kinetics [16].

In this project, we created a cascade consisting of hexokinase II (HK2) and glucose-6-phosphate dehydrogenase (G6PD) linked by supercharged sfGFP to investigate the mechanism of cascade enhancement. The charged residues on the supercharged (+36, 0 ,-30) sfGFP surface guide the molecule flux of the negatively charged intermediate, glucose-6-phosphate (G6P) via electrostatic forces and form the substrate channel [13,14]. The turnover rate of the cascade, k_{cat} or the reciprocal of overall cascade reaction interval, was significantly increased by (+36)sfGFP and decreased by (-30)sfGFP. The transient time is defined as the time the system spends to reach the steady-state, which is used to calculate the transport efficiency of electrostatic channeling. In this study, the transient time was decreased by (+36)sfGFP, whereas it increased by (-30)sfGFP. The transient time for a perfect channeling was close to zero; for an electrostatically channeled system, a lower lag time indicates increased channeling efficiency [17]. However, the variation of the initial rate after sfGFP rendered the expectation of substrate channeling ambiguous because the initial rate change implied the kinetics change happened at individual enzymes, which also impacted the cascade kinetics directly. Given this, we studied the kinetic change in individual enzymes before and after sfGFP modification. The affinity of negatively

charged substrates (ATP, $NADP^+$, G6P) in individual enzymes and the k_{cat} of HK2 were increased by (+36)sfGFP and decreased by (-30)sfGFP. Electrostatic interaction played an essential role because non-charged substrate (glucose) got no benefit from the sfGFP modification, and (0)sfGFP did not change the kinetics in individual enzymes.

With these parameters, we established the cascade kinetic model. The model represents the change in concentrations of reactants and products in the cascade over time by the rate law, which is a combination of individual enzyme rate law with G6P as a connection. The model is a series of standard differential equations with the parameters set as the kinetic constants from individual enzymes before and after sfGFP modifications. We discovered that the simulation results were in good agreement with the experimental results of the cascade before and after the sfGFP modification. Furthermore, we built two models to describe the cascade directly; the channeling model considers the substrate channel, and the non-channeling model only considers individual enzymes' processes. The experiment data were fitted to calculate the k-values in both models. Although both models fitted well with experiment data, the channeling models brought non-negligible errors in k-values, while the non-channeling model did not. The k_{cat} and Michael constant were simplified from the k-value of the non-channeling model and had no significant difference from the pseudo-Michael kinetic assay result. Compared to the transient time of the intermediates seen by channeling, this result suggests that sfGFP is more likely to cause charged molecules to accumulate around the attached HK2 and G6PD via its own charge, forming a microenvironment. Such a change directly affects the kinetics of HK2 and G6PD, respectively, resulting in the overall catalysis change of the cascade.

4.3 Result and Discussion

4.3.1 Constructing HK2-sfGFP-G6PD

It is widely believed that substrate channels formed by electrostatic guidance can enhance the apparent turnover rate of the cascade ($k_{cat,app}$). For a cascade reaction period ($\tau_{cascade}$), the assumption is that electrostatic guidance shortens the transient time/intermediate diffusion time, see the Figure S4.1a [18]. HK2 and G6PD were utilized as models to explore this hypothesis. HK2 phosphorylates glucose via ATP to produce glucose-6-phosphate and ADP. G6PD reduces $NADP^+$ to NADPH and oxidizes glucose-6-phosphate to 6-phosphogluconolactone. We created three sfGFPs with different charges (+36, 0, -30) to control the diffusion of negatively charged intermediate G6P (Figure 1b) to mimic the substrate channel. It was hypothesized that the (+36)sfGFP would attract and confine negatively charged G6P, while (-30)sfGFP would have the opposite effect. The (0)sfGFP is predicted to have no interaction with G6P because it is uncharged (see Figure 1a and 1b).

To construct this cascade complex, p-azido-phenylalanine (pAzF) was introduced at the N-terminal end of HK2, and p-alkyne-phenylalanine (pAkF) was introduced at the E131 position of sfGFP. pAzF and pAkF were linked by a copper-catalyzed azide-alkene cyclization reaction. Then the N terminus of sfGFP fuse the SpyTag, and the N terminus of the G6PD fuse the SpyCatcher. G6PD is connected to the N terminus of sfGFP via the SpyTag/SpyCatcher (see Figure S4.1b). The b-factor describes the mobility of the atomic positions [19]. The E131 site on the surface is chosen because it has a low b-factor, and its

side chain sticks out of the protein surface (see Figure S4.2). The fluorescence signal of sfGFP is structure-dependent [20]. The introduction of pAkF did not affect the structure of sfGFP, as evidenced by a statistically insignificant change in fluorescence signal (see Figure S4.3). SDS-PAGE shows the relative sizes of the HK2-sfGFP-G6PD complex with HK, G6PD, sfGFP, HK2-sfGFP, and G6PD-sfGFP (Figure 1c, with (+36)sfGFP as an example).

4.3.2 Substrate channeling appears to boost the cascade reaction's overall turnover rate.

The apparent Michaelis-Menten constants of the HK2-sfGFP-G6PD complex through kinetic tests were determined by saturating all substrates except for one [21] and compared to the HK2/G6PD (equimolar) mixture as a control (see Figure 4.2).

The apparent turnover rate of the cascade ($k_{cat,app}$) increased with (+36)sfGFP by 65.04±5.47 % in glucose, 54.51±4.64 % in ATP, and 56.19±4.59 % in $NADP^+$. No significant effect of $k_{cat,app}$ was observed with (0)sfGFP (≤ 10 %, and no significant statistical difference), while a decrease of $k_{cat,app}$ by 28.76±5.14 % in glucose, 25.75±4.97 % in ATP, and 19.47±5.13 % in $NADP^+$ was observed with (-30)sfGFP.

The apparent Michaelis constants ($K_{M,app}$) of the HK2-sfGFP-G6PD complex are significant under varied substrate conditions. For the ATP and $NADP^+$, the $K_{M,app}$ of (+36)sfGFP decreased by 31.67±11.41 % in ATP, and 14.96±3.18 % in $NADP^+$. On the other hand, the $K_{M,app}$ of (-30)sfGFP increased by 25.75±4.97 % in ATP, and 18.50±4.13 %

in $NADP^+$. The $K_{M,app}$ of (0)sfGFP had no significant change (≤ 10 %, and no significant statistical difference). Considering ATP and $NADP^+$ are both negatively charged molecules. These negatively charged substrates were likely attracted to (+36)sfGFP (decreasing $K_{M,app}$ or increasing affinity), and repelled by (-30)sfGFP (decreasing affinity decreases or increasing $K_{M,app}$), and ignored by (0)sfGFP. Glucose is uncharged, resulting in all three sfGFP with the same affinity for glucose (see Table 4.1). This finding suggests that, except for controlling the diffusion of intermediate, charged sfGFP influenced the kinetics of the HK2-sfGFP-G6PD cascade by changing the affinity of cascade towards charged substrates.

4.3.3 The increase in the overall turnover rate of cascade catalysis is not entirely explained by substrate channeling.

The overall cascade process ($\tau_{cascade}$) consists of HK2 production (τ_{HK2}), G6P diffusion along the sfGFP or in the bulk environment (τ_{G6P}), and depletion by G6PD (τ_{G6PD}). Only G6P is thought to be reduced by the substrate channel.

A saturating concentration of 1 mM glucose and 40 μM saturating $NADP^+$ was utilized to reduce HK2 synthesis and G6PD depletion impacts [22]. Furthermore, the ATP concentration should not exceed 40 μM at this time; otherwise, G6P may be produced in excess and diffuse into the bulk environment. 25 μM ATP was chosen in this case.

The transient time variation after sfGFP modification is shown in Figure 4.3. Compared to the HK2 and G6PD mix, (+36)sfGFP shortened the transient time by 59.98±6.17 % and suggested that (+36)sfGFP might effectively boost G6P transport. On

the other hand, (-30)sfGFP increased transient time by 70.03±5.43 %, while (0)sfGFP had no significant effect on transient time. Thus, (+36)sfGFP increased the k_{cat} or shortened the cascade process by shortening the G6P diffusion period. The k_{cat} decreased by (-30)sfGFP because of the transient time increasing.

However, compared to the HK2/G6PD mix, the initial rate of the cascade was enhanced by (+36)sfGFP, lowered by (-30)sfGFP, and insignificantly altered by (0)sfGFP (see Table 4.2). The initial rate change implied the kinetic change on the HK2 and G6PD, respectively. Thus, the cascade enhancement is caused not only by the substrate channel but also by the kinetic change of individual enzymes.

4.3.4 Following sfGFP modification, the kinetics of both HK2 and G6PD were altered.

To further our understanding of the change at individual enzymes after sfGFP modification, in this context, we examined HK2 and G6PD before and after sfGFP modifications (see Figure 4.4).

HK2 follows a random bi-bi mechanism (see method equation 1) . The kinetics of HK2 was altered after sfGFP modification (Figure 4.4 a-d). The turnover rate increased by 42.45±3.87 % with (+36)sfGFP. Moreover, the affinity of HK2 to ATP (negatively charged) was enhanced by (+36)sfGFP (decrease in $K_{M,ATP}$ by 25.18±2.94 %). The turnover rate decreased by 24.06±4.07 % with (-30)sfGFP. Meanwhile, (-30)sfGFP repelled ATP and decreased the affinity ($K_{M,ATP}$ increasing by 73.65±3.24 %). (0)sfGFP did not have a

statistically significant effect on the kinetics. The sfGFP modification did not affect (≤ 10 %, and no significant statistical difference) the affinity of HK2 for glucose, presumably since it is uncharged (see Table 4.3). G6PD follows the ordered bi-bi mechanism (see method section equation 2) . G6PD kinetics was altered by the change in sfGFP (Figure 4.4 e-h, see Table 4). Although the k_{cat} has no significant change, the affinity of G6PD towards negatively charged G6P and $NADP^+$ was increased with (+36)sfGFP by decreasing $K_{M,G6P}$ by 21.43±7.53 % and $K_{M,NADP+}$ by 15.63±5.48 %. (-30)sfGFP repelled the negatively charged substrates and lowered the relative affinity towards G6PD by increasing 15.97±5.12 % in $K_{M,G6P}$, and 14.06±4.98 % in $K_{M,NADP+}$. (0)sfGFP did not impact the kinetic behavior of G6PD (≤ 10 %, and no significant statistical difference).

As a result, sfGFP modifies the kinetics of HK2 and G6PD, respectively. Given that the $\tau_{cascade}$ incorporates not just τ_{G6P}, but also τ_{HK2} and τ_{G6PD}, variations in cascade output may be attributable to changes in the kinetics of the individual enzymes.

4.3.5 The catalytic kinetic changes of cascade under different sfGFP modifications are well explained by the kinetic changes of individual enzymes after sfGFP modification.

Given the importance of individual enzyme kinetics, we attempted to explain the kinetic performance of the cascade under the effect of sfGFP using the kinetic characteristics of the individual enzyme after sfGFP modification. Using the kinetic constants (k_{cat}, α, and K_i of HK2 and k_{cat}, K_M, and K_i of G6PD before and after sfGFP

modification) as known parameters, the cascade model (see the method section) was used to track the concentration changes over time (glucose, ATP, ADP, G6P, $NADP^+$, NADPH, 6PL, showing in Figure S4.5, with G6P and NADPH showing in Figure 4.5). Because individual enzyme kinetics are sensitive to environmental/local substrate concentrations [23], we investigated the following concentration situations. (1) The kinetics of HK2 is low, and the kinetics of G6PD is high (Figure 4.5A), which occurs when glucose is 50 μM, ATP is 25 μM, and $NADP^+$ is near saturation (40 μM). (2) The kinetics of both HK2 and G6PD were high (Figure 5B and Figure 5C) when glucose was saturated at 1000 μM or ATP saturated at 500 μM, while $NADP^+$ guaranteed saturation. (3) When HK2 activity is high, with glucose or ATP saturated. In comparison, the kinetics of G6PD is lower than before, with $NADP^+$ 5 μM (Figure 4.5D, Figure 5E, and Figure 4.5F). Picking up the data following the 10% rule, we compared the experimental and simulated NADPH data for all concentrations of interest in the interval between lag phase and steady-state. The results of the correlation analysis showed that the simulations fitted the experimental data sufficiently well (see Figure S4.6). The correlation test revealed that the experimental and simulated findings were linearly associated. Moreover, the standard residuals of data from simulation and experiment were in the range [-2,2], shown in Figure S4.7. This result demonstrated that the altered kinetics of the HK2-sfGFP-G6PD cascade could be adequately described by the kinetics change of a single enzyme in the cascade each step after sfGFP modification.

Two models (channeling model and non-channeling model) were created and fitted to the experimental data independently to assess the influence of substrate channeling on

the cascade. The results showed that both models could fit the experimental data of HK2-sfGFP-G6PD, but the channeling model produced a non-negligible error. In contrast, the non-channeling model fitted the data better and produced acceptable errors (see Figure S4.8 and Figure S4.9). Since the non-channeling model generates less error than the channling model, we believe that this model fits the data better than the channeling model (see table S4.1 for k-value of non-channeling model and table S4.2 for k-value of channeling model). We further combined the obtained k values from the non-channeling model to obtain the k_{cat} and inferred the Michaelis constant for G6P based on the order bi-bi mechanism (see table S3). For the HK2/G6PD mix, k_{cat} = 7.62±0.19 s^{-1}, $K_{M,G6P}$ = 9.52±0.13 μM. The (+36)sfGFP modification resulted in k_{cat} increasing to 8.58±0.21 s^{-1}, while the affinity of G6P increased and $K_{M,G6P}$ reached 8.87±0.18 μM. (0)sfGFP modification did not significantly change k_{cat} (8.08±0.24 s^{-1}), and $K_{M,G6P}$ (9.87±0.18 μM). (-30)sfGFP decreased k_{cat} (6.95±0.23 s^{-1}) and decreased G6P affinity as well ($K_{M,G6P}$ increases to 12.01±0.15 μM). The k_{cat} and Michaelis constant from the non-channeling model explained that the alteration of kinetics in both parts could effectively affect the catalysis of the cascade. The supercharged sfGFP affected the clustering of charged molecules surrounding the cascade, resulting in a shift in cascade dynamics in the form of a change in k-value.

4.4 Conclusion

Substrate channeling in cellular biochemistry and as a strategy aimed at synthesizing multienzyme complexes is a fascinating and engaging idea. The depth and

breadth of the debate surrounding the kinetic effects of substrate channels over the past three decades is a testament to our collective interest in this topic and the potential of this concept to explain the unexpected phenomenon of cascade catalysis. However, there is now growing evidence that some of the enhanced effects observed in spatially organized enzyme complexes are due to changes brought about by the structure itself. Specifically, DNA-, protein- and charged scaffolds-introduce new chemical and physical features in the structure and create a microenvironment around the attached enzyme that is different from the whole . In the same way that microenvironmental engineering can improve individual enzymes' turnover, stability, and kinetics, they can also influence cascade catalysis .

In this work, we modeled the cascade between HK2 and G6PD and constructed the HK2-sfGFP-G6PD system by scaffolding a differently charged protein (supercharged sfGFP). The (+36)sfGFP attracted the negatively charged intermediate G6P to form a substrate channel by electrostatic effect, while the (-30)sfGFP inhibited the transfer of G6P. Such a structure affected the intermediates' diffusion, manifested as a change in transient time. Furthermore, as a result, the kinetics of the cascade was shown to be altered in the pseudo-Michael assay. However, when we delved into the kinetics by transient time analysis, we found that not only the transient time was affected after sfGFP modification, but also the initial rate of the cascade changed dramatically. This result implies that the increase in the cascade turnover rate could not be explained by the transient time alone; the change in the initial rate implied a change in the kinetics of the individual enzyme, which also affected the cascade reaction period. We further analyzed the kinetic changes of HK2 and G6PD after sfGFP modification. The results showed that sfGFP modification affected

the distribution of charged substrates around individual enzymes. Specifically, (+36) sfGFP modification helped G6P leave HK2 faster (k_{cat} increased) and reached G6PD faster ($K_{M,G6P}$ decreased); other charged substrates were also affected by local charge changes, such as ATP and $NADP^+$; in contrast, glucose was not charged, and both $k_{cat,app}$ and $K_{M,app}$ were almost unaffected. Also, (-30)sfGFP affects charged molecules and alters the kinetics of HK2 and G6PD.

To describe our interpretation of the cascade, we used the kinetic constants of HK2 and G6PD as parameters to model the cascade. We found that the model results agree well with the experimental results. We built two models (channeling and non-channeling) to fit and showed the *k*-values of HK2-sfGFP-G6PD subjected to different sfGFP modifications. Although the *k*-values were fitted with or without considering channeling, the error of the channeling model was not negligible. This result suggested that sfGFP was more likely to form a microenvironment for charged molecules to aggregate around the attached HK2 and G6PD than to form a substrate channel. Such an alteration directly affects the enzymatic kinetics of HK2 and G6PD, leading to changes in the overall cascade catalysis. Distinguishing enhancements caused by microenvironmental changes from substrate channels may be challenging. However, when we recognize that the microenvironment plays a key role, we can design controlled experiments that strengthen conclusions about substrate channels where reasonable, providing alternative explanations when necessary.

A deeper understanding of the interactions between the microenvironment, multienzyme structural dynamics, and substrate channels will also help develop a range of

new technologies. Synthetic cells, membrane-free organelles, and other systems that attempt to recapitulate cellular function will benefit from cascade design rules that address spatial organization and microenvironmental chemistry. Likewise, nanosized, co-permeable, or other chemical scaffolds for enzymes in physical structures will benefit. Substrate channels have certainly captured our attention and curiosity. This intriguing topic has also captured the attention and imagination of many, and it promises to inspire future researchers as these new applications mature. We hope that a basic understanding of the microenvironment will be as impressive as directly enhancing activity using scaffolds.

4.5 Materials and Methods

4.5.1 Computer method

4.5.1.1. Fit HK2 and G6PD kinetics before and after sfGFP modification.

The kinetic mechanisms of HK2 and G6PD are the rapid equilibrium random sequential (Random bi-bi) mechanism [24] and the steady-state ordered sequential (Order bi-bi) mechanism [25], respectively. Their Michaelis-Menten constants were calculated from nonlinear surface fitting by the python package SciPy 1.0 which was provided by Ralf Gommers et al. [26] and was run in python 3.8.0, and double checked by OriginPro (Version 2021b) with nonlinear curve fitting. The fitting algorithm uses the Levenberg-Marquardt algorithm. We obtained the initial rate of HK2 and G6PD at different substrate concentrations. The initial rate data were entered into the script after calculating the mean and variance. In the script, the fitting function used for the random bi-bi mechanism was the equation below provided by Kathryn M. et al. [26,27].

$$\text{initial Rate} = \frac{k_{\text{cat}} \times [glucose] \times [ATP]}{\alpha \times \left(K_{i,ATP} \times K_{i,glucose} + K_{i,ATP} \times [glucose] + K_{i,glucose} \times [ATP]\right) + [glucose] \times [ATP]}$$

The output data including turnover rate (k_{cat}), kinetic constants ($K_{\text{i.glucose}}$, $K_{\text{i,ATP}}$, α) are listed in table S4.4. The Michaelis-Menten constants and equilibrium binding constant of two substrates are regarded by the following [28]:

$$K_{M,glucose} = K_{i,glucose} \times \alpha; K_{M,ATP} = K_{i,ATP} \times \alpha$$

The fit function used for the order bi-bi mechanism was equation offered by our previous work [29] with following equation:

$$\text{Initial Rate} = \frac{k_{cat} \times [NADP^+] \times [G6P]}{k_{i,NADP^+} \times K_{M,G6P} + K_{M,G6P} \times [NADP^+] + K_{M,NADP^+} \times [G6P] + [NADP^+] \times [G6P]}$$

The output data include turnover rate (k_{cat}), Michaelis-Menten constants of two substrates ($K_{\text{M.NADP+}}$, $K_{\text{M.G6P}}$), and equilibrium binding constant of $NADP^+$ ($K_{\text{i.NADP+}}$) are listed in the table S4.5). The experimental data and the fitted model correlations were evaluated by the R score and implemented by the OriginLab or the corrcoef model from the python package NumPy, offered by Millman et al. [30].

4.5.1.2. Simulation model of HK2-sfGFP-G6PD based on the assembly enzymes' kinetics after sfGFP modification.

The model of HK2-sfGFP-G6PD and HK2/G6PD mix were built by the python package kinetics 1.4.1, provided by Harmer et al. [31], under python 3.8.0. The model schematic was shown in Figure S4.10. The rate law of the model used the parameters of

the kinetic constants of HK2 before and after modifications and G6PD before and after modifications, see list S4.1. The script was written as G6P produced by HK2 with Eq.1, and consumed by G6PD with Eq.2. The kinetics constant of HK2 and G6PD before and after sfGFP modification, and enzyme concentration (0.05 - 0.25 pmol/ul) used in experiment are set as the parameters to constrain the model. As the output, the change of NADPH and G6P concentration in 60 mins (360 time points) is monitored at different substrate concentration conditions. Following substrate concentrations are monitored: (1) glucose 50 μM, ATP 25 μM, $NADP^+$ 40 μM; (2) glucose 1000 μM, ATP 25 μM, $NADP^+$ 40 μM; (3) glucose 50 μM, ATP 500 μM, $NADP^+$ 40 μM; (4) glucose 50 μM, ATP 500 μM, $NADP^+$ 5 μM; (5) glucose 1000 μM, ATP 25 μM, NADP+ 5 μM; (6) glucose 1000 μM, ATP 500 μM, $NADP^+$ 5 μM.

4.5.1.3. Kinetics model of HK2-sfGFP-G6PD.

The model of HK2-sfGFP-G6PD and HK2/G6PD mix were built with the chemical notation and based on the reaction mechanism. The steady-state rate equation was derived by the King-Altman algorithm. Eventually, the final rate equation for each component was expressed in algebraic form and based on the rate constants. We then manipulate each group of rate constants (k1, k2, k3, etc.) to generate Michaelis constants.

Two models were built. The first model is the non-channeling model. In the non-channeling model, the HK2-sfGFP-G6PD complex is considered as a group (represented by E), which contains two active sites (HK2 and G6PD fractions). Since the HK2 kinetics are in accordance with random bi-bi mechanism, the HK2 fraction binds randomly to

Glucose (G) and ATP (T) and produces ADP (L) and G6P (M). G6PD conforms to the order bi-bi mechanism, the G6PD part needs to first bind to $NADP^+$ (N), then to G6P to form an enzyme complex, and to produce first 6PL (L) and then NADPH (P). The model draft is shown in Figure S4.8a. The key point of this model is that the reactions of the two active sites are independent of each other, and only G6P is used as a link. When G6P is present, the reaction can start with either HK2, G6PD, or both. Because there is no channeling parameter included, HK2/G6PD mix can be also fitted by this model.

The second model is the channeling model. In the channeling model, HK2-sfGFP-G6PD was considered as a unit (E). $NADP^+$, Glucose, and ATP randomly bind to the enzyme and form a complex, which then forms 6PL, ADP, and NADPH, where 6PL is always formed before NADPH is formed. G6P is not formed during the whole process because we assume a good channeling effect in this model, and G6P is not released into the environment. The model draft is shown in Figure S4.8b.

To simplify the calculation, the process of enzyme complex formation is irreversible when both Glucose and ATP are bound to the enzyme active site [32]. The reaction mechanism and kinetic constants for this process are listed in the separate documents.

4.5.2 Experimental Methods

SAFETY STATEMENT: please consult the appropriate Materials Data Safety Sheet (MSDS) and other safety information prior to using this chemical.

4.5.2.1. Chemicals

4-azido-L-phenylalanine (pAzF) was purchased from VWR. p-alkynyl-L-phenylalanine (pAkF) was purchased from MedChemExpress. Spectinomycin, sodium chloride, chloramphenicol, kanamycin, Luria-Bertani (LB) broth, 10X PBS buffer, Tris-Base, ethanol, pierce 660nm Protein Assay Reagent, isopropyl beta-D-1-thiogalactopyranoside (IPTG), Amicon Ultra-4 centrifugal Filter 10 kDa MWCO, Amicon Ultra-4 centrifugal Filter 50 kDa MWCO, Amicon Ultra-4 centrifugal Filter 100 kDa MWCO, SOC medium, and SOB medium were purchased from Thermo Fisher Scientific. NEBuider HiFi DNA Assembly Master Mix, T4 DNA ligase, and Q5 Site-directed mutagenesis Kit were purchased from New England Biolabs (NEB). DNA clean & Concentrator kit was purchased from Zymo Research. HisTrap HP, size exclusion chromatography (Superdex 200 Increase 10/300 GL), ammonium sulfate, copper (II) sulfate, sodium-L-ascorbate, tris(3-hydroxypropyl-triazolyl-methyl)amine (THPTA), ethylenediaminetetraacetic acid (EDTA), glucose-6-phosphate dehydrogenase (G6PD), glucose-6-phosphate (G6P), $NADP^+$, NADPH, glucose, M9 media, imidazole were purchased from Sigma-Aldrich. 0.22 μM syringe filters and 0.45 μM syringe filters were purchased from Corning. Bio-Scale Mini De-salting cartridges were purchased from Bio-rad Laboratories. Synthetic complete (SC) powder was purchased from Sunrise Science Products.

4.5.2.2. HK2, G6PD, and super-charged sfGFP cloning, expression, and purification

Plasmids encoding for (+36)sfGFP-SpyTag, (0)sfGFP-SpyTag, (-30)sfGFP-SpyTag, HK2, and G6PD-SpyCatcher were based on our previous report [14]. The genes used in this project were listed in List S4.2 and primers are listed in Table S4.6. The amber stop codon was introduced at the E131 site of sfGFP by site-directed mutagenesis. The DNA fragment encoding relative gene was cloned into a pET-28a(+) expression vector using the NEBuilder HiFi DNA assembly method. The assembled expression vector was transformed into BL21DE3 cells for protein expression. Briefly, chemically competent *E. coli* cells were thawed on ice for 5 mins, 2 μL of the chilled solution (~1 ng/ul DNA) was added to 80 μL of competent cells, and the solution was mixed by pipetting and placed on ice for 30 mins. The transformation mixture then was heat shocked for 30s at 42 °C and subsequently cooled on ice for 2 minutes. Room temperature SOC media (2% Vegetable Peptone, 0.5% Yeast Extract, 10 mM NaCl, 2.5 mM KCl, 10 mM $MgCl_2$, 10 mM $MgSO_4$, 20 mM glucose media contents) was added into the tube to reach a final volume of 1 mL, prior to incubation at 37 °C (220 rpm) for 60 mins. Finally, 100 μL cells were spread onto a 37 °C warmed selection plate and incubated overnight at 37 °C. A successfully transformed colony was picked and transferred to 250 mL of sterilized LB broth containing 50 μg/mL kanamycin in a 1 L shake flask. HK2, G6PD, and sfGFP expression were induced with 0.5 mM IPTG when the culture reached an OD_{600} = 0.6 (~ 1 h after inoculation and growth at 37 °C with 220 rpm shaking). Post induction cultures were moved to a 20 °C shaker incubator and expression continued for 48 h. All purification steps were carried out

at 0-4 °C. Cells were harvested by centrifugation at 5000 g for 10 minutes and resuspended in 100 mL PBS twice. After lysis by sonication (the 30 s on/90 s off, with a total of 5 min on time, all processed on ice), lysates were harvested by centrifugation at 15000 g for 30 mins. Soluble protein fractions were first purified by ammonium sulfate precipitation; samples were isolated from fractions collected containing 30%-60% ammonium sulfate. After precipitation, precipitated samples were resuspended in 1×PBS. All protein samples were filtered through a 0.22 μm syringe filter, and isolated by HisTrap column at HisTag wash buffer (1×PBS buffer, 10 mM imidazole, pH 7.4) and at HisTag elution buffer (1X PBS buffer, 500mM imidazole, pH 7.4). After isolation, sfGFP was filtered over a 10 kDa filter, and G6PD and HK2 were filtered over 50 kDa filter to concentrate the sample.

4.5.2.3. Incorporation, click-chemistry with pAzF and pAkF, and covalent interaction with SpyTag and SpyCatcher

The site-specific incorporation of the non-canonical amino acid (pAzF for HK2 and pAkF for sfGFP) were accomplished by first introducing an amber stop codon, TAG, into the desired incorporation site. Mutagenesis on the HK2 or sfGFP gene (expressed from the pET-28a(+) vector as described above) to accomplish this was conducted with a Q5® Site-Directed Mutagenesis Kit and associated protocols (NEB). HK2 expression with incorporated pAzF was accomplished by transforming both the pEVOL-pAzF plasmid [33], encoding a tRNA synthetase/tRNA pair specific to pAzF, and pET-28a(+)-HK2 into *E. coli* BL21-AI cells. To avoid photolysis of pAzF, all step were conducted under a red photographic light or in a dark room. Cells harboring plasmids were used to inoculate 250

mL of M9 media containing 2 g/L synthetic complete (SC) powder (Sunrise Science Products), 1 mM pAzF, 50 μg/mL kanamycin and 25 μg/mL chloramphenicol in a 1 L flask at 37 °C. sfGFP expression with incorporated pAkF was accomplished by transforming both the pULTRA-CNF plasmid [34], encoding a tRNA synthetase/tRNA pair specific to p-alkynyl-phenylalanine (pAkF) [35], and pET-28a(+)-sfGFP into *E. coli* BL21DE3 cells. Cells harboring plasmids were used to inoculate 250 mL of LB media containing 1mM pAkF, 50 μg/mL kanamycin and 50 μg/mL spectinomycin in a 1 L flask at 37 °C. When cells reached an OD_{600} = 0.6, HK2 expression was induced with 0.5 mM IPTG, while expression from pEVOL-pAzF was induced with 0.2% (v/v%) arabinose, while sfGFP expression and expression from pULTRA-CNF was induced with 2mM IPTG. Post induction cultures were moved to a 20 °C, 250 rpm shaker incubator, and expression continued for 48 hours. All subsequent purification steps were carried out at ~4 °C unless noted otherwise. Cells were harvested by centrifugation at 5000 g for 10 min and resuspended in 100 mL 1×PBS buffer (twice). After sonication, clarified lysates were produced by centrifugation at 15000g for 30 mins and protein samples were purified the lysates as described in the previous section. For azide-alkyne cycloaddition, sfGFP(pAkF) was first mixed with 2 equivalents of HK2(pAzF). The protein sample mix was then added with 5 equivalents of pre-cold cycloaddition catalyst (100 mM $CuSO_4$ is incubated with 200 mM THPTA ligand in water for 10 min at 4 °C), 10 equivalents of sodium ascorbate (Cu(II) reducing agent). Vortex with 5 rpm at room temperature for 1 h. To stop the reaction, 5 mL 0.1g/mL EDTA is added into the sample. To remove extra HK2(pAzF) and salt, the sample filtered over a 100 kDa filter to concentrate the sample and then buffer-changed to

Tris buffer (50 mM Tris, pH 8.0) using size exclusion chromatography. To form SpyTag-SpyCatcher covalent interaction, purified HK2-sfGFP was mixed with 2 equivalents of G6PD-SpyCatcher overnight at 4 °C. Extra G6PD-SpyCatcher was removed by filtered over a 100 kDa filter.

4.5.2.4. Protein concentration determination

The concentration of protein samples was determined by Pierce 660 nm protein assay. Method is offered by Babu et al. [36] with small modifications. Briefly, BSA standard replicates (2.5, 5, 12.5, 25, 50, 75, 100, 150, and 200 μg) were first diluted in the 0.1 mL saline, and following added with 1.5 mL assay reagent. After incubating at room temperature (22 °C) in dark for 5 min, the absorbance of all the samples and controls were measured at 660 nm. The standard curve was shown in Figure S4.11. 0.1 mL of each replicate of protein samples were first buffer-transferred in 0.1 mL saline and following prepared with 1.5 mL of the protein assay reagent and covered to avoid the light. After 5 minutes of incubation at room temperature, all samples were detected with the spectrophotometer at 660 nm.

4.5.2.5. NADPH concentration determination

The concentration of NADPH solutions was checked by absorbance at 340 nm. The NADPH supply was diluted to 200 μM with a total volume of 1 mL using a kinetic performance buffer (50 mM Tris, 10 mM $MgCl_2$, pH 8.0). Additional dilutions (160 μM, 80 μM, 40 μM, 20 μM, 10 μM, 5 μM, 1 μM) and the control (0 μM) were then produced using kinetic performance buffers. The duplicates of 4 contained 200 ultimatums of each dilution into microplates. Absorption

measurements were made with a 340 nm absorbance filter with a 10 nm bandwidth utilizing a microplate reader, and the background signal was eliminated based on the control absorbance. The plot of NADPH absorbance with different NADPH concentration was plotted in Figure S4.12 with linear fitting by Graph Prism 9.

4.5.2.6. HK2, G6PD, and HK2-sfGFP-G6PD complex kinetics analysis

All kinetic assays were conducted in 96-well microtiter plates at room temperature with absorbance monitored using a Synergy Neo2 multi-mode microplate reader (BioTek). Kinetics was performed in kinetic buffer (50 mM Tris, 10 mM $MgCl_2$, pH 8.0). The HK2 kinetic assay was carried out in a total 200 µL reaction buffer, with 20 pmol recombinant HK2, 200 umol commercial G6PD as co-enzyme, 1 mM $NADP^+$, and substrates at each condition (glucose with final concentration: 0.05, 0.125, 0.25, 0.5, 1, and 2 mM, and ATP with final concentration 0.025, 0.05, 0.125, 0.25, 0.5, and 1 mM, with 6×6 conditions). For the G6PD, the kinetic assay was carried out in total 200 µL reactions buffer, 20 pmol recombinant G6PD, and substrates (G6P with final concentration: 25, 50, 100, 200, 400, and 800 uM, and $NADP^+$ with final concentration: 1, 2.5, 5, 10, 20, and 40 µM, with 6×6 conditions). For the HK2-sfGFP-G6PD and HK2/G6PD mix, kinetic assay was carried out in 200 µL reactions buffer, 50 pmol HK2-sfGFP-G6PD, or HK2 and G6PD mix (50 pmol : 50 pmol), and substrates (glucose with final concentration: 0.05, 0.125, 0.25, 0.5, 1, and 2 mM, ATP with final concentration 0.025, 0.05, 0.125, 0.25, 0.5, and 1 mM, and $NADP^+$ with final concentration: 1, 2.5, 5, 10, 20, and 40 uM, with 6×6×6 conditions). All activity was monitored by measuring the absorbance of the NADPH at 340 nm. The extinction

coefficient of NADPH at 340 nm under reaction conditions was obtained as NADPH concentration determination section with the extinction coefficient as 6657 $cm^{-1}M^{-1}$, calculated based on Beer's law with pathlength as 0.6 cm.

4.5.3 Statistics and reproducibility

Relevant statistical information for each experiment were included in the associated figure and table legends. The ordinary one-way ANOVA was performed in GraphPad Prism version 9 to determine one parameter under a certain condition by multiple comparisons.

The fitting curves for the kinetic assays of individual enzymes (HK2 and G6PD) before and after sfGFP modifications were performed by nonlinear curve fitting in the originlab software. The fitting algorithm was the Levenberg-Marquardt algorithm. The fitting curves for the kinetic assays of HK2-sfGFP-G6PD were performed by the Dynafit software with King-Altman method and based on least-squares minimization. The standard residues were calculated by the written python script named standard_residue.py, with the threshold as 2. The linear part of experiment data and simulation data were assumed with non-Gaussian distribution, and their nonparametric spearman correlation and r score were calculated by GraphPad Prism version 9. All parameters interpreted with a 95% confidence interval.

Experiments with representative figures conducted in this study were repeated multiple times independently with similar results. SDS-PAGE was performed three times

on different days. Each kinetic measurement was performed three times and repeated twice on different days.

4.6 Acknowledgements

The authors thank the Army Research Office MURI grant W911NF1410263 for funding.

4.7 Reference

1. Wheeldon, I. *et al.* Substrate channelling as an approach to cascade reactions. *Nature Chemistry* vol. 8 299–309 (2016).

2. Ellis, G. A. *et al.* Artificial Multienzyme Scaffolds: Pursuing in Vitro Substrate Channeling with an Overview of Current Progress. *ACS Catalysis* vol. 9 10812–10869 (2019).

3. Schmid-Dannert, C. & López-Gallego, F. Advances and opportunities for the design of self-sufficient and spatially organized cell-free biocatalytic systems. *Current Opinion in Chemical Biology* vol. 49 97–104 (2019).

4. Wu, X. M., Gutfreund, H., Lakatos, S. & Chock, P. B. Substrate channeling in glycolysis: a phantom phenomenon. *Proceedings of the National Academy of Sciences* vol. 88 497–501 (1991).

5. Zhang, Y., Tsitkov, S. & Hess, H. Proximity does not contribute to activity enhancement in the glucose oxidase–horseradish peroxidase cascade. *Nature Communications* vol. 7 (2016).

6. Poshyvailo, L., von Lieres, E. & Kondrat, S. Does metabolite channeling accelerate enzyme-catalyzed cascade reactions? *PLoS One* **12**, e0172673 (2017).

7. Schneider, T. R. *et al.* Loop closure and intersubunit communication in tryptophan synthase. *Biochemistry* **37**, 5394–5406 (1998).

8. Fu, J. *et al.* Multi-enzyme complexes on DNA scaffolds capable of substrate channelling with an artificial swinging arm. *Nat. Nanotechnol.* **9**, 531–536 (2014).

9. Electrostatic Channeling in the Bifunctional Enzyme Dihydrofolate Reductase-thymidylate Synthase. *J. Mol. Biol.* **262**, 370–374 (1996).

10. Eun, C., Kekenes-Huskey, P. M., Metzger, V. T. & Andrew McCammon, J. A model study of sequential enzyme reactions and electrostatic channeling. *J. Chem. Phys.* **140**, 105101 (2014).

11. Bulutoglu, B., Garcia, K. E., Wu, F., Minteer, S. D. & Banta, S. Direct Evidence for Metabolon Formation and Substrate Channeling in Recombinant TCA Cycle Enzymes. *ACS Chem. Biol.* **11**, 2847–2853 (2016).

12. Knighton, D. R. *et al.* Structure of and kinetic channelling in bifunctional dihydrofolate reductase–thymidylate synthase. *Nature Structural Biology* vol. 1 186–194 (1994).

13. Xie, Y. & Calabrese Barton, S. Infrequent metadynamics study of rare-event electrostatic channeling. *Phys. Chem. Chem. Phys.* **23**, 13381–13388 (2021).

14. Abdallah, W., Chirino, V., Wheeldon, I. & Banta, S. Catalysis of Thermostable Alcohol Dehydrogenase Improved by Engineering the Microenvironment through Fusion with Supercharged Proteins. *Chembiochem* **20**, 1827–1837 (2019).

15. Zhang, Y. & Hess, H. Toward Rational Design of High-efficiency Enzyme Cascades. *ACS Catalysis* vol. 7 6018–6027 (2017).

16. Microenvironmental effects can masquerade as substrate channelling in cascade biocatalysis. *Curr. Opin. Biotechnol.* **73**, 233–239 (2022).

17. Liu, Y. *et al.* Cascade kinetics of an artificial metabolon by molecular dynamics and kinetic Monte Carlo. *ACS Catal.* **8**, 7719–7726 (2018).

18. Ovádi, J. & Saks, V. On the origin of intracellular compartmentation and organized metabolic systems. *Mol. Cell. Biochem.* **256-257**, 5–12 (2004).

19. Touw, W. G. & Vriend, G. BDB: Databank of PDB files with consistent B-factors. *Protein Eng. Des. Sel.* **27**, 457–462 (2014).

20. Aronson, D. E., Costantini, L. M. & Snapp, E. L. Superfolder GFP is Fluorescent in Oxidizing Environments when Targeted via the Sec Translocon. *Traffic* **12**, 543 (2011).

21. Yadav, G. D. & Magadum, D. B. Kinetic Modelling of Enzyme Catalyzed Biotransformation Involving Activations and Inhibitions. *Enzyme Inhibitors and Activators* (2017) doi:10.5772/67692.

22. Liu, Y., Hickey, D. P., Minteer, S. D., Dickson, A. & Calabrese Barton, S. Markov-State Transition Path Analysis of Electrostatic Channeling. *J. Phys. Chem. C Nanomater. Interfaces* **123**, 15284–15292 (2019).

23. Lang, X., Hong, X., Baker, C. A., Otto, T. C. & Wheeldon, I. Molecular binding scaffolds increase local substrate concentration enhancing the enzymatic hydrolysis of VX nerve agent. *Biotechnol. Bioeng.* **117**, 1970–1978 (2020).

24. Wilson, J. E. Hexokinases. in *Reviews of Physiology, Biochemistry and Pharmacology, Volume 126* 65–198 (Springer, Berlin, Heidelberg, 1995).

25. Glucose 6-phosphate dehydrogenase of human blood platelets: Kinetics and regulatory properties. *Arch. Biochem. Biophys.* **162**, 186–193 (1974).

26. Virtanen, P. *et al.* SciPy 1.0: fundamental algorithms for scientific computing in Python. *Nat. Methods* **17**, 261–272 (2020).

27. A rapid equilibrium random sequential bi-bi mechanism for human placental glutathione S-transferase. *Biochimica et Biophysica Acta (BBA) - Protein Structure and Molecular Enzymology* **998**, 7–13 (1989).

28. Fisher, J. R. Enzyme Kinetics Enzyme Kinetics: Behavior and Analysis of Rapid Equilibrium and Steady-State Enzyme Systems Irwin H. Segel. *BioScience* vol. 26 210–212 (1976).

29. A Chimeric Fusion Protein Engineered with Disparate Functionalities—Enzymatic Activity and Self–assembly. *J. Mol. Biol.* **392**, 129–142 (2009).

30. Harris, C. R. *et al.* Array programming with NumPy. *Nature* **585**, 357–362 (2020).

31. Finnigan, W. *et al.* Engineering a Seven Enzyme Biotransformation using Mathematical Modelling and Characterized Enzyme Parts. *ChemCatChem* **11**, 3474–3489 (2019).

32. Kuzmič, P. DynaFit--a software package for enzymology. *Methods Enzymol.* **467**, (2009).

33. Chin, J. W. *et al.* Addition of p-azido-L-phenylalanine to the genetic code of Escherichia coli. *J. Am. Chem. Soc.* **124**, 9026–9027 (2002).

34. Schultz, K. C. *et al.* A genetically encoded infrared probe. *J. Am. Chem. Soc.* **128**, 13984–13985 (2006).

35. Young, D. D. *et al.* An evolved aminoacyl-tRNA synthetase with atypical polysubstrate specificity. *Biochemistry* **50**, 1894–1900 (2011).

36. Antharavally, B. S., Mallia, K. A., Rangaraj, P., Haney, P. & Bell, P. A. Quantitation of proteins using a dye-metal-based colorimetric protein assay. *Anal. Biochem.* **385**, (2009).

4.8 Figures and Tables

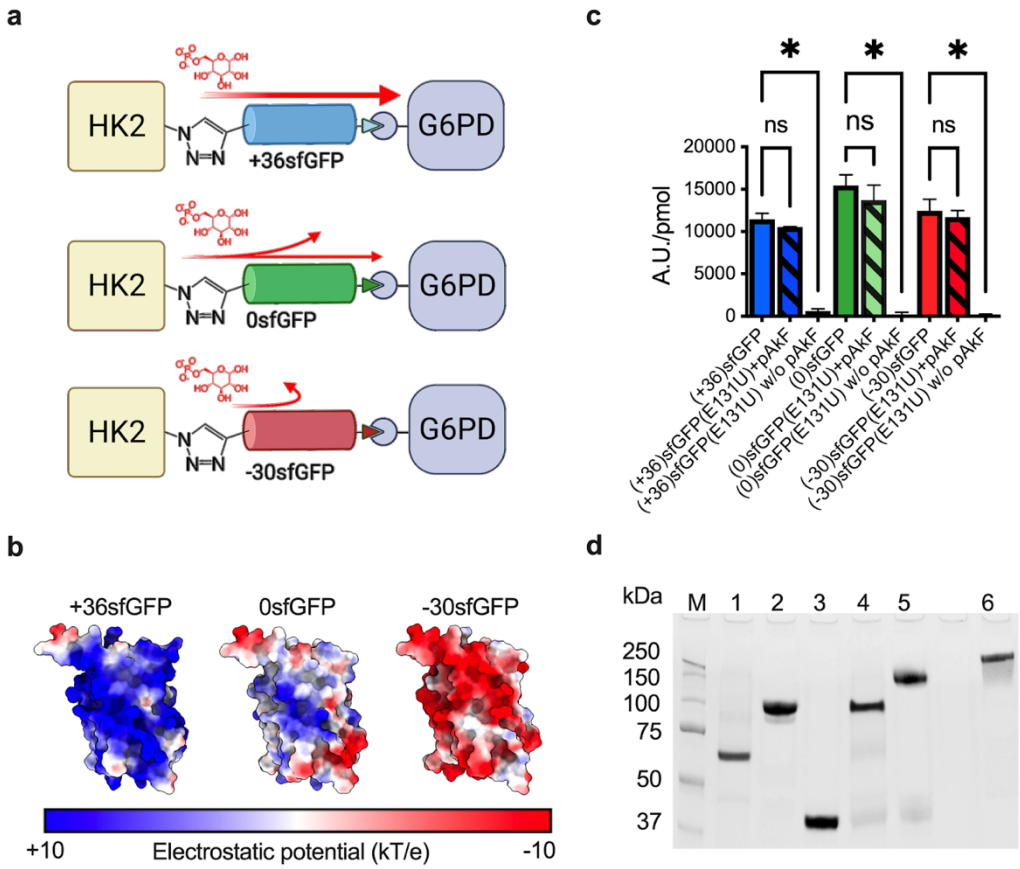

Figure 4.1 The HK2-sfGFP-G6PD complex is synthesized. (a) A schematic representation of the structure of HK2-sfGFP-G6PD is shown. The chemical structures of azide-alkyne cycloaddition represent the linkage of HK2 and sfGFP. SpyTag (triangle) and SpyCatcher (pacman) form a covalent bond that connects sfGFP to G6PD. The red arrow represents the predicted molecular flow of G6P. (b) sfGFP with varying surface charges (+36, 0, -30). (c) The fluorescence signal of sfGFP with and without pAkF, normalized based on the amount of sfGFP. Statistical significance is calculated by the ordinary one-way ANOVA and is in comparison to HK2/G6PD mixed together. "ns" indicates a p value > 0.05, "*" indicates $p \leq 0.05$. (d) SDS-PAGE analysis of HK2-sfGFP-G6PD synthesis with (+36)sfGFP as an example. M for Marker, L1 for G6PD, L2 for HK2, L3 for sfGFP, L4 for G6PD-sfGFP, L5 for HK2-sfGFP, L6 for HK2-sfGFP-G6PD.

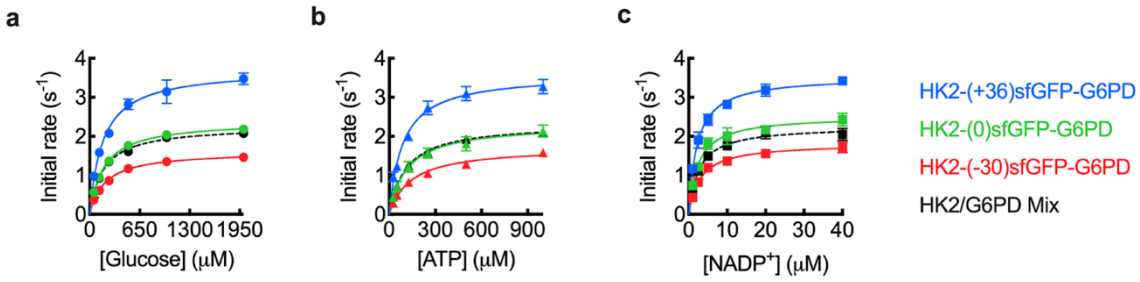

Figure 4.2 The effect of (+36)sfGFP, (0)sfGFP, and (-30)sfGFP on HK2-sfGFP-G6PD cascade. Kinetics assay of HK2-sfGFP-G6PD performed under the following conditions: (a) glucose concentration was varied while ATP and $NADP^+$ were saturated. (b) ATP concentration was varied while glucose and $NADP^+$ were saturated. (c) $NADP^+$ concentration was varied while glucose and ATP were saturated. HK2 and G6PD (equimolar) mix is shown as the control.

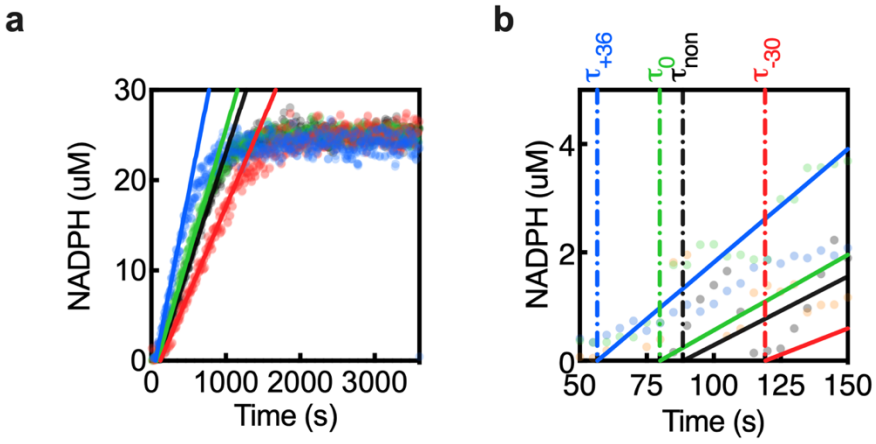

Figure 4.3 Transition time (τ) analysis of the HK2 and G6PD cascades at 1000 µM glucose, 25 µM ATP, and 40 µM $NADP^+$. (a) Changes in NADPH over time before and after sfGFP modification in the HK2-G6PD cascade reaction. The points represent experimental data obtained in the time curve, where absorption is converted to NADPH (see the method part, NADPH concentration determination). A solid line was drawn to represent the linear range of the time curve. (b) An inset of the time curve shows transition time. The transition time is the point at which the fitted line in panel (a) intersects the X-axis and is indicated by the dashed line. The figure depicts four sets of experiments. HK2-(+36)sfGFP-G6PD (blue), HK2-(0)sfGFP-G6PD (green), HK2-(-30)sfGFP-G6PD (red), and mixed HK2/G6PD (black).

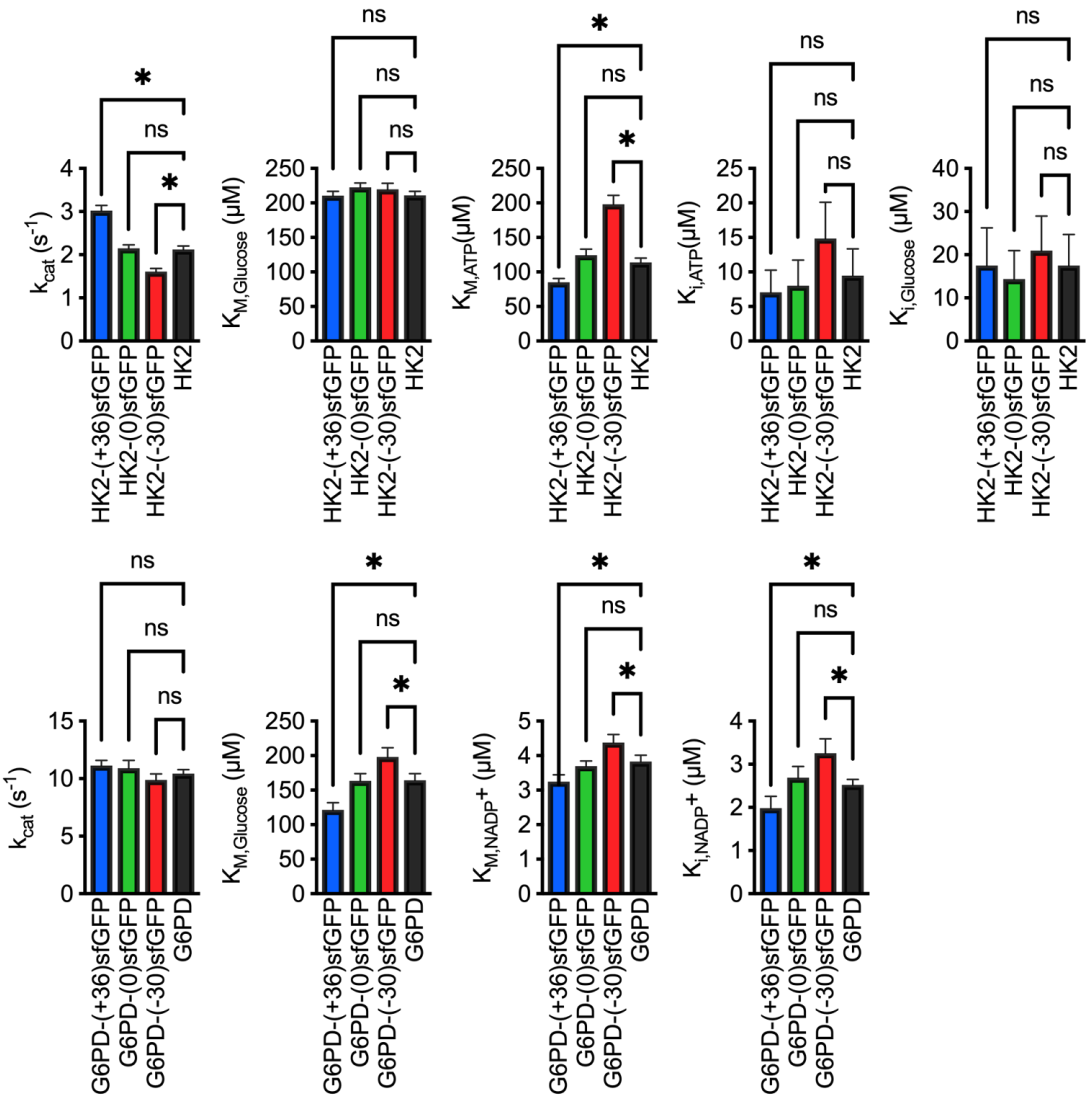

Figure 4.4 The change of k_{cat}, K_M, and K_i of HK2 and G6PD before and after sfGFP modification. The statistical significance calculated by the ordinary one-way ANOVA, and in comparison, to HK2 and G6PD in the absence of sfGFP modification is stated with "ns" indicating a p value >0.05, * is $p \leq 0.05$. Figure S4.4 depicts the 2-dimensional fitting curve.

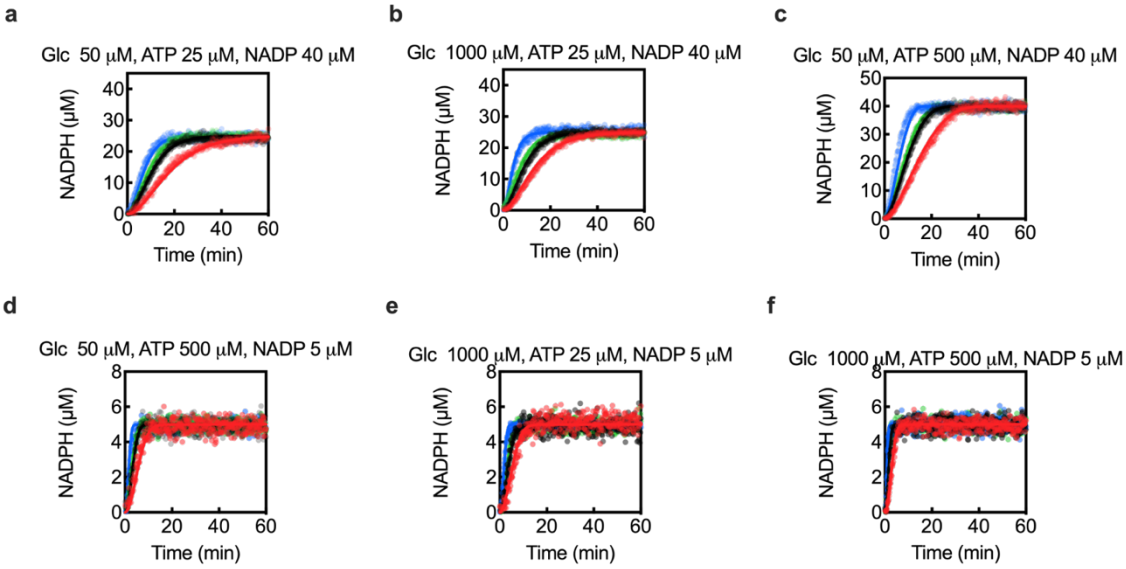

Figure 4.5 Data from simulation versus data from experiments. The time curve was used to generate the experiments, and the absorbance was converted to NADPH concentration using Beer's Law. A dot represents each piece of experimental data. The simulated NADPH data are shown as solid lines. On the left Y-axis, simulated NADPH data are plotted. The concentrations of six different substrates (a-f) were recorded and listed above the figure. Blue represents the data for HK2-(+36)sfGFP-G6PD. Green represents HK2-(0)sfGFP-G6PD. The HK2-(-30)sfGFP-G6PD is depicted in red, while the HK2/G6PD Mix is depicted in black.

Table 4.1 Kinetic parameters of HK2/G6PD and HK2-sfGFP-G6PD. Data are mean ± s.d. Statistical significance is calculated by the ordinary one-way ANOVA in comparison to HK2/G6PD mix. "ns" indicates a p value > 0.05, * indicates p ≤ 0.05.

	glucose				ATP				$NADP^+$			
	$k_{cat,app}(s^{-1})$		$K_{M,app}(\mu M)$		$k_{cat,app}(s^{-1})$		$K_{M,app}(\mu M)$		$k_{cat,app}(s^{-1})$		$K_{M,app}(\mu M)$	
HK2-(+36)sfGFP-G6PD	3.73±0.21	*	172.43±34.69	ns	3.60±0.21	*	75.69±10.63	*	3.53±0.14	*	2.16±0.06	*
HK2-(0)sfGFP-G6PD	2.40±0.09	ns	184.40±24.16	ns	2.32±0.19	ns	116.93±11.45	ns	2.53±0.15	ns	2.52±0.17	ns
HK2-(-30)sfGFP-G6PD	1.61±0.08	*	200.67±36.39	ns	1.73±0.11	*	147.13±15.77	*	1.82±0.09	*	3.01±0.14	*
HK2/G6PD Mix	2.26±0.12		176.37±34.29		2.33±0.07		110.77±8.81		2.26±0.12		2.54±0.09	

Table 4.2 Transition Time of HK2/G6PD mixed and HK2-sfGFP-G6PD. Data are mean ± s.d. Statistical significance is calculated by the ordinary one-way ANOVA, and in comparison, to HK2/G6PD mixed. "ns" indicates a p value > 0.05, * indicates $p \leq 0.05$.

	Transition Time (s)		Initial Rate (s^{-1})	
HK2-(+36)sfGFP-G6PD	46.93±4.28	*	0.68±0.07	*
HK2-(0)sfGFP-G6PD	96.31±8.82	ns	0.44±0.03	ns
HK2-(-30)sfGFP-G6PD	197.42±13.8	*	0.29±0.01	*
HK2/G6PD Mix	116.10±9.65		0.45±0.05	

Table 4.3 Kinetic parameters of HK2 and HK2-sfGFP. Data are mean ± s.d. Statistical significance calculated by the ordinary one-way ANOVA in comparison to HK2 in the absence of sfGFP modification. "ns" indicates a p value > 0.05, * indicates $p \leq 0.05$.

	$k_{cat}(s^{-1})$		$K_{M,glucose}(\mu M)$		$K_{M,ATP}(\mu M)$		$K_{i,glucose}(\mu M)$		$K_{i,ATP}(\mu M)$	
HK2-(+36)sfGFP	3.02±0.12	*	210.76±16.04	ns	85.21±2.55	*	17.47±8.13	ns	7.06±3.22	ns
HK2-(0)sfGFP	2.15±0.08	ns	222.84±12.22	ns	124.55±3.43	ns	14.36±6.63	ns	8.03±3.71	ns
HK2-(-30)sfGFP	1.61±0.07	*	219.99±21.62	ns	197.77±7.04	*	20.96±8.02	ns	14.84±5.28	ns
HK2	2.12±0.08		210.86±16.13		113.89±3.28		17.53±7.16		9.47±3.87	

Table 4.4 Kinetic parameters of G6PD and G6PD-sfGFP. Data are mean ± s.d. Statistical significance is calculated by One-way ANOVA, and in comparison, to G6PD in the absence of sfGFP modification. "ns" indicates a p value > 0.05, * indicates p ≤ 0.05.

	$k_{cat}(s^{-1})$		$K_{M,NADP}(\mu M)$		$K_{M,G6P}(\mu M)$		$K_{i,NADP}(\mu M)$	
G6PD-(+36)sfGFP	11.14±0.45	ns	3.25±0.20	*	121.47±10.37	*	1.98±0.28	*
G6PD-(0)sfGFP	10.91±0.67	ns	3.69±0.15	ns	163.50±10.64	ns	2.68±0.26	ns
G6PD-(-30)sfGFP	9.88±0.53	ns	4.28±0.23	*	191.93±14.37	*	3.26±0.33	*
G6PD	10.43±0.37		3.83±0.18		165.50±11.55		2.52±0.13	

4.9 Supporting information

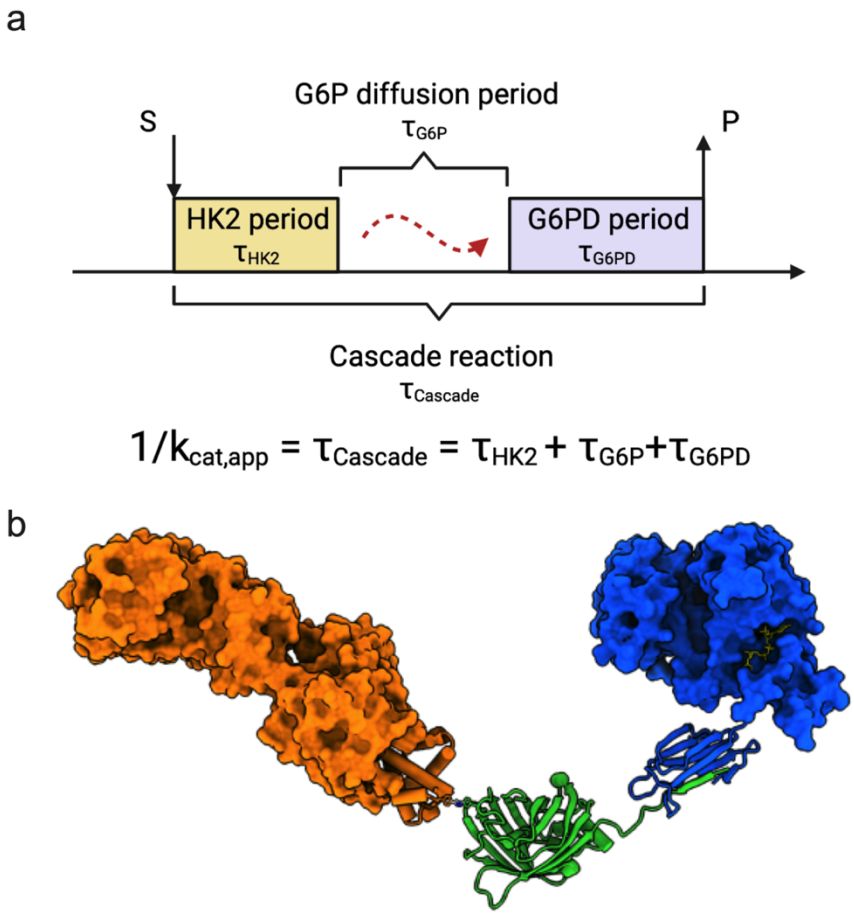

Figure S 4.1 The schematic diagram of the HK2-sfGFP-G6PD cascade. (a) The cascade period consists of the HK2 production, G6P diffusion, and G6PD consumption. (b) The schematic diagram of HK2-sfGFP-G6PD structure. HK2 is stained orange. G6PD is fused with a SpyCatcher and is stained blue. The active site of G6PD has NADP and is stained yellow. sfGFP fusing with SpyTag is stained green and has a covalent bond with SpyCatcher of G6PD.

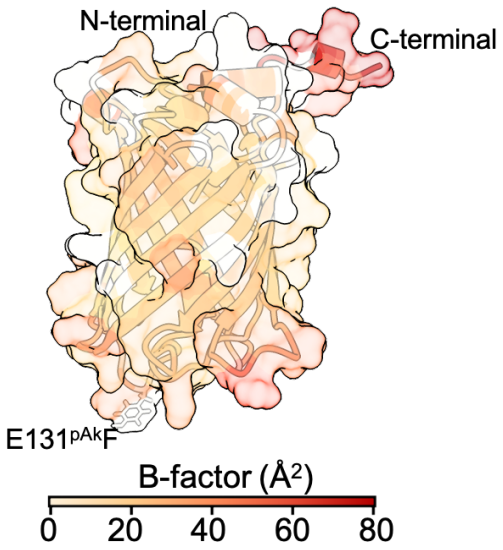

Figure S 4.2 The surface displacement of the atomic positions from an average value (b-factor) of (+36)sfGFP colors with the depth of red. Site E131 is mutated as pAkF, shown as stick, and labeled. The N-terminal and C-terminal are labeled next to the structure.

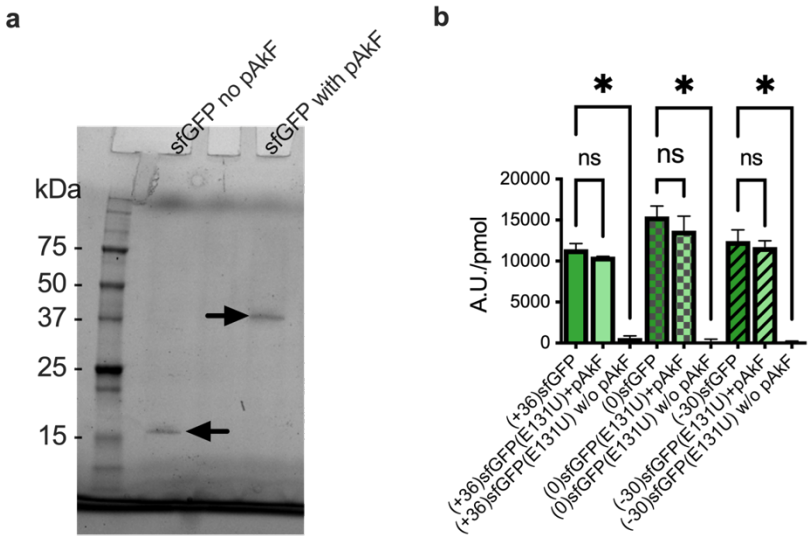

Figure S 4.3 The sfGFP incorporation with and without pAkF. (a) The SDS page of sfGFP without, and with pAkF. The band is marked with an arrow. (b) The fluorescent signal of different charged sfGFP with and without pAkF. "ns" indicates a p value > 0.05, * indicates $p \leq 0.05$.

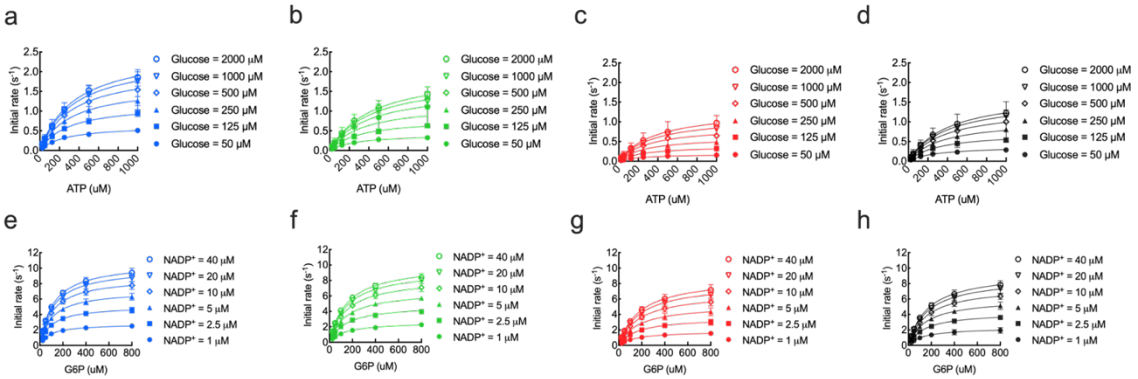

Figure S 4.4 2-D Kinetic assay of HK2 and G6PD before and after sfGFP modification. Dot represents the experiment data. Light blue surface is the fitting. The kinetics of HK2 and HK2-sfGFP are fitted by the Rapid equilibrium random sequential mechanism model. **(a)** HK2-(+36)sfGFP. **(b)** HK2-(0)sfGFP. **(c)** HK2-(-30)sfGFP. **(d)** HK2. The kinetics of G6PD and G6PD-sfGFP are fitted by the Steady state ordered sequential mechanism. **(e)** G6PD-(+36)sfGFP. **(f)** G6PD-(0)sfGFP. **(g)** G6PD-(-30)sfGFP. **(h)** G6PD.

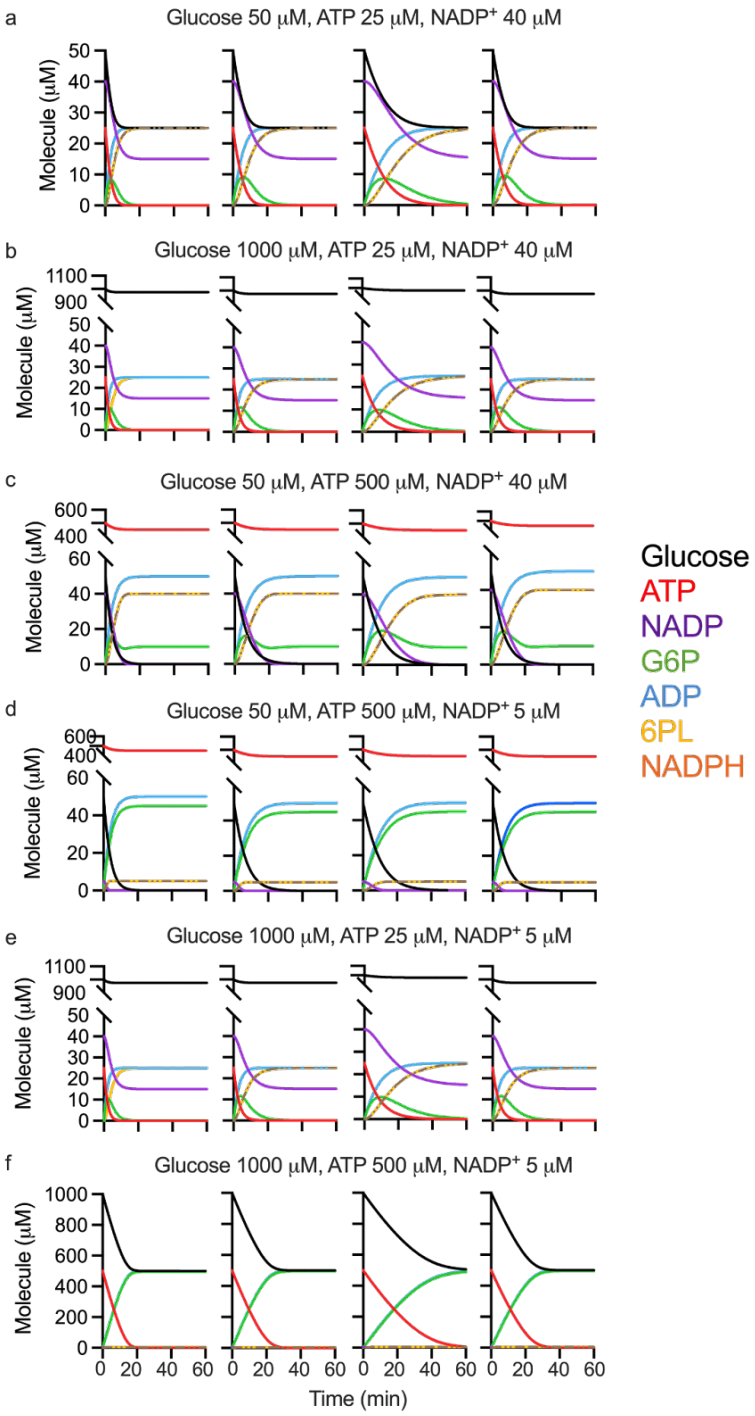

Figure S 4.5 The model of HK2/G6PD cascades before and after sfGFP modification at different substrate conditions.

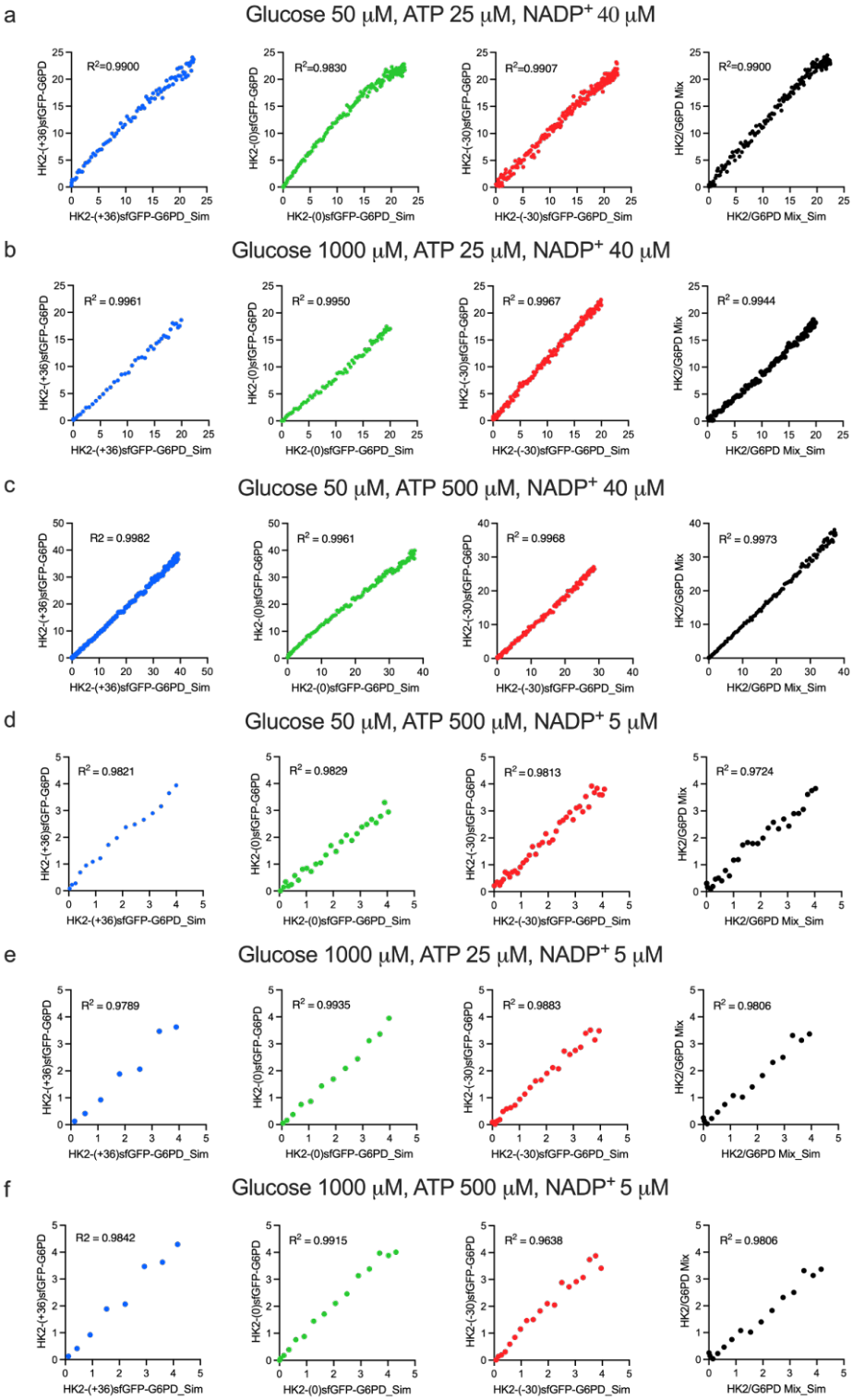

Figure S 4.6 The correlation of linear stage from simulation data and experiment data at six different substrate concentrations, with p<0.001.

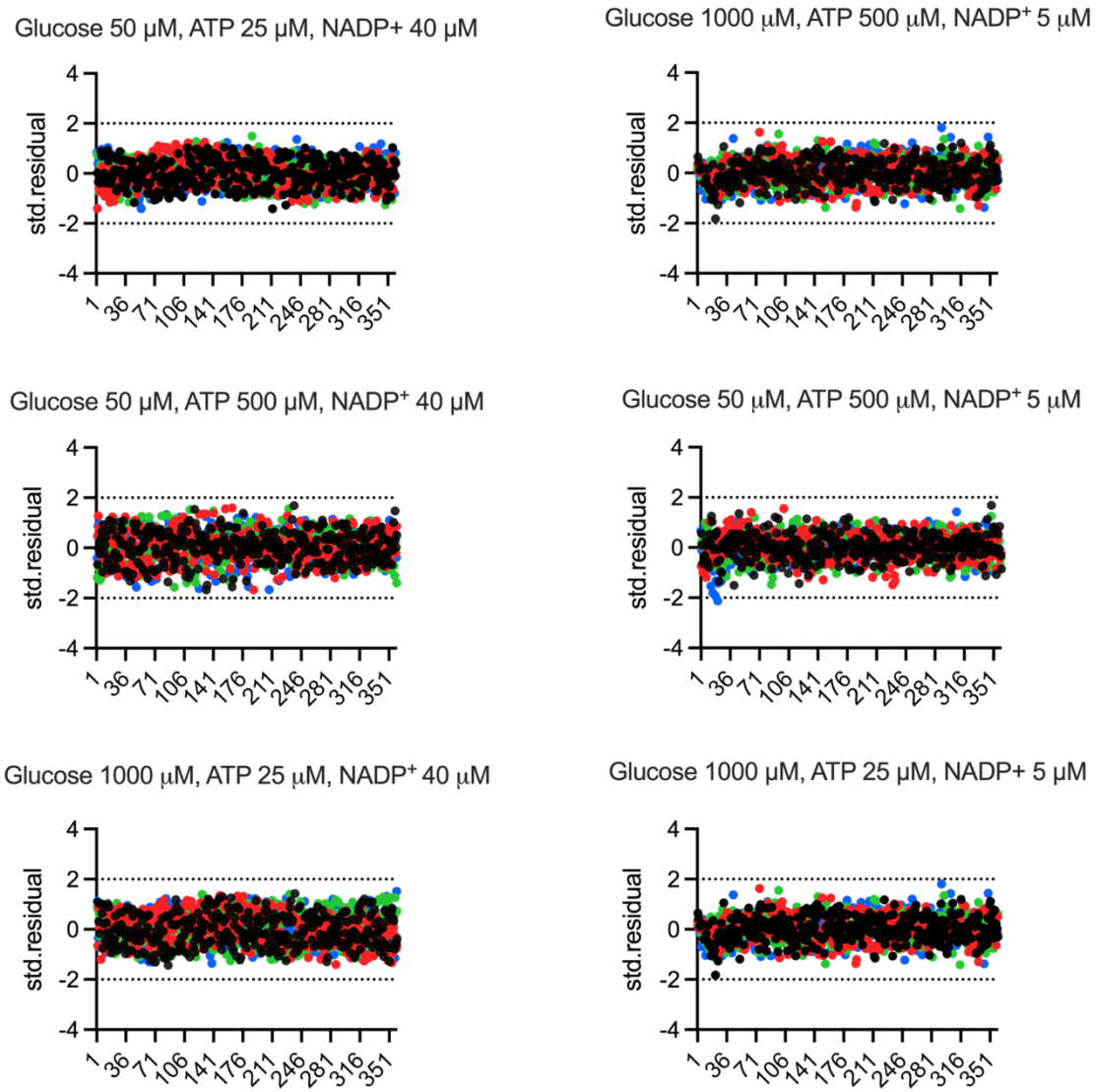

Figure S 4.7 The standard residual plot of NADPH from simulation and experiment. The standard residuals were on the vertical axis. Each residual was calculated from simulation and experiment. The independent data was on the horizontal axis. HK2-(+36)sfGFP-G6PD is indicated by blue, red is indicated by HK2-(-30)sfGFP-G6PD, and green is indicated by HK2-(0)sfGFP-G6PD. The HK2/G6PD Mix is shown in black as a control.

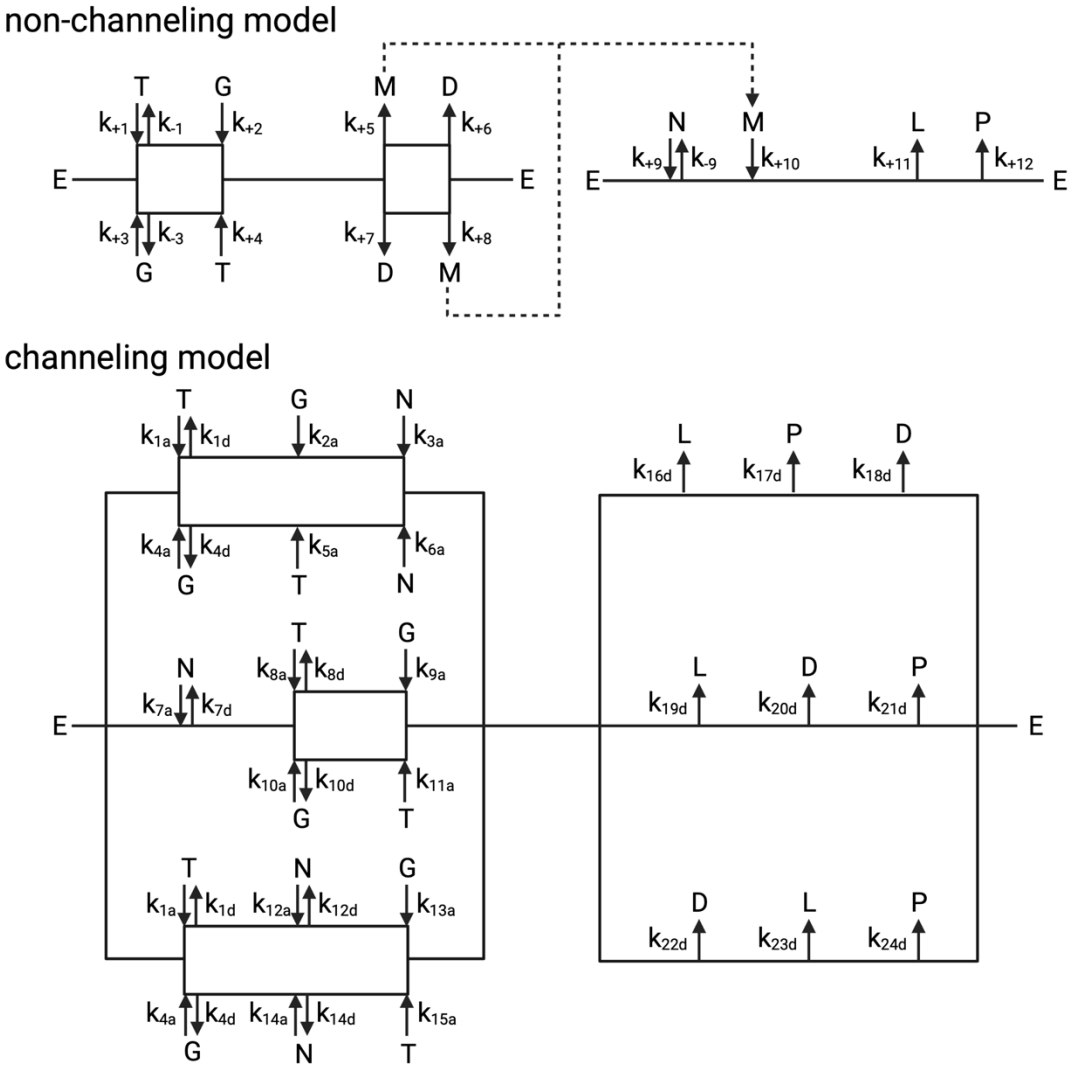

Figure S 4.8 The Schematic diagram of non-channeling model and channeling model. E is HK2-G6PD cascade, G is glucose, T is ATP, M is G6P, D is ADP, L is 6PL, P is NADPH, N is $NADP^+$, D is ADP. The k values are labeled next to the arrow.

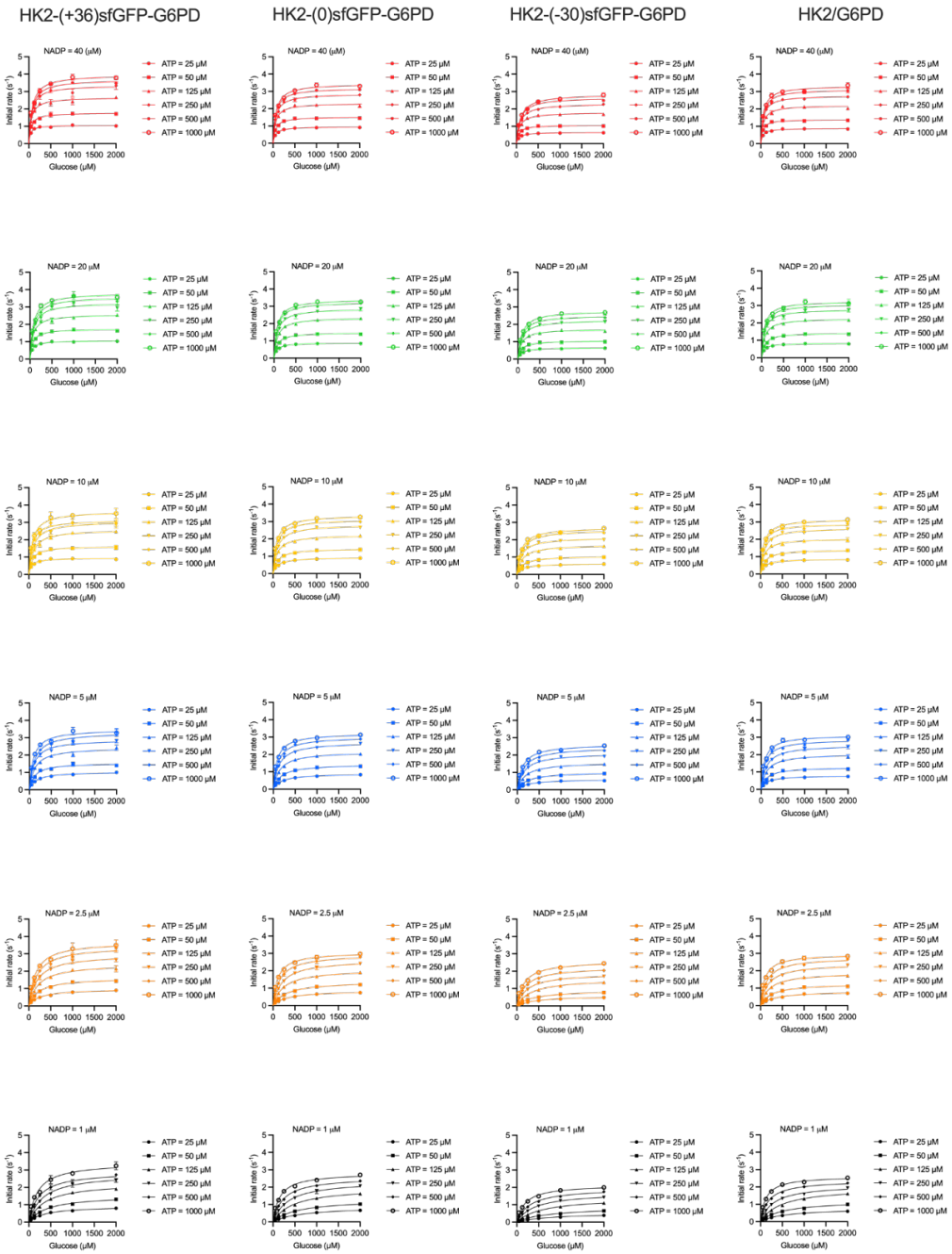

Figure S 4.9 The kinetic assay fitted by the non-channeling model. From left to right are sets of data for HK2 and G6PD modified by (+36)sfGFP, (0)sfGFP, and (-30)sfGFP, or no modification. The substrate concentrations are labeled as in legends and titles.

Table S 4.1 k-value of non-channeling model.

k value	non	(+36)sfGFP	(0)sfGFP	(-30)sfGFP
k+1	0.89±0.12	0.81±0.13	0.89±0.11	1.09±0.16
k-1	14.65±2.42	15.00±2.39	14.89±2.55	13.10±2.22
k+2	0.61±0.09	0.72±0.10	0.56±0.08	0.33±0.06
k+3	0.48±0.09	0.71±0.10	0.48±0.08	0.36±0.06
k-3	3.56±0.59	3.73±0.64	3.70±0.62	3.21±0.50
k+4	0.50±0.06	0.64±0.11	0.53±0.07	0.34±0.05
k+5	6.13±0.79	7.28±1.25	6.79±0.86	5.86±0.99
k+6	5.96±0.89	7.48±1.01	6.58±0.98	5.15±0.62
k+7	6.25±1.06	7.27±1.13	6.28±0.78	5.31±0.93
k+8	5.75±0.91	6.44±0.99	5.80±0.95	4.66±0.81
k+9	3.74±0.53	2.86±0.48	4.00±0.70	5.14±0.79
k-9	13.59±2.45	12.56±1.66	14.89±2.06	13.29±2.05
k+10	0.80±0.11	0.97±0.17	0.80±0.14	0.58±0.09
k+11	15.33±1.84	17.30±2.93	16.05±2.65	13.69±2.14
k+12	15.17±2.28	17.02±2.20	16.27±2.72	14.13±2.50

Data are mean ± s.d.
Rate law of the non-channeling model is attached as a non-channeling file.
“non” indicates HK2/G6PD mix, the name of charged sfGFP indicates the charged of sfGFP modified the HK2-G6PD cascade.
All data starts at 1.

Table S 4.2 k-value of channeling model

k-value	(+36)sfGFP		(0)sfGFP		(-30)sfGFP		non	
	mean	s.d.	mean	s.d.	mean	s.d.	mean	s.d.
k1a	0.14246	0.00052	0.132916	6.50E-05	0.189871	8.20E-05	0.155411	3.80E-05
k1d	26.33	0.13	22.331	0.013	22.918	0.012	25.6339	0.008
k2a	0.09161	5.80E-05	0.083558	1.10E-05	0.058456	5.50E-06	0.106406	7.80E-06
k3a	6200	1100	25100	4100	27100	4300	48700	7600
k4a	0.12403	0.00017	0.071544	2.90E-05	0.062288	2.50E-05	0.084697	2.10E-05
k4d	6.53	0.013	5.5474	0.0028	5.6242	0.0025	6.2249	0.0019
k5a	0.11234	3.30E-05	0.080101	5.40E-06	0.058801	4.00E-06	0.088025	3.30E-06
k6a	7300	1100	23900	3700	25000	4600	48800	7500
k7a	190	55000	510	720000	560	820000	720	700000
k7d	810	240000	1900	2.67E+06	1400	2.12E+06	2600	2.50E+06
k8a	0.0053	0.82	0.00012	100	0.0012	0.11	5.70E-05	28
k8d	800	120000	120	9.96E+07	1500	140000	100	5.00E+07
k9a	0.028	2	1.00E-06	1.3	0.014	0.56	1.00E-06	0.68
k10a	0.00039	1200	0.0012	0.17	2.50E-05	17	0.00094	0.061
k10d	97	3.01E+10	1700	230000	56	3.81E+07	2200	140000
k11a	1.00E-06	3.3	0.028	1.8	1.00E-06	0.99	0.031	0.91
k12a	1.00E-06	0.0053	0.00034	0.0025	0.00018	0.0016	0.0004	0.0031
k12d	21	210000	530	29000	580	61000	1400	100000
k13a	0.12	530	0.8	40	0.76	75	1.6	110
k14a	0.011	0.16	0.0027	0.071	0.00098	0.016	0.0018	0.057
k14d	540	9000	1700	63000	1200	50000	2400	110000
k15a	0.38	1.3	0.74	10	0.82	22	0.97	17
k16d	12	5.88E+07	14	1.32E+07	12	9.72E+06	13	7.10E+06
k17d	17	1.07E+08	14	1.82E+07	14	1.54E+07	18	1.50E+07
k18d	16	7.52E+07	11	9.90E+06	11	8.91E+06	12	7.60E+06
k19d	3.7	1.92E+07	0.069	8.97E+04	1.2	1.20E+06	3.9	2.50E+06
k20d	11	7.48E+07	12	1.68E+07	6.1	7.93E+06	9.7	9.10E+06
k21d	11	7.26E+07	12	2.04E+07	6.2	8.06E+06	9.7	9.10E+06
k22d	19	7.41E+07	15	1.65E+07	11	1.09E+07	14	7.80E+06
k23d	22	9.46E+07	12	9.96E+06	15	1.80E+07	19	1.70E+07
k24d	16	7.04E+07	11	1.06E+07	11	8.47E+06	12	8.00E+06

Rate law of the non-channeling model is attached as a non-channeling file.
“non” indicates HK2/G6PD mix, the name of charged sfGFP indicates the charged of sfGFP modified the HK2-G6PD cascade.
All data starts at 1.

Table S 4.3 k_{cat} and Michaelis constant from the k-value of the non-channeling model. Statistical significance is calculated by One-way ANOVA for each kinetic constant, and in comparing to group "non". "ns" indicates a p value > 0.05, * indicates p ≤ 0.05. Data are mean ± s.d.

Apparent kinetic constant	(+36)sfGFP		(0)sfGFP		(-30)sfGFP		non
$K_{M,NADP}$ = k11*k12/(k9*(k11+k12))	3.00±0.17	*	2.02±0.18	ns	1.35±0.16	*	2.04±0.14
$K_{M,G6P}$ = k11*k12/(k10*(k11+k12))	8.87±0.18	*	9.87±0.18	ns	12.01±0.15	*	9.52±0.13
k_{cat} = k11*k12/(k11+k12)	8.58±0.21	*	8.08±0.24	ns	6.95±0.23	*	7.62±0.19

Table S 4.4 Kinetic parameters of HK2 and HK2-sfGFP. Statistical significance is calculated by One-way ANOVA for each kinetic parameters, and in comparing to HK2 in the absence of sfGFP modification. "ns" indicates a p value >0.05, * is $p \leq 0.05$. Data are mean ± s.d.

	$k_{cat}(s^{-1})$		α		$K_{i,Glucose}(\mu M)$		$K_{i,ATP}(\mu M)$	
HK2-(+36)sfGFP	3.01±0.02	*	12.98±3.94	ns	16.66±4.87	ns	6.60±1.92	ns
HK2-(0)sfGFP	2.24±0.01	ns	15.14±4.84	ns	15.69±4.83	ns	7.72±2.37	ns
HK2-(-30)sfGFP	1.61±0.02	*	10.50±4.29	ns	20.96±8.02	ns	18.84±7.28	ns
HK2	2.12±0.02		12.03±5.13		17.53±7.16		9.47±3.87	

Table S 4.5 Kinetic parameters of G6PD and G6PD-sfGFP. Statistical significance is calculated by One-way ANOVA for each kinetic parameters, and in comparing to G6PD in the absence of sfGFP modification. "ns" indicates a p value >0.05, * is $p \leq 0.05$. Data are mean ± s.d.

	$k_{cat}(s^{-1})$	$K_{M,NADP}(\mu M)$	$K_{M,G6P}(\mu M)$	$K_{i,NADP+}(\mu M)$
G6PD-(+36)sfGFP	11.14±0.45 ns	3.246±0.20 *	121.47±10.37 *	1.98±0.28 *
G6PD-(0)sfGFP	10.91±0.67 ns	3.693±0.15 ns	163.50±10.64 ns	2.68±0.26 ns
G6PD-(-30)sfGFP	9.88±0.53 ns	4.280±0.23 *	191.93±14.37 *	3.26±0.33 *
G6PD	10.43±0.37	3.825±0.18	165.50±11.55	2.52±0.13

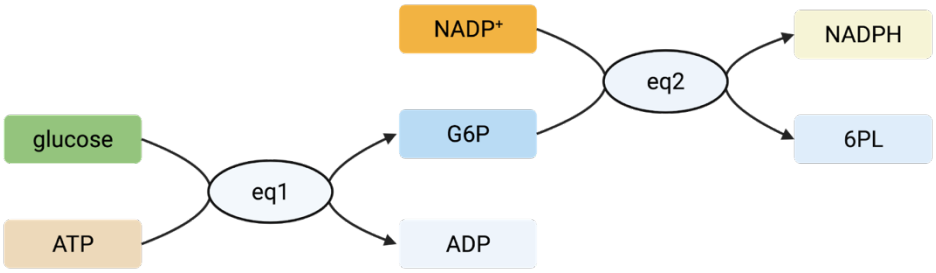

Figure S 4.10 The schematic diagram of the kinetic model. The eq1 indicates the random bi-bi reaction equation of HK2. The eq2 indicates the order bi-bi reaction equation of G6PD.

List S 4.1 The rate laws of the kinetic model.

$$eq1 = \frac{k_{\text{cat}} \times [glucose] \times [ATP]}{\alpha \times \left(K_{i,ATP} \times K_{i,glucose} + K_{i,ATP} \times [glucose] + K_{i,glucose} \times [ATP]\right) + [glucose] \times [ATP]}$$

$$eq2 = \frac{k_{cat} \times [NADP^+] \times [G6P]}{k_{i,NADP^+} \times K_{M,G6P} + K_{M,G6P} \times [NADP^+] + K_{M,NADP^+} \times [G6P] + [NADP^+] \times [G6P]}$$

$$d[glucose]/dt = -eq1$$

$$d[ATP]/dt = -eq1$$

$$d[ADP]/dt = eq1$$

$$d[G6P]/dt = eq1 - eq2$$

$$d[NADP^+]/dt = -eq2$$

$$d[NADPH]/dt = eq2$$

$$d[6PL]/dt = eq2$$

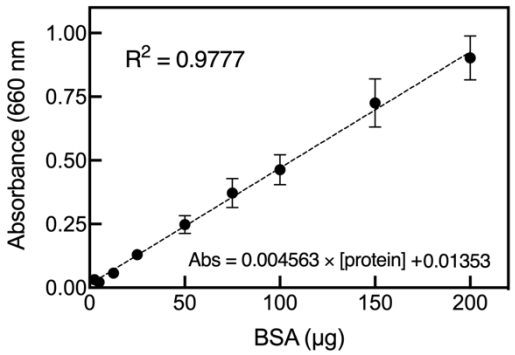

Figure S 4.11 Typical color response curves for BSA using protein assay procedure.

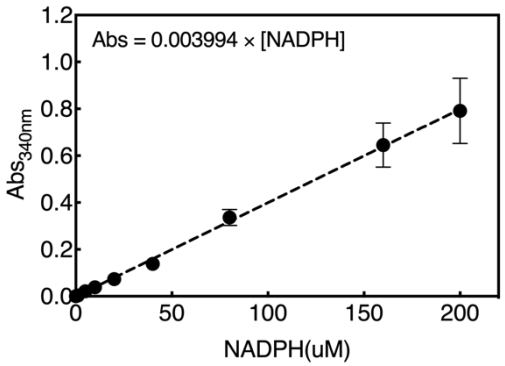

Figure S 4.12 NADPH concentration curve measured using absorbance at 340 nm. The NADPH was measured as the kinetic assay condition. The correlation between absorbance and NADPH concentration was converted with the equation listed in the figure.

Table S 4.6 Primers for site-directed mutagenesis (all sequences listed from 5'- to 3'-)

Sequence	Comment	Tm[1]
TGACTTCAAAtagAAAGGCAACATTTTAG CGACCTTTCAGTTTGATAC	E131U[2] in (+36)sfGFP	57°C
TGACTTCAAAtagGACGGCAACATTTTAG CGACCTTTCAGTTCGATAC	E131U in (0)sfGFP	61°C
CGACTTCAAAtagGACGGCAACATTTTAG ATACCTTTCAGTTCGATACG	E131U in (-30)sfGFP	60°C
CTACCACATGtagCTCTCTGATGAGAC AGATACTGGTCAACCTTC	R33U[3] in HK2	58°C

1: Tm is calculated by NEBaseChanger version 1.3.2.
2: The site E131U is based on PDB file 2b3p.
3: The site R33U is based on DNA sequence.

List S 4.2 Genes in this project before site-directed mutagenesis. Gene encoded target enzyme was labeled by underline. Site in the gene for direct mutation to amber code was labeled as **red bold**. Gene colored as orange encoded SpyTag. Gene colored as blue encoded SpyCatcher.

(+36)sfGFP-SpyTag

ATGGGCAGCAGCCATCATCATCATCATCACAGCAGCGGCCTGGTGCCGCGCGGCAGC 57
CATATGGCTAGCATGACTGGTGGACAGCAAATGGGTCGCGGATCCGAATTCGAGCTC 114
CGTCGACAAATGGGTGGCGCTAGCAAAGGTGAACGTCTGTTTCGTGGTAAAGTACCG 171
ATCTTAGTGGAATTAAAGGGCGACGTGAACGGTCATAAATTTAGCGTGCGCGGCAAA 228
GGCAAAGGTGACGCTACCCGTGGTAAATTGACCCTGAAGTTTATTTGCACAACAGGC 285
AAATTACCCGTTCCGTGGCCCACCTTAGTGACCACCCTGACCTATGGCGTTCAGTGC 342
TTCAGTCGTTACCCTAAACATATGAAACGTCACGATTTTTTCAAATCAGCCATGCCT 399
AAAGGATATGTTCAAGAGCGTACAATCAGCTTCAAGAAGGATGGCAAATATAAAACG 456
CGTGCGGAAGTGAAATTTGAAGGCCGCACATTAGTAAATCGTATCAAACTGAAAGGT 513
CGTGACTTCAAA**GAA**AAAGGCAACATTTTAGGCCATAAACTGCGTTATAACTTTAAT 570
TCTCATAAGGTGTATATTACGGCCGATAAACGCAAGAATGGTATCAAGGCAAAATTC 627
AAAATTCGCCATAACGTGAAAGACGGCAGCGTTCAATTAGCGGATCATTATCAACAA 684
AACACGCCGATTGGTCGCGGGCCTGTACTGTTACCTCGCAACCACTACCTGAGCACC 741
CGTTCTAAACTGAGCAAAGATCCGAAAGAAAAACGCGATCACATGGTTCTGTTAGAA 198
TTCGTGACCGCTGCAGGCATTAAGCACGGACGCGACGAACGCTACAAGGCCCACATC 855
CGTGATGGTGGACGCCTACAAGCCGACGAAGTAA 888

(0)sfGFP-SpyTag

ATGGGCAGCAGCCATCATCATCATCATCACAGCAGCGGCCTGGTGCCGCGCGGCAGC 57
CATATGGCTAGCATGACTGGTGGACAGCAAATGGGTCGCGGATCCGAATTCGAGCTC 114
CGTCGACAAATGGGTGGCGCTAGCAAAGGTGAACGTCTGTTTACTGGTGTAGTACCG 171
ATCTTAGTGGAATTAGACGGCGACGTGAACGGTCATAAATTTAGCGTGCGCGGCGAG 228
GGCGAAGGTGACGCTACCAATGGTAAATTGACCCTGAAGTTTATTTGCACAACAGGC 285
AAATTACCCGTTCCGTGGCCCACCTTAGTGACCACCCTGACCTATGGCGTTCAGTGC 342
TTCAGTCGTTACCCTGATCATATGAAACAACACGATTTTTTCAAATCAGCCATGCCT 399
GAAGGATATGTTCAAGAGCGTACAATCAGCTTCAAGGACGATGGCACCTATAAAACG 456
CGTGCGGAAGTGAAATTTGAAGGCGACACATTAGTAAATCGTATCGAACTGAAAGGT 513
CGTGACTTCAAA**GAA**GACGGCAACATTTTAGGCCATAAACTGGAATATAACTTTAAT 570
TCTCATAACGTGTATATTACGGCCGATAAACAGAAGAATGGTATCAAGGCAAATTTC 627
AAAATTCGCCATAACGTGGAGGACGGCAGCGTTCAATTAGCGGATCATTATCAACAA 684
AACACGCCGATTGGTGATGGGCCTGTACTGTTACCTCGCAACCACTACCTGAGCACC 741
CAATCTGCCCTGAGCAAAGATCCGAAAGAAAAACGCGATCACATGGTTCTGTTAGAA 198
TTCGTGACCGCTGCAGGCATTACGCACGGAATGGACGAACGCTACAAGGCCCACATC 855
CGTGATGGTGGACGCCTACAAGCCGACGAAGTAA 888

(-30)sfGFP

ATGGGCAGCAGCCATCATCATCATCATCACAGCAGCGGCCTGGTGCCGCGCGGCAGC 57
CATATGGCTAGCATGACTGGTGGACAGCAAATGGGTCGCGGATCCGAATTCGAGCTC 114
CGTCGACAAATGGGTGGCGCTAGCAAAGGTGAAGAGCTGTTTGACGGTGTAGTACCG 171
ATCTTAGTGGAATTAGACGGCGACGTGAACGGTCACGAATTTAGCGTGCGCGGCGAG 228
GGCGAAGGTGACGCTACCGAGGGTGAATTGACCCTGAAGTTTATTTGCACAACAGGC 285
GAATTACCCGTTCCGTGGCCCACCTTAGTGACCACCCTGACCTATGGCGTTCAGTGC 342
TTCAGTGATTACCCAGATCATATGGATCAACACGATTTTTTCAAATCAGCCATGCCT 399
GAAGGATATGTTCAAGAGCGTACAATCAGCTTCAAGGACGATGGCACCTATAAAACG 456

```
CGTGCGGAAGTGAAATTTGAAGGCGACACATTAGTAAACCGTATCGAACTGAAAGGT   513
ATCGACTTCAAAGAAGACGGCAACATTTTAGGCCATAAGCTGGAATATAACTTTAAT   570
TCTCATGACGTGTATATTACGGCCGATAAACAGGAAAACGGTATCAAGGCAGAATTT   627
GAAATTCGCCATAACGTGGAGGACGGCAGCGTTCAATTAGCGGATCATTATCAACAA   684
AACACGCCGATTGGTGATGGGCCTGTACTGTTACCTGACGATCACTACCTGAGCACG   741
GAGTCAGCCCTGAGCAAAGATCCGAACGAAGACCGCGATCACATGGTTCTGTTAGAA   198
TTCGTGACCGCTGCAGGCATTGATCATGGAATGGACGAGCTGTACAAGGCCCACATC   855
CGTGATGGTGGACGCCTACAAGCCGACGAAGTAA                          888

G6PD-SpyCatcher
ATGGGCAGCAGCCATCATCATCATCATCACAGCAGCGGCCTGGTGCCGCGCGGCAGC   57
CATGGCGCCATGGTTGATACCTTATCAGGTTTATCAAGTGAGCAAGGTCAGTCCGGT   114
GATATGACAATTGAAGAAGATAGTGCTACCCATATTAAATTCTCAAAACGTGATGAG   171
GACGGCAAAGAGTTAGCTGGTGCAACTATGGAGTTGCGTGATTCATCTGGTAAAACT   228
ATTAGTACATGGATTTCAGATGGACAAGTGAAAGATTTCTACCTGTATCCAGGAAAA   285
TATACATTTGTCGAAACCGCAGCACCAGACGGTTATGAGGTAGCAACTGCTATTACC   342
TTTACAGTTAATGAGCAAGGTCAGGTTACTGTAAATGGCAAAGCAACTAAAGGTGAC   399
GCTCATATTGGTATGGCTATGGCAGAGCAGGTGGCCCTGAGCCGGACCCAGGTGTGC   456
GGGATCCTGCGGGAAGAGCTTTTCCAGGGCGATGCCTTCCATCAGTCGGATACACAC   513
ATATTCATCATCATGGGTGCATCGGGTGACCTGGCCAAGAAGAAGATCTACCCCACC   570
ATCTGGTGGCTGTTCCGGGATGGCCTTCTGCCCGAAAACACCTTCATCGTGGGCTAT   627
GCCCGTTCCCGCCTCACAGTGGCTGACATCCGCAAACAGAGTGAGCCCTTCTTCAAG   684
GCCACCCCAGAGGAGAAGCTCAAGCTGGAGGACTTCTTTGCCCGCAACTCCTATGTG   741
GCTGGCCAGTACGATGATGCAGCCTCCTACCAGCGCCTCAACAGCCACATGAATGCC   798
CTCCACCTGGGGTCACAGGCCAACCGCCTCTTCTACCTGGCCTTGCCCCCGACCGTC   855
TACGAGGCCGTCACCAAGAACATTCACGAGTCCTGCATGAGCCAGATAGGCTGGAAC   912
CGCATCATCGTGGAGAAGCCCTTCGGGAGGGACCTGCAGAGCTCTGACCGGCTGTCC   969
AACCACATCTCCTCCCTGTTCCGTGAGGACCAGATCTACCGCATCGACCACTACCTG   1026
GGCAAGGAGATGGTGCAGAACCTCATGGTGCTGAGATTTGCCAACAGGATCTTCGGC   1083
CCCATCTGGAACCGGGACAACATCGCCTGCGTTATCCTCACCTTCAAGGAGCCCTTT   1140
GGCACTGAGGGTCGCGGGGGCTATTTCGATGAATTTGGGATCATCCGGGACGTGATG   1197
CAGAACCACCTACTGCAGATGCTGTGTCTGGTGGCCATGGAGAAGCCCGCCTCCACC   1254
AACTCAGATGACGTCCGTGATGAGAAGGTCAAGGTGTTGAAATGCATCTCAGAGGTG   1311
CAGGCCAACAATGTGGTCCTGGGCCAGTACGTGGGGAACCCCGATGGAGAGGGCGAG   1368
GCCACCAAAGGGTACCTGGACGACCCCACGGTGCCCCGCGGGTCCACCACCGCCACT   1425
TTTGCAGCCGTCGTCCTCTATGTGGAGAATGAGAGGTGGGATGGGGTGCCCTTCATC   1482
CTGCGCTGCGGCAAGGCCCTGAACGAGCGCAAGGCCGAGGTGAGGCTGCAGTTCCAT   1539
GATGTGGCCGGCGACATCTTCCACCAGCAGTGCAAGCGCAACGAGCTGGTGATCCGC   1596
GTGCAGCCCAACGAGGCCGTGTACACCAAGATGATGACCAAGAAGCCGGGCATGTTC   1653
TTCAACCCCGAGGAGTCGGAGCTGGACCTGACCTACGGCAACAGATACAAGAACGTG   1710
AAGCTCCCTGACGCCTATGAGCGCCTCATCCTGGACGTCTTCTGCGGGAGCCAGATG   1767
CACTTCGTGCGCAGCGACGAGCTCCGTGAGGCCTGGCGTATTTTCACCCCACTGCTG   1824
CACCAGATTGAGCTGGAGAAGCCCAAGCCCATCCCCTATATTTATGGCAGCCGAGGC   1881
CCCACGGAGGCAGACGAGCTGATGAAGAGAGTGGGTTTCCAGTATGAGGGCACCTAC   1938
AAGTGGGTGAACCCCCACAAGCTCTGA                                 1965
```

HK2

ATGGGCAGCAGCCATCATCATCATCATCACAGCAGCGGCCTGGTTCCGCGTGGTAGT 57
GACCAAGTGCAGAAGGTTGACCAGTATCTCTACCACATGCGCCTCTCTGATGAGACC 114
CTCTTGGAGATCTCTAAGCGGTTCCGCAAGGAGATGGAGAAAGGGCTTGGAGCCACC 171
ACTCACCCTACTGCAGCAGTGAAGATGCTGCCCACCTTTGTGAGGTCCACTCCAGAT 228
GGGACAGAACACGGAGAGTTCCTGGCTCTGGATCTTGGAGGGACCAACTTCCGTGTG 285
CTTTGGGTGAAAGTAACGGACAATGGGCTCCAGAAGGTGGAGATGGAGAATCAGATC 342
TATGCCATCCCTGAGGACATCATGCGAGGCAGTGGCACCCAGCTGTTTGACCACATT 399
GCCGAATGCCTGGCTAACTTCATGGATAAGCTACAAATCAAAGACAAGAAGCTCCCA 456
CTGGGTTTTACCTTCTCGTTCCCCTGCCACCAGACTAAACTAGACGAGAGTTTCCTG 513
GTCTCATGGACCAAGGGATTCAAGTCCAGTGGAGTGGAAGGCAGAGACGTTGTGGCT 570
CTGATCCGGAAGGCCATCCAGAGGAGAGGGGACTTTGATATCGACATTGTGGCTGTG 627
GTGAATGACACAGTTGGGACCATGATGACCTGTGGTTATGATGACCACAACTGTGAG 684
ATTGGTCTCATTGTGGGCACGGGCAGCAACGCCTGCTACATGGAAGAGATGCGCCAC 741
ATCGACATGGTGGAAGGCGATGAGGGGCGGATGTGTATCAATATGGAGTGGGGGGCC 798
TTCGGGGACGATGGCTCGCTCAACGACATTCGCACTGAGTTTGACCAGGAGATTGAC 855
ATGGGCTCACTGAACCCGGGAAAGCAACTGTTTGAGAAGATGATCAGTGGGATGTAC 912
ATGGGGGAGCTGGTGAGGCTTATCCTGGTGAAGATGGCCAAGGAGGAGCTGCTCTTT 969
GGGGGGAAGCTCAGCCCAGAGCTTCTCAACACCGGTCGCTTTGAGACCAAAGACATC 1026
TCAGACATTGAAGGGGAGAAGGATGGCATCCGGAAGGCCCGTGAGGTCCTGATGCGG 1083
TTGGGCCTGGACCCGACTCAGGAGGACTGCGTGGCCACTCACCGGATCTGCCAGATC 1140
GTGTCCACACGCTCCGCCAGCCTGTGCGCAGCCACCCTGGCCGCCGTGCTGCAGCGC 1197
ATCAAGGAGAACAAAGGCGAGGAGCGGCTGCGCTCTACTATTGGGGTCGACGGTTCC 1254
GTCTACAAGAAACACCCCCATTTTGCCAAGCGTCTACATAAGACCGTGCGGCGGCTG 1311
GTGCCCGGCTGCGATGTCCGCTTCCTCCGCTCCGAGGATGGCAGTGGCAAAGGTGCA 1368
GCCATGGTGACAGCAGTGGCTTACCGGCTGGCCGATCAACACCGTGCCCGCCAGAAG 1425
ACATTAGAGCATCTGCAGCTGAGCCATGACCAGCTGCTGGAGGTCAAGAGGAGGATG 1482
AAGGTAGAAATGGAGCGAGGTCTGAGCAAGGAGACTCATGCCAGTGCCCCCGTCAAG 1539
ATGCTGCCCACCTACGTGTGTGCTACCCCGGACGGCACAGAGAAAGGGGACTTCTTG 1596
GCCTTGGACCTTGGAGGAACAAATTTCCGGGTCCTGCTGGTCCGTGTTCGGAATGGG 1653
AAGTGGGGTGGAGTGGAGATGCACAACAAGATCTACGCCATCCCGCAGGAGGTCATG 1710
CACGGCACCGGGGACGAGCTCTTTGACCACATTGTCCAGTGCATCGCGGACTTCCTC 1767
GAGTACATGGGCATGAAGGGCGTGTCCCTGCCTCTGGGTTTTACCTTCTCCTTCCCC 1824
TGCCAGCAGAACAGCCTGGACGAGAGCATCCTCCTCAAGTGGACAAAAGGCTTCAAG 1881
GCATCTGGCTGCGAGGGCGAGGACGTGGTGACCCTGCTGAAGGAAGCGATCCACCGG 1938
CGAGAGGAGTTTGACCTGGATGTGGTTGCTGTGGTGAACGACACAGTCGGAACTATG 1995
ATGACCTGTGGCTTTGAAGACCCTCACTGTGAAGTTGGCCTCATTGTTGGCACGGGC 2052
AGCAATGCCTGCTACATGGAGGAGATGCGCAACGTGGAACTGGTGGAAGGAGAAGAG 2109
GGGCGGATGTGTGTGAACATGGAATGGGGGGCCTTCGGGGACAATGGATGCCTAGAT 2166
GACTTCCGCACAGAATTTGATGTGGCTGTGGATGAGCTTTCACTCAACCCCGGCAAG 2223
CAGAGGTTCGAGAAAATGATCAGTGGAATGTACCTGGGTGAGATTGTCCGTAACATT 2280
CTCATCGATTTCACCAAGCGTGGACTACTCTTCCGAGGCCGCATCTCAGAGCGGCTC 2337
AAGACAAGGGGCATCTTTGAAACCAAGTTCTTGTCTCAGATTGAGAGTGACTGCCTG 2394
GCCCTGCTGCAAGTCCGAGCCATCCTGCAACACTTAGGGCTTGAGAGCACCTGTGAC 2451
GACAGCATCATTGTTAAGGAGGTGTGCACTGTGGTGGCCCGGCGGGCAGCCCAGCTC 2508
TGTGGCGCAGGCATGGCCGCTGTGGTGGACAGGATACGAGAAAACCGTGGGCTGGAC 2565
GCTCTCAAAGTGACAGTGGGTGTGGATGGGACCCTCTACAAGCTACATCCTCACTTT 2622
GCCAAAGTCATGCATGAGACAGTGAAGGACCTGGCTCCGAAATGTGATGTGTCTTTC 2679
CTGCAGTCAGAGGATGGCAGCGGGAAGGGGGCGGCGCTCATCACTGCTGTGGCCTGC 2736
CGCATCCGTGAGGCTGGACAGTCATCACGATAA 2769

Chapter 5. Summary and conclusion

Enzymes work as efficient biocatalysts that determine the rate of biological reactions and control complex cellular metabolic pathways and other cellular processes. Their high catalytic efficiency is remarkable, so enzymes are now an important industrial tool for targeted chemical transformations. Specifically, modern enzymology, which is at the heart of food and beverage manufacturing processes, is also simultaneously related to a myriad of industrial applications, such as the production, processing, and quality performance improvement of animal feed and detergents pharmaceuticals and textile products. However, a big challenge is the susceptibility of natural enzymes to denaturation under environmental conditions. However, advances in biomolecular engineering have shifted the challenge to improving the reaction kinetics of enzymes above wild-type levels. The catalytic efficiency of many wild-type enzymes that are of industrial value are low, and inefficient catalysis is becoming more and more prominent, especially with the growing demand at the industrial level. Through rational design, directed evolution, computational design, and other cases, many existing active site engineering approaches have been shown to improve enzyme catalytic efficiency. At the same time, design rules for conjugation strategies that increase the reaction kinetics of enzymes above wild-type levels lack an explanation of how they can be exploited. Thus, a new approach is needed that builds on these previous successes and breaks down these apparent challenges to create an adequate reaction. The approach proposed here is synergistic with traditional active site engineering approaches and can be used to improve catalysis once the limits of active site engineering have been reached and no further gains through directed evolution are possible.

This endeavor has many ramifications. First, the study provides a new mechanism for improving enzyme catalytic efficiency without relying on the enzyme itself.

Chapter 2 presents a new enzyme engineering strategy to achieve this goal. The strategy uses a designed DNA scaffold to modify the enzyme microenvironment to improve kinetics and stability. This approach is an essential step towards achieving effective biocatalytic solutions to treat organophosphate poisoning, which is a long-standing problem in the field of catalysis. At the same time, the method promises to replace the common PEGylation (usually, PEGylation improves stability but not kinetics) with a new technique that enhances both stability and reaction kinetics. This new enzyme engineering strategy allows phosphodiesterase (PTE) to hydrolyze organophosphorus p-hydroxylates 11 times faster. This enhancement is a remarkable success considering the already fast PTE kinetics (with the turnover rate over 2000 s^{-1}). Specifically, it maintains the turnover rate while the second-order rate constant is as high as 10^7 $M^{-1}s^{-1}$. Simultaneously, a PTE-DNA system tuned for the hydrolysis of the chemical warfare toxin VX saw a three-fold boost in kinetics. According to mechanistic investigations, the scaffold enhances local substrate concentration by weak substrate binding. Improved thermal stability and enhanced resistance to protease attack were also achieved, with 48h in 37C serum, PTE maintained 4-fold activity after modification compared with non-modified one. This approach can theoretically improve any enzyme, especially when the substrate concentration is low (below the concentration represented by K_M). This approach, for example, has been studied for the degradation of fentanyl toxicity. The poisoning condition is analogous to organophosphorus poisoning in that the organophosphorus must be

destroyed before the fentanyl can be absorbed. We rationalized the DNA sequence to bind fentanyl effectively and demonstrated in our preliminary experiments that the degradation of fentanyl by Cytochrome P450 was enhanced by DNA modification. Another important implication of this method is that it improves the stability of the modified enzyme. The reason is that the method isolates the protein from the larger environment by randomly modifying the DNA and wrapping it to a certain extent. This isolation prevents harmful degradation of the protein and enhances its rigidity of the protein. Finally, this method is the basis for the opinion in Chapter 3. It provides a theoretical basis for our thinking about the enhancement of catalysis in multi-enzyme systems.

Despite the fact that we present an approach for rationally-designed DNA modifications based on conjugation to increase the enzyme's reaction kinetics, the existing method still has three areas that have not yet been addressed. One is the lack of design rules that explain how the conjugation method can improve the enzyme's reaction kinetics beyond wild-type levels. The second limitation is that the approach may only applicable when the target substrate is positively charged, as the negatively charged DNA scaffold must electrostatically attract the positively charged target molecule. Third, the approach is thus far limited to single enzyme systems, and we would like to broaden its application, such as cascade catalysis. A variety of bioconjugation techniques that form enzyme-scaffold complexes with regulated microenvironments can be used to boost enzyme activity. We show that computationally guided enzyme scaffold design can result in predicted increases in an enzyme's Michaelis constant, K_M, as well as an increase in the second-order rate constant, k_{cat}/K_M, in chapter 3. A rationally designed DNA covalently

attached to the enzyme PTE attracts the desired substrate (paraoxon) increasing the effective substrate concentration around the enzyme, an effect that results in a substantial decrease in K_M, an increase in substrate on-rate, k_1, and maintains the high catalytic turnover of the unmodified enzyme. The rise in substrate concentration near the DNA scaffold is due to both electrostatic attraction and short-range vdW forces, as shown by MD and BD simulations, allowing the concentration gradient around the scaffold to be quantified. We generated a series of PTE-DNA complexes with different distances between the conjugated DNA scaffold and the enzyme's active site (0.6 to 7.3 nm) via site-click, and were able to experimentally test the effect of scaffold position on enzyme kinetics as a result. We develop a capture radius model based on experimental and computational results that predicts K_M enhancements based on the position of the conjugated scaffold; conjugation close to the active site without sterically blocking access resulted in the greatest enhancement in enzyme kinetics, a 7.1-fold decrease in K_M. The model, as well as the experimental and computational results, represent a novel design strategy for increasing enzyme catalysis in controlled microenvironments using conjugated scaffolds to boost an enzyme's effective substrate concentration. We anticipate that this approach can be applied to create additional enzyme-scaffold bioconjugates with increased activity and kinetics, despite the fact that this work and the resulting design principles were developed utilizing PTE modified with a DNA scaffold.

Changing an enzyme's microenvironment to influence catalysis is not restricted to single enzyme systems; cascades of enzyme reactions are also capable of doing so. Substrate channels can isolate some or all substrates from the rest of the environment,

resulting in improved functional metabolism. Nonetheless, one of the most contentious issues in this sector is that the scaffolds utilized to build these complexes might cause significant changes in the enzyme's kinetics. These methods introduce new chemical and physical properties that could change the enzymatic activity of the environment around the organizing enzyme. We created a microenvironment distinct from the rest of the system in Chapter 4 by inserting sfGFP fusions with varying high charge densities (+36, 0, -30) into the cascade enzyme complexes of interest (HK2 and G6PD). Microenvironmental engineering can impact the catalysis of the cascade in the same manner that it can increase the turnover, stability, and kinetics of individual enzymes. In contrast to changes generated by substrate channels, specific enhancements are difficult to achieve due to changes in the microenvironment. When we acknowledge that the microenvironment is essential, we can design controlled experiments to aid in finding substrate channeling and, when appropriate, present alternate hypotheses.

A deeper understanding of the interactions between the microenvironment, multi-enzyme structural dynamics, and substrate channels will also help develop a range of new technologies. Synthetic cells, membrane-free organelles, and other systems that attempt to recapitulate cellular function will benefit from cascade design rules that address spatial organization and microenvironmental chemistry. Likewise, nanosized, co-permeable, or other chemical scaffolds for enzymes in physical structures will benefit. Substrate channels have certainly captured our attention and curiosity. This intriguing topic has also captured the attention and imagination of many, and it promises to inspire future researchers as these new applications mature. We hope that a fundamental understanding of the

microenvironment and the utilization of scaffolds for specific activity enhancement will be equally interesting.

It is worth mentioning that the method has a wide range of applications. Deconstruction of recalcitrant polymers (plastics), which was documented last year, is a good example. *Ideonella sakaiensis* has been found to secrete a two-enzyme system that breaks down polyethylene terephthalate (PET) into its monomers. PET is depolymerized by PETase in *I. sakaiensis*, releasing soluble compounds such as mono(2-hydroxyethyl) terephthalate (MHET), which is cleaved by MHETase into terephthalic acid and ethylene glycol. Plastics that would usually take hundreds of millions of years to decompose are degraded in a couple of months thanks to the dual enzyme system's synergistic action. This is unquestionably a significant step forward. While the approach improved the efficiency of dissolving plastics, the natural enzyme was thermally unstable, and the efficiency may be improved even further. The method described in Chapter 2 can be used to solve the problem of thermal instability. Meanwhile, the cascade catalytic efficiency could be increased by altering the microenvironment around the two enzymes. It is worth noting that the method described in Chapter 4 is not incompatible with the method described in Chapter 2. We can envision a cascade catalytic complex, with +36sfGFP as a bridge linkage and reasonably encapsulated in a protected and well-designed DNA scaffold, being widely used as a viable strategy for plastic degradation in the future, because the intermediates produced by plastic degradation are negatively charged.